Joint super-resolution/segmentation approaches for the tomographic images analysis of the bone micro-architecture

Alina Toma

Numéro d'ordre : 2016LYSEI019 Année 2016

THÈSE

présentée devant

L'Institut National des Sciences Appliquées de Lyon

pour obtenir

LE GRADE DE DOCTEUR

ÉCOLE DOCTORALE : ÉLECTRONIQUE, ÉLECTROTECHNIQUE, AUTOMATIQUE

par

Alina TOMA

Joint super-resolution/segmentation approaches for the tomographic images analysis of the bone micro-architecture

Soutenue publiquement le 9 mars 2016

Jury

Denis Kouamé	Professeur, Université Paul Sabatier Toulouse 3	Rapporteur
Maria J. Ledesma-Carbayo	Professeur (TU), Université Politecnica de Madrid	Rapporteur
Su Ruan	Professeur, Université de Rouen	Président
Jean-Baptiste Pialat	Professeur, Université de Lyon	Invité
Françoise Peyrin	Directeur de recherche INSERM	Directeur de thèse
Bruno Sixou	Maître de conférences, INSA de Lyon	Co-directeur de thèse
Loïc Denis	Maître de conférences, Université de Saint-Etienne	Co-encadrant de thèse

INSA Direction de la Recherche - Ecoles Doctorales – Quinquennal 2011-2015

SIGLE	ECOLE DOCTORALE	NOM ET COORDONNEES DU RESPONSABLE
CHIMIE	**CHIMIE DE LYON** **http://www.edchimie-lyon.fr** Sec : Renée EL MELHEM Bat Blaise Pascal 3e etage 04 72 43 80 46 Insa : R. GOURDON secretariat@edchimie-lyon.fr	M. Jean Marc LANCELIN Université de Lyon – Collège Doctoral Bât ESCPE 43 bd du 11 novembre 1918 69622 VILLEURBANNE Cedex Tél : 04.72.43 13 95 directeur@edchimie-lyon.fr
E.E.A.	**ELECTRONIQUE, ELECTROTECHNIQUE, AUTOMATIQUE** **http://edeea.ec-lyon.fr** Sec : M.C. HAVGOUDOUKIAN Ecole-doctorale.eea@ec-lyon.fr	M. Gérard SCORLETTI Ecole Centrale de Lyon 36 avenue Guy de Collongue 69134 ECULLY Tél : 04.72.18 60.97 Fax : 04 78 43 37 17 Gerard.scorletti@ec-lyon.fr
E2M2	**EVOLUTION, ECOSYSTEME, MICROBIOLOGIE, MODELISATION** **http://e2m2.universite-lyon.fr** Sec : Bat Atrium- UCB Lyon 1 04.72.44.83.62 Insa : S. REVERCHON secretariat.e2m2@univ-lyon.fr	M. Fabrice CORDEY Laboratoire de Géologie de Lyon Université Claude Bernard Lyon 1 Bât Géode – Bureau 225 43 bd du 11 novembre 1918 69622 VILLEURBANNE Cédex Tél : 04.72.44.83.74 Sylvie.reverchon-pescheux@insa-lyon.fr fabrice.cordey@ univ-lyon1.fr
EDISS	**INTERDISCIPLINAIRE SCIENCES-SANTE** **http://www.ediss-lyon.fr** Sec : Bat Atrium – UCB Lyon 1 04 72 44 83 62 Insa : secretariat.ediss@univ-lyon1.fr	Mme Emmanuelle CANET-SOULAS INSERM U1060, CarMeN lab, Univ. Lyon 1 Bâtiment IMBL 11 avenue Jean Capelle INSA de Lyon 696621 Villeurbanne Tél : 04.72.11.90.13 Emmanuelle.canet@univ-lyon1.fr
INFOMATHS	**INFORMATIQUE ET MATHEMATIQUES** **http://infomaths.univ-lyon1.fr** Sec :Renée EL MELHEM Bat Blaise Pascal 3e etage infomaths@univ-lyon1.fr	Mme Sylvie CALABRETTO LIRIS – INSA de Lyon Bat Blaise Pascal 7 avenue Jean Capelle 69622 VILLEURBANNE Cedex Tél : 04.72. 43. 80. 46 Fax 04 72 43 16 87 Sylvie.calabretto@insa-lyon.fr
Matériaux	**MATERIAUX DE LYON** **http://ed34.universite-lyon.fr** Sec : M. LABOUNE-DAHMANI PM : 71.70 –Fax : 87.12 Bat. Direction 1er et. Ed.materiaux@insa-lyon.fr	M. Jean-Yves BUFFIERE INSA de Lyon MATEIS Bâtiment Saint Exupéry 7 avenue Jean Capelle 69621 VILLEURBANNE Cedex Tél : 04.72.43 71.70 Fax 04 72 43 85 28 Ed.materiaux@insa-lyon.fr
MEGA	**MECANIQUE, ENERGETIQUE, GENIE CIVIL, ACOUSTIQUE** **http://mega.universite-lyon.fr** Sec : M. LABOUNE PM : 71.70 –Fax : 87.12 Bat. Direction 1er et. mega@insa-lyon.fr	M. Philippe BOISSE INSA de Lyon Laboratoire LAMCOS Bâtiment Jacquard 25 bis avenue Jean Capelle 69621 VILLEURBANNE Cedex Tél : 04.72 .43.71.70 Fax : 04 72 43 72 37 Philippe.boisse@insa-lyon.fr
ScSo	**ScSo*** **http://recherche.univ-lyon2.fr/scso/** Sec : Viviane POLSINELLI Brigitte DUBOIS Insa : J.Y. TOUSSAINT viviane.polsinelli@univ-lyon2.fr	Mme Isabelle VON BUELTZINGLOEWEN Université Lyon 2 86 rue Pasteur 69365 LYON Cedex 07 Tél : 04.78.77.23.86 Fax : 04.37.28.04.48 isavonb@dbmail.com

*ScSo : Histoire, Géographie, Aménagement, Urbanisme, Archéologie, Science politique, Sociologie, Anthropologie

Contents

Abstract

Osteoporosis is a bone fragility disease increasing with the aging of the population in many countries. The early diagnosis of osteoporosis is a major goal to prevent severe complications. For this aim, the investigation of trabecular bone micro-architecture provides relevant information to determine the bone strength. While the spatial resolution of clinical CT scanners is not sufficient to resolve the trabecular structure, new High Resolution peripheral Quantitative CT (HR-pQCT) systems have been developed to investigate bone micro-architecture *in-vivo* at peripheral sites (tibia and radius). Despite this considerable progress, the quantification of 3D trabecular bone micro-architecture *in-vivo* remains limited due to a lack of spatial resolution compared to the trabeculae size.

The objective of this thesis is to propose a joint super-resolution/segmentation approach for improving the quantitative analysis of *in-vivo* HR-pQCT images of the trabecular bone structure.

To begin with, we have investigated super-resolution methods for improving the image resolution. Super-resolution is a linear ill-posed inverse problem and one way to solve it is by using regularization methods. Approaches based on Total Variation (TV) and Higher Degree Total Variation (HDTV) were compared on 2D images of the trabecular bone. The minimization was made with a customized implementation of the state-of-the-art ADMM (Alternating Direction Method of Multipliers) method.

Afterwards, we have addressed the problem of the TV regularization parameter selection in the ADMM algorithm. An iterative method combining the Morozov principle and the Newton method was proposed in order to estimate the regularization parameter. This method was first compared with the Unbiased Predictive Risk Estimator (UPRE) method in the case of deconvolution. Then the Morozov principle was modified to be adapted to super-resolution and to obtain improved results compared to UPRE. The method provides a very good regularization parameter only in few iterations compared with the UPRE method that requires an extensive scanning of parameter values.

Furthermore, since our main goal is the quantification of the binary trabecular bone micro-structure images, we have developed a joint super-resolution/segmentation method. For this purpose, we proposed using a prior based on Total Variation with a convex relaxation (TVbox).The validation of the proposed methods was made on experimental micro-CT bone images after simulating the effect of blur, a loss of spatial resolution and degradation by noise. The results showed an improvement of the bone parameters and 3D connectivity with the TVbox method.

At the end of this research, we have investigated a semi-blind joint super-resolution/ segmentation approach aiming to estimate both the binary super-resolved image and the blurring kernel that is not known for the real HR-pQCT images. For this aim, we have used an alternated minimization scheme assuming that the images were blurred with a Gaussian blur. The first tests performed on a HR-pQCT experimental image for which a ground truth was available, showed better quantitative and visual results.

In conclusion, our work has shown that TV based optimization methods promise to improve the quantification of bone micro-architecture from HR-pQCT images.

Résumé

L'analyse de la microstructure osseuse joue un rôle important pour étudier des maladies de l'os comme l'ostéoporose. Des nouveaux scanners périphériques haute résolution (HR-pQCT) permettent de faire des acquisitions de la micro-architecture osseuse *in-vivo* sur l'homme. Toutefois la résolution spatiale de ces appareils reste comparable à la taille des travées osseuses, ce qui limite leur analyse quantitative.

L'objectif de cette thèse est de proposer de nouvelles approches jointes super-résolution/ segmentation pour une analyse quantitative plus fine des images HR-pQCT *in-vivo* de la structure osseuse trabéculaire.

Dans une première étape nous nous sommes concentrés sur des méthodes de super-résolution afin d'améliorer la résolution des images. La super-résolution est un problème linéaire inverse mal-posé. Plusieurs stratégies de régularisation par variation totale (TV) et TV d'ordre plus élevé (Higher Degree TV) ont été comparées dans des images 2D d'os trabéculaire. Une méthode de minimisation de la fonctionnelle de régularisation par un algorithme de type ADMM (Alternating Direction Method of Multipliers) a été implémentée.

Ensuite, nous nous sommes intéressés aussi au choix des paramètres de régularisation pour la régularisation TV dans l'algorithme ADMM. Une méthode itérative combinant le principe de Morozov et la méthode de Newton a été développée pour estimer le paramètre de régularisation. Cette méthode a été comparée à la méthode UPRE (Unbiased Predictive Risk Estimator). Un principe de Morozov modifié permet d'améliorer les résultats obtenus avec UPRE. La méthode mise au point est rapide et ne requiert pas un balayage exhaustif des valeurs des paramètres.

Le but final étant la quantification de la micro-structure trabéculaire de l'os et nécessitant de binariser la structure osseuse, nous avons développé dans une deuxième étape une méthode de super-résolution/segmentation conjointe. Dans ce but, nous avons proposé un a priori basé sur la Variation Totale avec une relaxation convexe (TVbox). La validation des méthodes proposées a été faite sur des images expérimentales micro-CT après simulation de l'effet du flou, la perte de résolution spatiale et la dégradation par le bruit. Les résultats montrent une amélioration de paramètres quantitatifs de l'os et de la connectivité 3D avec la méthode TVbox.

Finalement, en vue de l'application à des images réelles HR-pQCT, nous nous sommes intéressés à une approche conjointe semi-aveugle super-résolution/segmentation qui vise à estimer à la fois l'image binaire super-résolue et le noyau de convolution. Dans ce but, un schéma de minimisation alterné a été utilisé en supposant que l'image est convoluée avec un noyau Gaussien. Cet approche a été validé sur des images de test et aussi sur une image expérimentale de HR-pQCT, pour laquelle la vérité terrain est disponible.

En conclusion, notre travail montre que les méthodes d'optimisation basées sur la régularisation TV sont prometteurs pour améliorer la quantification de la micro-architecture osseuse sur des images HR-pQCT.

List of abbreviations

APS	Advanced Photon Source
ADMM	Alternating Direction Method of Multipliers
BMD	Bone Mineral Density
BV/TV	Bone Volume to Total Volume
CG	Conjugate Gradient
CT	Computed Tomography
DFT	Discrete Fourier Transform
DXA	Dual X-ray Absorptiometry
ESRF	European Synchrotron Radiation Facility
FBP	Filtered Back Projection
FEA	Finite Element Analysis
HA	Hydroxyapatite
HDTV	Higher Degree Total Variation
HR	High Resolution
HR-pQCT	High Resolution - peripheral Quantitative Computed Tomography
IHDTV	Isotropic Higher Degree Total Variation
IRLS	Iterated Reweighted Least Square
ISCD	International Society for Clinical Densitometry
KKT	Karush Kuhn Tucker
LR	Low Resolution
LTA	Local Topological Analysis
MIMO	Multi-Input Multi-Output
MISO	Multi-Input Single-Output
MM	Majorization-Minimization
MSE	Mean Squared Error
NV/BV	Node Volume to Bone Volume
pQCT	peripheral Quantitative Computed Tomography
PSF	Point Spread Function
PSNR	Peak Signal-to-Noise Ratio
PV/BV	Plates Volume to Bone Volume
QCT	Quantitative Computed Tomography
RV/BV	Rods Volume to Bone Volume
SISO	Single-Input Single-Output
SLS	Swiss Light Source
SMI	Structural Model Index
SNR	Signal-to-Noise Ratio
SOLEIL	Source Optimisée de Lumière d'Énergie Intermédiaire du LURE
TB.N	Trabecular Number
TB.Sp	Trabecular Separation
TB.Th	Trabecular Thickness

TV	Total Variation
UPRE	Unbiased Predictive Risk Estimator
VOI	Volume of Interest
WHO	World Health Organization

RESUME ETENDU

Introduction

L'ostéoporose est une maladie qui affecte les propriétés mécaniques des os et qui est caractérisée par une diminution de la densité minérale osseuse et par une altération de la micro-architecture trabéculaire osseuse. Cette maladie est responsable des fractures et des phénomènes de compression vertébrale qui peuvent conduire à une invalidité et à un décès. L'ostéoporose a attiré l'attention de nombreux cliniciens et chercheurs ces dernières décennies. Les statistiques montrent que 40% des femmes et 13% des hommes après 50 ans sont atteints d'ostéoporose et 24% des patients âgés meurent chaque année après une fracture de la hanche. De nos jours, le diagnostic de l'ostéoporose est basé sur une mesure de la densité minérale osseuse (BMD) par la technique de mesure d'absorption duale de rayon X (Dual X-ray absorptiometry). Cependant, cette technique ne peux estimer que 60 à 70% du risque de fracture. Par conséquent, de nouvelles techniques d'évaluation de la fragilité osseuse sont développées qui s'appuient sur une quantification de la micro-architecture osseuse.

La micro-tomographie par de rayons X fournit des images 3D avec une résolution spatiale plus élevée que les systèmes cliniques. Cette technique a été particulièrement utilisée pour l'analyse de la micro-architecture osseuse sur des échantillons osseux prélevés ou sur le petit animal [Seeman and Delmas (2006), Peter and Peyrin (2011)]. La micro-architecture de l'os qui est un déterminant important de la résistance biomécanique est formée d'un arrangement complexe de petites structures appelées travées qui ont une épaisseur de l'ordre de 150 μm. Les images 3D de la micro-architecture obtenues par micro-tomographie X sont ensuite traitées pour extraire les descripteurs quantitatifs 3D de la micro-structure de l'os. L'analyse de la structure de l'os requiert une méthode de segmentation de l'image comme première étape pour extraire la structure osseuse du fond. Ensuite le calcul des paramètres morphométriques comme le rapport du volume osseux au volume total, l'épaisseur moyenne des travées mais aussi des paramètres topologiques comme la connectivité ou l'organisation de la micro-structure en tubes ou en plaques, peut être effectué [Hildebrand *et al.* (1999), Peyrin *et al.* (2010)]. De tel descripteurs ont été utilisés dans de nombreuses études mais limitées à l'analyse d'échantillons osseux *ex-vivo*. Alors que la résolution spatiale des scanners cliniques n'est pas suffisante pour résoudre la structure trabéculaire, de nouveaux systèmes High Resolution peripheral Quantitative CT (HR-pQCT) ont été commercialisés pour étudier la micro-architecture osseuse *in-vivo* du tibia et du radius [Boutroy *et al.* (2005)]. Les images 3D sont ensuite segmentées et les mêmes paramètres que ceux utilisées pour la micro-tomographie sont utilisés pour quantifier la micro-architecture des patients. Cependant, le résultat de la segmentation peut être décevant, compromettant la quantification ultérieure [Tjong *et al.* (2012)]. Ce problème est relié à la résolution spatiale limitée de la technique HR-pQCT qui est proche de l'épaisseur des travées.

Le but de cette thèse est d'améliorer la quantification de la micro-structure osseuse à partir d'images HR-pQCT *in-vivo*. La validation des approches proposées est effectuée sur des images expérimentales haute résolution de micro-CT d'échantillons d'os avec une résolution de 20 μm après simulation de l'effet de la perte de résolution spatiale et de la dégradation par le bruit. Une validation plus réaliste est accomplie sur des images *ex-vivo* HR-pQCT pour lesquelles l'image vraie correspondante est aussi disponible.

Le plan de la thèse est le suivant :
Chapitre 1: Contexte médical
Chapitre 2: Cadre théorique
Chapitre 3: Super-résolution basée sur la Variation Totale
Chapitre 4: Sélection du paramètre de régularisation
Chapitre 5: Super-résolution/segmentation jointe
Chapitre 6: Approche semi-aveugle Super-résolution/segmentation jointe
Conclusion et perspectives

Dans le premier chapitre, nous détaillons le contexte médical de la thèse, c'est à dire les maladies de la fragilité osseuse. Nous présentons en particulier les méthodes d'imagerie permettant d'étudier le tissu osseux. Dans ce cadre, la micro-CT est devenue une technique de base pour analyser la micro-architecture osseuse en 3D, sur des échantillons osseux ou des modèles animaux. Nous présentons rapidement la micro-CT synchrotron qui sera utilisée pour avoir des images de référence dans ce travail, puis la tomographie quantitative haute résolution (HR-pQCT) qui permet l'analyse du tissu osseux *in-vivo* sur des sites périphériques. Les principaux paramètres utilisés pour quantifier la micro-architecture osseuse sont ensuite décrits.

Dans le second chapitre, nous détaillons les aspects théoriques liés aux problèmes inverses et aux méthodes de régularisation, en particulier pour les applications comme la super-résolution et la segmentation. Le problème de super-résolution peut être vu comme un problème inverse linéaire mal posé comme d'autres problèmes d'analyse d'image, le débruitage et la déconvolution. Ce type de problème a été très étudié et nous résumons dans ce chapitre les notions fondamentales du domaine. Les méthodes de régularisation peuvent être utilisées pour obtenir des solutions stables. Nous présentons notamment l'approche variationnelle dans laquelle une fonctionnelle de régularisation est construite pour résoudre ce problème. Différents termes de régularisation sont présentés comme le terme de Variation Totale (TV) qui a été l'objet d'une grande attention ces dernières années. L'équilibre entre le terme d'attache aux données et la pénalisation de régularisation est contrôlé par un paramètre de régularisation qui est crucial et qui est difficile à choisir. Ce choix peut être basé sur le niveau de bruit ou non. Les méthodes de base du choix du paramètre sont décrites. Plusieurs méthodes peuvent être utilisées pour minimiser la fonctionnelle de régularisation. Nous insistons sur la méthode ADMM (Alternate Direction of Minimization method) qui fait partie des méthodes les plus actuelles. Nous terminons ce chapitre par des généralités sur la segmentation et sur les métriques qui permettent d'évaluer la qualité de l'image reconstruite.

Dans le chapitre 3, nous étudions des méthodes de super-résolution 2D basées sur la variation totale. Ce type de régularisation est très utilisé pour restaurer des images constantes par morceaux mais il crée des effets de marche d'escalier et nous utilisons aussi des termes de régularisation d'ordre plus élevé similaires au terme TV. Ces termes sont considérés car ils constituent les approches les plus utiles pour des approches mixtes super-résolution/segmentation avec des valeurs quasi-binaires. Nous étendons aussi la méthode de minimisation ADMM à la régularisation HDTV (Higher Degree TV) . Nous introduisons une formulation générale du terme de régularisation adapté aux deux méthodes TV et HDTV isotrope basée sur des opérateurs linéaires différentiels. Ces termes d'ordres plus élevés sont considérés car on s'attend à ce qu'il diminue les effets d'escalier qui détériorent la reconstruction.

Dans le chapitre 4, nous présentons une nouvelle méthode de choix du paramètre de régularisation pour la régularisation TV. Cette méthode est basées sur une estimation du

niveau de bruit et elle généralise le principe classique de Morozov utilisé pour la régularisation de Tikhonov. Un principe modifié est présenté avec un algorithme très rapide de choix du paramètre basé sur ce principe. Cette méthode est évaluée sur différentes images tests ainsi que sur des images de la micro-architecture osseuse et comparée à une méthode d'estimation du paramètre de régularisation de la littérature, la méthode UPRE (Unbiased Predictive Risk Estimator).

Le chapitre 5 est consacré au problème 3D de super-résolution/segmentation jointe. Les problèmes de super-résolution et de segmentation sont souvent étudiés avec des approches variationnelles. Cependant, dans la plupart des cas ils sont considérés séparément. Dans ce chapitre, nous essayons de résoudre les deux problèmes en même temps avec une méthode variationnelle. La base de cette méthode est une convexification de la fonctionnelle de régularisation avec une terme de contrainte convexe additionnelle. La méthode de minimisation doit être modifiée pour inclure cette nouvelle contrainte. Des résultats sont présentés sur des volumes 3D de micro-architecture osseuse.

Le dernier chapitre présente une méthode semi-aveugle de super-résolution/segmentation. Un algorithme de minimisation alternée est utilisé pour restaurer les images haute résolution et les noyau de flou qui est supposé Gaussien. Cette approche est testée aussi sur des images réelles.

Nous terminons ce manuscrit avec des conclusions et des perspectives.

Chapitre 1 : Contexte médical

Tissu osseux

Les os forment le squelette qui est une partie du système locomoteur. Le squelette est responsable de la stabilité, du mouvement et de la forme du corps. De plus, les os stockent les minéraux comme le calcium et le phosphore. Les deux types de tissus osseux sont l'os cortical et l'os trabéculaire. L'os cortical est une coquille extérieure qui constitue 80% du squelette humain total et est localisé principalement à la périphérie du squelette. L'os cortical humain, organisé en ostéons, inclut un réseau complexe de canaux: les canaux Havers qui sont orientés longitudinalement et les canaux Volkmann qui sont orientés perpendiculairement.

L'os trabéculaire forme 70% du squelette humain central. Il est organisé de réseau en nid d'abeille constitué de travées verticales et horizontales. Au cours de la vie, l'ancien os est remplacé, renouvelé au cours d'un processus appelé remodelage, qui permet aux os de s'adapter aux contraintes mécaniques. Le remodelage osseux affecte 25% de l'os trabéculaire et seulement 2-3% de l'os cortical. Après reconstruction osseuse la concentration minérale dans certaines régions localisées augmente progressivement. L'os peut donc être vu comme un arrangement d'unité osseuses (BMU) avec différents degrés de minéralisation [Meunier and Boivin (1997)].

Ostéoporose

L'ostéoporose est une maladie qui affecte essentiellement les personnes âgées. Elle est caractérisée par une décroissance de la densité osseuse (BMD) et une altération de la micro-architecture osseuse du tissu osseux trabéculaire. La conséquence directe de cette maladie est la fragilité osseuse et une augmentation du risque de fracture. Les fractures de la hanche ou le problème de compression vertébrale sur des patients âgés atteints d'ostéoporose peuvent conduire à une invalidité ou à la mort. L'organisation mondiale de la santé définit l'ostéoporose à partir d'une densité minérale osseuse qui est plus faible de 2.5 écart-type par rapport à la moyenne d'elle (d'adultes jeunes, en bonne santé) mesurée par absorption bi-photonique à rayons X (DXA). Cependant cette technique ne peut estimer que 60% à 70% des risques de fracture [Peter and Peyrin (2011)]. Par conséquent, il devient de nécessaire de développer nouvelles methodes d'évaluation de la fragilité osseuse en particulier, en prenant en compte la micro-architecture osseuse.

Etude de la micro-architecture de l'os

L'analyse de la micro-structure trabécularie de l'os a un rôle important dans l'étude et dans le diagnostic des pertes de densité osseuse.
L'histomorphométrie représente la technique conventionnelle d'évaluation de l'architecture de l'os mais d'autres techniques non destructives sont de plus en plus utilisées dans ce but. Si l'on considère les techniques d'imagerie par rayons X, une autre méthode d'évaluation de l'architecture de l'os est la micro-tomographie par rayons X, une technique non destructive d'imagerie 3D qui peut également fournir la densité volumique alternativement à la technique standard DXA [Engelke *et al.* (1989)]. Des images de micro-CT améliorées, au sens du rapport signal sur bruit (SNR) avec une résolution très élevée ($<1\ \mu m$) peuvent être obtenues en utilisant le rayonnement synchrotron à la place des sources de rayons X standards. La microtomographie par rayonnement synchrotron est souvent utilisée comme

une technique de référence pour évaluer les modalités d'imagerie nouvelles. Toutefois, les systèmes de micro-CT pouvant atteindre des résolutions spatiales très élevées, sont réservés à des échantillons osseux ou au petit animal, mais ne sont pas adaptés pour imager l'os trabéculaire *in-vivo* chez l'homme. En revanche, de nouveaux systèmes de CT quantitative haute résolution (HR-pQCT), comme le système Scanco XtremeCT, peuvent fournir des images 3D de la micro-architecture osseuse de l'os pour les extrémités humaines (tibia et radius) à haute résolution (82 μm). Néanmoins, la taille de voxel restant très proche de la taille des travées osseuses, des études récentes ont montré que l'analyse des images HR-pQCT de l'os trabéculaire est biaisée par le manque de résolution des images [Tjong *et al.* (2012)].

Notre recherche a pour objectif d'améliorer la quantification de la micro-architecture de l'os à partir d'images HR-pQCT par des approches de super-résolution. Le problème sera formulé comme un problème inverse et résolu en incluant des différents termes de régularisation en 2D et en 3D. Un algorithme itératif de type ADMM sera implémenté. Les approches proposées seront validées d'abord sur des images micro-CT de super-résolution détériorées de façon artificielle et sous-échantillonnées avec la même résolution que les images réelles HR-pQCT. Des tests seront aussi effectués sur des images *ex-vivo* HR-pQCT pour lesquelles les images vraies de micro-tomographie sont disponibles.

Chapitre 2 : Cadre théorique

Problèmes inverses mal-posés

Les problèmes inverses linéaires rencontrés dans de nombreuses applications en science de l'ingénieur jouent un rôle très important en analyse d'image. Par exemple, les problèmes de déconvolution et de restauration sont cruciaux en imagerie médicale. Dans cette thèse, nous essayons d'inverser les problèmes mal posés de déconvolution et de super-résolution avec des approches de type variationnelle. Le cadre bayésien représente une autre voie pour formaliser et résoudre le même type de problèmes inverses mal-posés [Molina (1994), Ruiz *et al.* (2015)]. Le problème de super-résolution consiste à obtenir une ou un ensemble d'images hautes-résolution (HR) à partir d'une ou de plusieurs images de basse résolution [Farsiu *et al.* (2004)]. Ces dernières années, de nombreuses approches de super-résolution ont été proposées.

Approches variationnelles de régularisation

Une méthode bien connue pour résoudre un problème inverse mal posé consiste à introduire une information à priori et à minimiser une fonctionnelle de régularisation incluant deux termes. Le premier terme est un terme d'attache aux données qui mesure l'adéquation entre les mesures et l'estimation de la fonction reconstruite. Le second terme impose un à priori sur la solution calculée et est appelé terme de régularisation. Un paramètre de régularisation équilibre les deux termes. Sa valeur a une grande influence sur l'image reconstruite [Scherzer *et al.* (2008)].

Les méthodes de régularisation diffèrent par le choix du terme de régularisation inclu dans la fonctionnelle à minimiser. Nous détaillons ici certains des termes de régularisation les plus utilisés ainsi que certaines fonctionnelles plus nouvelles. La régularisation par Variation Totale (TV) a été introduite par [Rudin *et al.* (1992)] pour résoudre des problèmes de débruitage. Par la suite cette régularisation a été appliquée à des problèmes de reconstruction d'image [Combettes and Pesquet (2004), Bioucas-Dias *et al.* (2006), Beck and Teboulle (2009)], d'inpainting [Chan and Shen (2002)] de zoom [Chambolle (2004)]. Cette régularisation est basée sur le calcul de la norme L_1 du gradient de l'image. La régularisation TV est largement utilisée dans de nombreuses application du fait de sa convexité et de sa capacité à préserver les bords. Cependant, les résultats de régularisation TV présentent des effets de marche d'escalier. Différentes approches ont été proposées pour résoudre ces problèmes. Farsiu et al. ont introduit en 2004 une régularisation TV améliorée qui considère une TV bilatérale pour un problème de super-résolution [Farsiu *et al.* (2004)]. Peyre et al. ont proposé un terme de régularisation TV non local appliqué pour les problèmes inverses comme la super-résolution, l'impainting ou l'échantillonnage compressé [Peyré *et al.* (2011)]. Des études plus récentes sur cette méthode de régularisation mettent en jeu des dérivées d'ordre plus élevé pour atténuer l'effet de marche d'escalier comme dans [Hu and Jacob (2012), Lefkimmiatis *et al.* (2012)a, Lefkimmiatis *et al.* (2012)b, Chan *et al.* (2000), Lysaker and Tai (2006), Yuan *et al.* (2009), Chambolle and Lions (1997), Chan *et al.* (2007), You and Kaveh (2000), Lysaker *et al.* (2003), Steidl (2005)]. La minimisation de la fonctionnelle de régularisation peut être réalisée par le biais de différents algorithmes. Nous nous sommes particulièrement intéressés à la méthode Alternate Direction Method of Multipliers (ADMM) [Boyd *et al.* (2011), Esser (2009)]. Le principe de cette méthode est de construire un Lagrangien augmenté avec une variable duale qui prend en compte les contraintes sur la fonction à reconstruire, et d'utiliser des

techniques de splitting des variables. La minimisation est effectuée de façon itérative sur la fonction à reconstruire, la fonction duale et la fonction splitée. Cette méthode est liée aux méthodes proximales. Ses propriétés de convergence ont été étudiées.

Déconvolution et super-résolution aveugle

Dans les problèmes de déconvolution et de super-résolution aveugles, l'image inconnue doit être reconstruite et dans le même temps le noyau de convolution doit être estimé. Une revue des méthodes variationnelles bayésiennes pour la déconvolution est présentée dans [Ruiz *et al.* (2015)]. Dans le cadre des méthodes variationnelles, des fonctionnelles incluant le terme d'attache aux données ainsi qu'une terme de régularisation sur l'image $\boldsymbol{f}$ et un sur le noyau de convolution $\boldsymbol{k}$ peuvent être considérées.

A partir de cette double régularisation, un certain nombre d'approches utilisent une minimisation alternée par rapport à $\boldsymbol{f}$ et $\boldsymbol{k}$ [You and Kaveh (1996), Chan and Wong (1998)]. Ceci sera l'approche utilisée dans ce travail. Des résultats de convergence dans le cas de la déconvolution ont été établis pour une régularisation de type Sobolev mais les résultats dépendent de $\overline{\boldsymbol{k}}$ et $\overline{\boldsymbol{f}}$, les premières grandeurs estimées [Chan and Wong (2000)]. Les conditions pour lesquelles une solution de norme minimum existe et est unique ont été étudiées dans la publication [Justen and Ramlau (2006)]. Une méthode de résolution non itérative est aussi proposée par les auteurs. Une approche similaire basée sur une minimisation alternée et des opérateurs proximaux est présentée dans [Abboud *et al.* (2014)].

La plupart des approches variationnelles pour les problèmes de déconvolution sont des approches à un seul niveau et l'image et la PSF apparaissent dans un seule fonction objectif à minimiser. Des méthodes plus élaborées comme une optimisation à deux niveaux pour trouver la PSF ont été présentées dans [Hintermüller and Wu (2015)]. Au premier niveau, une méthode de variation totale est imposée. D'autre part une fonctionnelle objectif est considérée qui incorpore l'information statistique sur l'image et la PSF.

Segmentation

Il existe une grande quantité de travaux concernant le problème de segmentation, voir par exemple la revue de [Aubert and Kornprobst (2002)]. L'objectif est de trouver une partition de l'image entre différentes régions. Les approches classiques sont souvent classées en approches contours ou régions. Toutefois, les méthodes variationnelles sont de plus en plus utilisées en segmentation d'images.
Des approches dans la littérature utilisent le contour actif géodésique et le formalisme level-set. D'autres approches sont basées sur la fonctionnelle Mumford-Shah avec comme inconnues la fonction intensité et les bords. Une des difficultés de cette méthode est d'approximer la fonctionnelle de régularisation. Le terme de régularisation inclut la mesure de Hausdorff de l'ensemble des bords qui étend la notion de bord à des ensembles non lisses. Des travaux ont montré que la fonctionnelle de Mumford Shah peut être utilisée pour la régularisation des problèmes inverses linéaires mal posés [Ramlau and Ring (2010), Jiang *et al.* (2014)]. Ces publications sont très intéressantes car dans la plupart des cas, les problèmes de déconvolution et de super-résolution sont considérés séparément pour le problème de segmentation. Récemment, des chercheurs ont étudié ces problèmes inverses avec le modèle de Potts qui est un cas particulier de la fonctionnelle de Mumford Shah [Storath *et al.* (2014), Weinmann *et al.* (2015)]. Ce travail utilise la norme L_0 du gradient

de l'image $\|\nabla \boldsymbol{f}\|_0$. Ce terme de régularisation est non convexe et la minimisation de la fonctionnelle de régularisation pose des problèmes de convergence et d'implémentation.

Chapitre 3 : Super-résolution basée sur la Variation Totale

Nous avons commencé notre recherche avec des techniques de restauration d'images pour la super-résolution.

Méthodes

Traditionnellement, la super-résolution requiert plusieurs images basse résolution [Chaudhuri (2002),Park *et al.* (2003)]. Notre objectif est d'améliorer la résolution d'images *in-vivo* et nous allons considérer le problème inverse de super-résolution à partir d'une seule image. Les images que nous utilisons montrent une structure quasi-binaire et nous nous sommes appuyés sur un a priori de variation totale (TV).

Cette méthode a été généralisée récemment avec les termes de plus haut degré (HDTV) en évitant l'effet de marche d'escalier [Hu and Jacob (2012)]. Ces fonctionnelles de régularisation sont basées sur une norme mixte $L_1 - L_2$ ou $L_1 - L_1$ des dérivées d'ordre plus élevées de l'image [Lefkimmiatis *et al.* (2012)a, Hu and Jacob (2012)]. Dans ces travaux, la fonctionnelle de régularisation HDTV est minimisée avec un algorithme majoration-minimisation. Des méthodes numériques diverses ont été utilisées pour résoudre ce problème de déconvolution régularisé par un terme TV [Becker *et al.* (2011), van den Berg and Friedlander (2008)]. Cependant des expériences numériques ont montré que les algorithmes basés sur la méthode des multiplicateurs avec une direction alternée, Alternating Direction Method of Multipliers (ADMM), font partie de l'état de l'art [Wang *et al.* (2008), Yang *et al.* (2009), Afonso *et al.* (2010), Ng *et al.* (2010)]. Dans ce chapitre, nous étendons la méthode de minimisation ADMM à la régularisation HDTV isotrope. Nous introduisons une formulation générale du terme de régularisation adapté aux deux méthodes, TV et HDTV isotrope. Un gradient conjugué préconditionné est proposé pour contourner les effets produits par le sous-échantillonnage et le sur-échantillonnage.

Expériences numériques

Afin de comparer les performances des deux approches de régularisation, les méthodes sont testées sur des images d'os détériorées de façon artificielle. Une comparaison avec une interpolation bicubique est aussi présentée. Du fait de leur très grande qualité nous avons utilisé comme images originales des images synchrotron micro-CT. Nous avons choisi quatre coupes à partir d'échantillons osseux différents, de forme de cylindre de 10 mm acquis avec une taille de voxel de 10 μm. Les volumes osseux ont été reconstruits à partir de 1500 projections 2D en utilisant l'algorithme de rétroprojection filtré (FBP) [Salomé *et al.* (1999)] puis sous échantillonné à 20 μm. Chaque région d'intérêt (coupe 2D) est artificiellement détériorée par un noyau Gaussien d'écart type $\sigma_{blur} = 4.85$, sous-échantillonnée par un facteur $p = 4$, puis bruitée avec un bruit Gaussien additif d'écart type $\sigma = 1$. La qualité de l'image obtenue a été mesurée avec le ratio PSNR. Comme notre but final est de quantifier la micro-architecture de l'os après segmentation, nous introduisons des paramètres supplémentaires calculées après segmentation. L'image est segmentée en appliquant le critère d'Otsu. Ensuite, nous calculons le coefficient de DICE, la surface osseuse (in mm^2), le nombre d'Euler (χ) qui reflète la connectivité. Pour chaque méthode, le paramètre de régularisation choisi μ est celui obtenu par un PSNR maximum. Pour une valeur donnée du paramètre de régularisation , l'algorithme ADMM a été appliqué pour obtenir le point selle du Lagrangien pour les régularisations TV et IHDTV et les valeurs de PSNR de l'images obtenues ont été calculées.

Résultats

Les résultats montrent que les méthodes basées sur la régularisation TV donnent des résultats similaires à celles basées sur IHDTV concernant le PSNR. Les coefficients DICE sont aussi très similaires. Cependant, les meilleurs résultats sont obtenus pour la surface osseuse pour la méthode TV. Le volume osseux et le nombre d'Euler sont des indicateurs important de la qualité osseuse. On peut voir que l'erreur est considérablement réduite par rapport à des images interpolés et encore d'avantage en comparaison avec l'image dégradée qui a la même résolution que celle utilisée dans les essais cliniques.

Conclusions

Dans ce chapitre, nous avons proposé d'améliorer la résolution spatiale d'images CT de la micro-structure d'os obtenues par techniques de super-résolution . Nous avons comparé l'interpolation standard avec des méthodes de super-résolution basées sur TV et sur la méthode récemment proposée de Isotropic Higher Order TV. Nous avons réécrit chaque terme de régularisation sous une forme similaire et présenté un schéma de minimisation efficace basé sur l'algorithme ADMM. La matrice hessienne en super-résolution n'a pas une structure circulante par blocs, et un algorithme de gradient conjugué préconditionné a été proposé pour accélérer les calculs. Une comparaison des approches de régularisation est faite sur des images basse résolution de la micro-strucutre de l'os en terme de PSNR, et de paramètres structuraux et de segmentation. Les deux méthodes TV améliorent les résultats de l'interpolation bicubique pour tous les critères. TV et IHDTV donnent des résultats similaires. Cependant, dans le contexte de la segmentation, TV est préférée car elle donne une image qui est plus proche d'un modèle constant par morceaux.

Chapitre 4 : Sélection du paramètre de régularization

Quand un problème inverse est résolu par des approches de régularisation, le paramètre qui équilibre les deux termes de la fonctionnelle a une très grande importance pour la qualité du résultat. Dans ce chapitre, nous nous intéressons au moyen de sélectionner ce paramètre de régularisation pour qu'il soit le plus proche possible du paramètre optimal. Nous proposons une méthode rapide et simple pour sélectionner ce paramètre de régularisation pour la restauration avec une régularisation TV d'une image f à partir d'une image bruitée, flou et sous-échantillonnée. Notre contribution dans ce domaine consiste à étudier une méthode itérative en utilisant une fonction modèle pour le terme de régularisation de Tikhonov [Kunisch and Zou (1998)].

Méthodes

Avec le principe de Morozov [Morozov (1984)], le paramètre de régularisation est choisi de telle sorte qu'il soit égal au niveau de bruit. Dans certains cas, l'utilisation du principe de Morozov peut ne pas conduire à un paramètre optimal. Comme suggéré dans [Kunisch (1993), Kunisch and Zou (1998)], une équation de Morozov modifiée peut être plus efficace. Nous proposons une nouvelle méthode itérative pour estimer le paramètre de régularisation optimal dans les problèmes inverses linéaires avec un terme de régularisation TV. Pour un paramètre donné, la fonctionnelle de régularisation TV est minimisée avec un algorithme ADMM. Notre approche est basée sur le principe de Morozov classique et sur une version modifiée de ce principe. Les propriétés de convergence de la méthode de régularisation pour ce choix du paramètre de régularisation ont été démontrées. En s'appuyant sur les propriétés de régularité du Lagrangien augmenté, il a été montré que le terme d'attache aux donnée peut être approximé par une fonction modèle simple. Cette fonction modèle est obtenue à partir des images reconstruites pour deux valeurs du paramètres de régularisation. Une valeur approchée du paramètre est calculée à partir de la fonction modèle qui approxime ce terme d'écart aux données. Ensuite, la solution est améliorée avec une méthode de Newton itérative sur la base du principe de Morozov ou de sa version modifiée. Nous présentons aussi brièvement la méthode UPRE (Unbiased Predictive Risk Estimator) qui sera utilisé pour des comparaisons avec nos méthodes itératives. L'approche UPRE a été étudiée en détail pour sélectionner le paramètre de régularisation Tikhonov [Vogel (2002), Blu and Luisier (2007), Eldar (2009), Ramani *et al.* (2008), Vaiter *et al.* (2013)]. Récemment, la méthode UPRE a été étendue au terme de régularisation TV et à des problèmes de grandes dimensions [Lin *et al.* (2010)].

Expériences numériques

Afin de montrer l'efficacité de la méthode pour choisir le paramètre de régularisation, nous avons considéré deux problèmes test, la déconvolution et la super-résolution. Dans le cas du problème de déconvolution l'image est floutée par une noyau Gaussien d'écart type σ_{blur} et bruitée par un noyau Gaussien d'écart type σ. Différents valeurs de bruit et floutage ont été appliqués sur plusieurs type d'images. Dans le cas de la super-résolution, l'image est aussi sous-échantillonnée par un facteur $p = 4$, ce qui augmente le caractère mal posé du problème.

Conclusions

Les approches proposées ont été comparées avec celles basées sur la méthode UPRE pour la déconvolution et la super-résolution, pour des bruits et des niveaux de flou différents et pour différentes images. Dans le cas de la déconvolution, le principe de Morozov modifié est la méthode la plus efficace pour le niveau de flou le plus élevé. Sinon, le principe de Morozov permet une meilleure estimation du paramètre de régularisation optimal. Pour le cas de la super-résolution, la méthode UPRE améliore le principe de Morozov. Cependant, une estimation plus précise du paramètre de régularisation optimal est obtenue avec le principe de Morozov modifié, où le terme d'attache aux données est pondéré par un terme TV. Les schémas itératifs basés sur cette nouvelle fonction modèle présentés dans ce travail sont très rapides et permettent d'éviter un balayage complet de l'ensemble des valeurs du paramètres de régularisation.

Chapitre 5 : Super-résolution/segmentation jointe

Dans ce chapitre, nous nous intéressons au problème conjoint de super-résolution et de segmentation, compte tenu que l'objectif final étant la quantification de la phase osseuse, il est nécessaire de disposer d'une image segmentée de l'os.

Méthode

Dans un problème de segmentation à deux phases, chaque voxel de l'image segmentée $\boldsymbol{s}$ se voit assigné à l'une ou l'autre des deux phases. Soit c_0 et c_1 le niveau de gris moyen de chaque phase. Une segmentation satisfaisante de l'image $\boldsymbol{f}$ est l'attribution d'un label tel que chaque voxel est assigné à une des phases dont le niveau de gris moyen est proche du niveau de gris correspondant de l'image $\boldsymbol{f}$ et ou les voxels voisins appartiennent le plus souvent à la même classe. On peut dont considérer la fonctionnelle suivante proposée par [Mumford and Shah (1989)]:

$$\int_{\mathscr{R}_0} [f(\boldsymbol{r}) - c_0]^2 \, \mathrm{d}\boldsymbol{r} + \int_{\mathscr{R}_1} [f(\boldsymbol{r}) - c_1]^2 \, \mathrm{d}\boldsymbol{r} + \nu|\Gamma| \tag{1}$$

où $\mathscr{R}_0$ et $\mathscr{R}_1$ sont les régions de chacune des deux phases et où $|\Gamma|$ dénote le périmètre de la frontière entre les deux régions $\mathscr{R}_0$ et $\mathscr{R}_1$.

Dans sa forme discrète, on est conduit au problème de minimisation suivant:

$$\arg\min_{\boldsymbol{s}\in\mathbb{B}} \quad \frac{\mu}{2}\|\boldsymbol{f} - \boldsymbol{s}\|_2^2 + \mathcal{R}_{\mathrm{TV}}(\boldsymbol{s}) \tag{2}$$

où $\mathbb{B} = \{c_0, c_1\}^{N'}$ est l'ensemble des N'-voxels des volumes des deux phase et $\mu = 2|c_1 - c_0|/\nu$.

Afin d'effectuer une super-résolution/segmentation jointe, nous considérons le problème d'optimisation suivant:

$$\arg\min_{\boldsymbol{s}\in\mathbb{B}} \ \frac{\mu}{2}\left\|\boldsymbol{A}\boldsymbol{s} - \boldsymbol{g}^{\delta}\right\|_2^2 + \mathcal{R}_{\mathrm{TV}}(\boldsymbol{s})\,. \tag{3}$$

où $\boldsymbol{g}^{\delta}$ représente l'image sous-échantillonnée, floutée et bruitée.
Ce problème de minimisation est très complexe pour des opérateurs linéaires très généraux $\boldsymbol{A}$. Nous avons donc effectué une minimisation approchée en considérant une relaxation convexe:

$$\hat{\boldsymbol{s}} \in \arg\min_{\boldsymbol{s}\in[c_0,c_1]^{N'}} \ \frac{\mu}{2}\left\|\boldsymbol{A}\boldsymbol{s} - \boldsymbol{g}^{\delta}\right\|_2^2 + \mathcal{R}_{\mathrm{TV}}(\boldsymbol{s})\,, \tag{4}$$

où l'ensemble des volumes à deux phases est remplacé par l'ensemble convexe des images à niveaux de gris dans $[c_0, c_1]$.
Cette méthode sera dénotée dans la suite TVbox, compte tenu de la contrainte sur les bornes.

Expériences numériques

A partir de ce chapitre les méthodes proposées ont été appliqués sur des volumes 3D. La vérité terrain binaire, de taille $328 \times 328 \times 328$, a été obtenue du volume micro-CT du synchrotron, présenté dans le chapitre 3, après avoir fait une segmentation avec la méthode d'Otsu. Cette référence a été floutée par une noyau Gaussien d'écart type $\sigma_{blur} = 2.425$ et bruitée par un noyau Gaussien d'écart type $\sigma = 0.01$ et $\sigma = 0.1$. Pour chaque niveau de

bruit, une comparaison entre les méthodes basés sur TV (TV et TVbox) et l'interpolation bicubique a été présenté en utilisant le coefficient DICE et les paramètres quantitatifs de l'os. Pour la méthode TVbox, un seuillage de 0.5 a été utilisé pour segmenter l'os dans les images quasi-binaires obtenues.

Résultats

Nous présentons les résultats obtenus pour des échantillons de taille $150 \times 150 \times 150$ sur la Figure 1 pour $\sigma = 0.1$. A partir de ces images on peut voir que la méthode TVbox est meilleure pour retrouver la micro-architecture osseuse et que c'est la méthode à privilégier pour résoudre le problème.

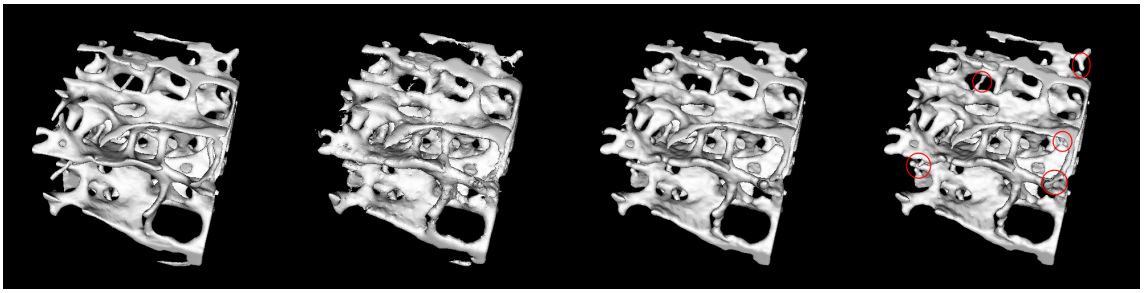

(a) Ground-truth (b) Low resolution (c) TV regularization (d) TVbox regularization

Figure 1: Comparison of 3D restoration methods for the noise level sigma=0.1.

Le coefficient DICE et les paramètres osseux quantitatifs (nombre d'Euler, connectivité, densité de connectivité et BV/TV) sont améliorés par les approches de régularisation basée par la Variation Totale. Les meilleurs résultats de reconstruction et les paramètres structuraux sont obtenus avec des contraintes additionnelles (méthode TVbox).

Conclusions

Dans ce chapitre, nous avons proposé une méthode de super-résolution/segmentation basée sur la régularisation par variation totale avec une contrainte convexe et une minimisation ADMM. Notre choix de paramètres de régularisation est basé sur une connaissance de la solution vraie du problème inverse. Nous comparons cette approche avec une méthode d'interpolation standard et une méthode de super-résolution TV sur les volumes basse résolution bruités, floutés en termes de coefficient DICE et de paramètres structuraux. De meilleurs résultats sont obtenus quand une contrainte convexe est incluse dans la fonctionnelle de régularisation TV. Nous observons que le volume osseux rapporté au volume total devient quasi exact et que la connectivité est aussi améliorée par rapport à l'image originale.

Chapitre 6 : Semi-aveugle super-résolution/segmentation jointe

Dans le chapitre 5, nous avons montré qu'un *a priori* basé sur la régularisation TV avec une relaxation convexe de la contrainte binaire (TVbox) peut améliorer la quantification (en particulier la connectivité) des images de micro-CT expérimentales détériorées de façon artificielle quand le noyau de flou est connu. Cependant, si l'on considère des données réelles, le problème est plus complexe car le noyau de convolution n'est pas connu et peut être difficile à estimer. Plusieurs méthodes ont été proposée pour la restauration simultanée d'une image et de la PSF comme les méthodes bayésiennes [Babacan *et al.* (2009), Molina *et al.* (2006)], la régularisation de Tikhonov [You and Kaveh (1996)] ou la régularisation par variation totale (TV) [Babacan *et al.* (2009), Chan and Wong (1998), Liao and Ng (2011)]. Estimer l'image inconnue et une PSF connue partiellement correspond à une déconvolution semi-aveugle [Galatsanos *et al.* (2000), Molina (1994)]. Nous nous sommes donc intéressé au problème semi-aveugle de super-résolution/segmentation jointe qui vise à estimer à la fois l'image segmentée super-résolue et le noyau de convolution partiellement connu. Des résultats préliminaires sur des images expérimentales HR-pQCT sont présentés.

Méthode

Dans une première approche, nous supposons que le noyau de flou est isotrope et peut être représenté par un noyau 3D Gaussien. Notre problème se ramène à trouver une image segmentée super-résolue et l'écart type σ du noyau Gaussien. Notre approche est basée sur le même à priori TVbox. Nous notons que la fonction de coût est convexe par rapport à $\boldsymbol{f}$ mais non convexe par rapport à la l'écart type σ. Pour trouver la solution $\{\boldsymbol{f}, \sigma\}$ nous alternons entre deux étapes de minimisation jusqu'à convergence. Un algorithme itératif est utilisé qui revient à fixer une des inconnues et à minimiser la fonction de coût par rapport à l'autre variable. Quand le noyau de convolution est fixé, la minimisation de la fonction de coût est équivalente à l'approche présentée au chapitre 5 qui s'appuie sur la méthode ADMM. Quand l'image segmentée restaurée est fixée à la solution ADMM seuillée obtenue à la première étape, une méthode de Newton est appliquée pour estimer σ. A la fin, une valeur optimum locale de σ est trouvée.

Expériences numériques

L'approche semi-aveugle est appliquée au même volume trabéculaire décrit aux chapitres 3 et 5 pour comparaison avec l'approche non-aveugle TVbox. Un sous échantillonage de 2 et un noyau Gaussien de $\sigma = 2.4$ sont étudiés. Un bruit Gaussien avec une déviation standard de 0.1 est appliqué à l'image quasi-binaire. Des indicateurs de la segmentation comme le DICE ou des paramètres quantitatifs de l'os sont calculés. Le paramètre de régularisation est optimisé par rapport à l'image idéale.

Données réelles

Nous avons exploité des données réelles d'échantillons osseux acquises à l'Université de San Francisco. Des images 3D de radius humain ont été acquise sur un système HR-pQCT à partir de 750 projections et reconstruites avec une taille de voxel de 82 μm. Les mêmes échantillons ont aussi été scannés en utilisant un système micro-CT qui fournit des images 3D de 24 μm. Les images HR-pQCT ont été recalées sur l'image de micro-CT ré échantillonnée à 41 μm.

Résultats

De bons résultats sont obtenus sur des images test détériorées de façon artificielle. Notre hypothèse gaussienne sur le noyau de convolution est valide dans ce cas. Pour des images réelles, seule l'approche semi-aveugle peut être appliquée. Les résultats montrent que pour le cas réel les autres paramètres devraient être pris en considération comme une ré-estimation des paramètres c_0 et c_1 de la contrainte convexe.

Conclusions

Dans ce chapitre, nous avons proposé une méthode semi-aveugle de super-résolution/ segmentation basée sur la régularisation par variation totale avec une contrainte convexe et une minimisation ADMM pour améliorer la quantification de la micro-architecture de l'os trabéculaire à partir de volumes HR-pQCT ou de micro-CT. Nous avons comparé les approches semi-aveugle TVbox avec la méthode standard d'interpolation en terme de DICE et de paramètres structuraux. Pour des images synchrotron micro-CT détériorées de façon artificielle, une comparaison avec la méthode TVbox est présentée. Nous montrons que notre méthode semi-aveugle améliore les paramètres structuraux comparés aux paramètres originaux et que nous pouvons estimer le noyau de convolution. Elle améliore clairement la méthode d'interpolation et pour des images artificiellement floutée, l'approche semi-aveugle TVbox donne des résultats proches de ceux de la méthodes non aveugle. Ces résultats peuvent être un point de départ pour l'analyse des images réelles HR-pQCT pour lesquelles nous possédons une image de référence. Les résultats obtenus sur les données réelles doivent être améliorés. De nombreux aspects doivent être testés comme l'optimisation des paramètres de l'algorithme ou le choix de c_0 et c_1 pour la contrainte convexe. Un noyau anisotrope et variant spatialement peut aussi être considéré.

Conclusion et perspectives

Dans cette thèse, nous nous sommes intéressés à des méthodes susceptibles d'améliorer la quantification de la micro-architecture osseuse à partir d'images HR-pQCT. De façon spécifique, notre but était d'explorer les méthodes de super résolution en considérant que ces images étaient floues, bruitées et sous échantillonnées. De plus, compte tenu que le but final est d'obtenir des paramètres quantitatifs calculés sur une image binarisée de la micro-architecture osseuse, nous nous sommes intéressés au problème combiné de super-résolution et de segmentation. Pour cela, nous avons utilisé des approches variationnelles avec différents termes de régularisation. Nous nous sommes aussi intéressés au problème du choix du paramètre de régularisation. Les différentes approches ont été testées sur des images 2D et des volumes 3D, obtenus par simulations ou issus de données réelles d'échantillons osseux.

Dans un premier temps, nous avons étudié les méthodes de super-résolution 2D basées sur la variation totale TV. La méthode classique de régularisation TV a été étendue à une régularisation TV de plus haut degré car le terme TV du premier ordre crée des effets de marche d'escalier. Nous avons étendu la méthode de minimisation ADMM à la régularisation isotrope HDTV. Nous avons introduit une formulation générale du terme de régularisation pour les deux méthodes et nous avons présenté un algorithme de minimisation efficace. Ces termes ont été étudiés dans ce travail car ils constituent les approches les plus utiles pour des problèmes joints super-résolution/segmentation avec des valeurs quasi-binaires. Une comparaison des méthodes a été faite sur des images basse résolution de la structure osseuse en termes de PSNR et de paramètres structuraux et de segmentation. Les approches basées sur la variation totale ont amélioré les méthodes standards d'interpolation. Néanmoins, les méthodes TV et IHDTV ont montré des résultats de reconstruction similaires.

Nous avons présenté ensuite une nouvelle méthode de choix du paramètre de régularisation pour la régularisation TV. Cette méthode généralise le principe de Morozov classique. La convergence de la méthode de régularisation TV avec ce choix à postériori du paramètre de régularisation a été étudiée. L'algorithme qui permet de choisir le paramètre optimal est très rapide. Des comparaisons numériques ont été présentées avec d'autres méthodes comme UPRE. Plusieurs images et niveau de bruits ont été testés. De très bons résultats ont été obtenus avec notre méthode qui permet d'améliorer les approches existantes.

La partie suivante de ce manuscrit concerne le problème joint de super-résolution/ segmentation à 3 dimensions. Les problèmes de super-résolution et de segmentation sont souvent considérés de façon séparés. Dans cette partie, nous avons essayé de résoudre ces deux problèmes en même temps. La méthode a été basée sur une convexification de la fonctionnelle avec des contraintes convexes supplémentaires. La méthode de minimisation a dû être modifiée pour inclure cette contrainte convexe. Des résultats ont été présentés sur des volumes 3D. Les résultats de reconstruction et la connectivité ont été améliorés par cette nouvelle contrainte.

Le dernier chapitre de cette thèse concerne une méthode semi-aveugle de segmentation et super-résolution conjointe. Un algorithme de minimisation alterné a été utilisé pour reconstruire les images et le noyau de convolution qui a été supposé Gaussien. Cette approche a été testée sur des images d'os issues du synchrotron ESRF. L'approche semi-aveugle a amélioré les paramètres structuraux et a conduit à une très bonne estimation du noyau de convolution. Cette thèse a été un travail préliminaire sur le problème inverse difficile qui nous intéresse. De nombreux aspects restent à étudier. Une première extension possible de ce travail est l'utilisation de nouveaux terme de régularisation comme le terme

de régularisation de Potts par exemple. Cela pose des problèmes difficiles de minimisation de la fonctionnelle de régularisation mais cela pourrait permettre d'améliorer les résultats de reconstruction. Une méthode de choix du paramètre de régularisation a été proposée pour la régularisation TV appliquée à la super-résolution. Cependant, il pourrait être intéressant d'étudier des méthodes adaptatives du choix du paramètre pour des problèmes de reconstruction plus difficiles. Dans ce travail, nous avons régularisé la fonctionnelle de régularisation avec des termes liés à l'image. Des fonctionnelles plus complexe peuvent être utilisées et le problème du choix des différents paramètres étudié plus précisément. La minimisation de la fonctionnelle de régularisation a été mise en œuvre avec l'algorithme ADMM. La comparaison avec les méthodes proximales est une perspective de recherche intéressante. Une validation plus réaliste de la méhode de minimisation alternée doit être faite sur des images ex-vivo HR-pQCT pour lesquelles des images de référence de micro-CT sont disponibles. Le problème de super-résolution aveugle doit aussi être étudié sur des données simulées et des images réelles. Différentes approches mentionnées dans le chapitre bibliographique sur les problèmes inverse peuvent être comparées. Les approches non itératives de [Ramlau and Ring (2007)] et la méthodologie bilevel sont des directions de recherches futures intéressantes.

Introduction

Osteoporosis is a disease that affects the strength of the bones and is characterized by a decrease of bone mineral density (BMD) and an alteration of the trabecular bone micro-architecture. Responsible for fractures and vertebral compression that can lead to invalidity and even cause death, osteoporosis or related bone loss diseases have been attracting the interest of many groups of clinicians and researchers from few decades ago. Statistics show that 40% of women and 13% of men over the age of 50 are diagnosed with osteoporosis and 24% of aged patients die every year after a hip fracture. Nowadays, the osteoporosis diagnosis is based on the measurement of BMD using dual X-ray absorptiometry (DXA) technique. However, this technique can estimate between 60% and 70% of the fracture risk. Thus, new bone fragility evaluation techniques that involve quantification of bone micro-architecture are being developed.
X-Ray micro-CT provides 3D images at spatial resolution higher than clinical CT systems. It has been particularly used to analyze bone micro-architecture in the study of osteoporosis, a bone fragility disease, still difficult to diagnose [Seeman and Delmas (2006), Peter and Peyrin (2011)]. Bone micro-architecture which is an important determinant of biomechanical strength is made of a complex arrangement of thin structures called trabeculae, having a thickness around 150 μm. The 3D images of bone micro-architecture obtained with X-Ray micro-CT are further processed to extract 3D quantitative descriptors of the bone micro-structure. Bone structure analysis requires an image segmentation method as a first step to extract the bone from the background. Then it is considered the calculation of 3D morphometric parameters such as bone volume to total volume ratio, mean trabecular thickness, mean trabecular spacing, but also topological parameters, such as connectivity or the micro-structure organization in plate or rods [Hildebrand *et al.* (1999), Peyrin *et al.* (2010)]. Such descriptors have been reported in many studies but limited to the analysis of *ex vivo* bone samples. While the spatial resolution of clinical CT scanners is not sufficient to resolve the trabecular structure, new High Resolution peripheral Quantitative CT (HR-pQCT) systems have been commercialized to investigate bone micro-architecture *in-vivo* at peripheral sites (tibia and radius) [Boutroy *et al.* (2005)]. The obtained 3D images are segmented and the same parameters as those used in X-ray micro-CT are calculated to quantify the bone micro-architecture of patients. However, the result of image segmentation can be poor, compromising the subsequent quantification [Tjong *et al.* (2012)]. This problem is related to the limited physical spatial resolution of the HR-pQCT which is close to the trabecular thickness.

The aim of this thesis is to improve the quantification of the trabecular bone microstructure from *in-vivo* HR-pQCT images. We propose the investigation of super-resolution methods and joint super-resolution/segmentation methods based on variational approaches. The proposed approaches validation is performed on experimental high-resolution micro-CT images of bone samples at 20 μm after simulating the effect of spatial resolution loss and degradation by blur and noise. Also, a more realistic validation is performed on ex-

vivo HR-pQCT images for which the correspondent ground-truth micro-CT images are available.

The outline of the thesis is the following:
Chapter 1 - Medical context
Chapter 2 - Background (theoretical aspects)
Chapter 3 - Total Variation based super-resolution
Chapter 4 - Regularization parameter selection
Chapter 5 - Joint super-resolution /segmentation
Chapter 6 - Semi-blind joint super-resolution /segmentation
Conclusion and perspectives

In the first chapter, we detail the medical context of this thesis. The high quality bone micro-architecture images are acquired at the European Synchrotron Radiation Facility (ESRF) in Grenoble. The bone micro-structure is presented together with investigation methods of this micro-architecture, and especially the HR-pQCT studies. The relevant parameters to quantify the structure are detailed.

In the second chapter, we present some aspects of the theoretical background regarding inverse problems and regularization methods, especially for image processing applications as super-resolution and segmentation. The super-resolution problem can be understood as an ill-posed linear inverse problem like the other image processing problems, the denoising or deconvolution. This type of problems has been much studied and we summarize in this chapter the basic definitions in the field. Regularization methods can be used to obtain stable solutions. We follow in this thesis a variational approach and a regularization functional is constructed to solve the problem. Different regularization terms are presented in this chapter. An example is the Total Variation (TV) term that has attracted much interest in recent years. The balance between the data term and the regularization penalization is controlled by a regularization parameter which is crucial and difficult to choose. This choice may be based on the noise level or not. The basic parameter selection methods are described. Moreover, several methods can be used to minimize the regularization functional. We focus here on the ADMM (Alternate Direction of Minimization method) which is among the state of the art methods. We end this chapter with generalities about segmentation and about metrics of image reconstruction quality.

In chapter 3, we investigate the super-resolution 2D methods based on TV. This type of regularization term is very useful to restore piecewise constant images but it is well-known to create staircasing effects. Therefore, we will try to use also higher order regularization terms similar to TV. These TV terms will be considered because they may represent more useful approaches for mixed super-resolution/segmentation problems with quasi-binary values. We extend the ADMM minimization method to isotropic HDTV (Higher Degree TV) regularization. Then, we introduce a general formulation of the regularization term suited to both methods, TV and isotropic HDTV based on linear differential operator. These higher order terms will be taken into account because they are expected to decrease the staircasing effects that deteriorate the reconstruction.

In chapter 4, we present a new method of choice for the TV regularization parameter. This method is based on an estimation of the noise level and it is a generalization of the classical Morozov principle used for Tikhonov regularization. A modified principle is presented together with a very fast algorithm to choose the parameter based on this principle. Comparison results are presented with other methods for choosing the regularization parameter like the Unbiased Predictive Risk Estimator.

Chapter 5 is devoted to the joint super-resolution /segmentation problem in 3D. The

super-resolution and segmentation problems are often studied with variational approaches but in most cases they are considered separately. In this chapter, we try to solve both problems at the same time with a variational method. The basis of the method is a convexification of the regularization functional with additional box constraints. The minimization method must be modified to include this convex constraint. Results are presented on 3D micro-CT volumes.

The last chapter presents a semi-blind joint super-resolution/segmentation method. An alternate minimization algorithm is used to recover the images and the blur kernel which is assumed to be a Gaussian kernel. This approach is validated on test and real images.

We end the manuscript with some conclusions and perspectives.

Chapter 1

Medical context

1.1 Bone tissue

Bones form the skeletal system which is part of the locomotor or musculoskeletal system. The skeletal system is responsible for the stability, movement, shape and form of the body. Moreover, bones are storing minerals (as calcium and phosphorus), producing blood for the body and protecting vital organs. The most important bones with protecting functions are the skull for the brain and the rib cage for the heart and lungs.
The two types of bone tissue are the cortical and the cancellous (trabecular or spongy) bone. The cortical bone, also called the compact bone, is a dense external shell that constitutes 80% of the total human skeleton and is located primarily in the peripheral skeleton. For each bone, the amount of each type of tissue can differ considering the function that bone has. The structure of the bone tissues is presented in Figure 1.1.

The compact bone is organized in osteons that are composed of successive concentric lamellae. This regularly arrangement contributes to the bone strength by resisting banding. Also, the compact bone is considered dense because the spaces between the osteons are filled with layers of hard bone matrix called interstitial lamellae. Osteons include also a complex network of canals: the Haversian canals which are longitudinally oriented through the center of osteons and the ones perpendicular to it, the Volkmann canals.

The trabecular bone forms 70% of the axial (central) human skeleton. It has the form of a honeycomb of vertical and horizontal bars called trabeculae. Here, in these regions, is located the red marrow.

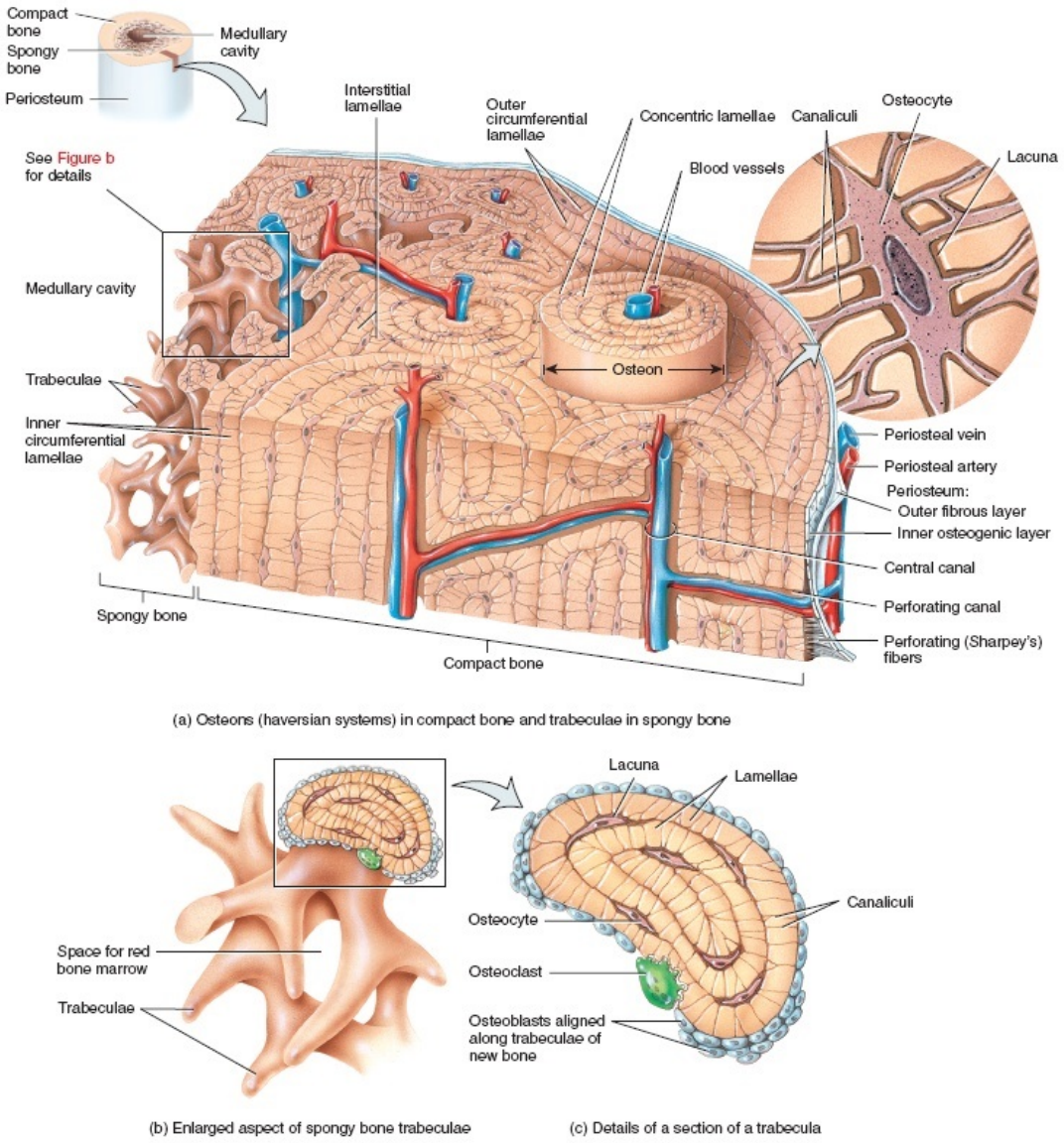

Figure 1.1: The structure of the compact and trabecular bone tissues (http://higheredbcs.wiley.com/).

Bone modeling and remodeling

From birth to adulthood the skeletal is changing in form and gaining in mass (for example long bones are increasing in length and diameter). The process responsible for these changes is called bone modeling and is characterized by bone resorption and bone formation taking place on separate surfaces.

During lifetime, the old bones are replaced with the new ones through a process called bone remodeling, which allows bone to adapt to mechanical constraints. Thus the bones are sequentially resorbed and reconstructed. Bone remodeling has an annual turnover rate of about 25% in trabecular bone and only 2-3% in cortical bone. After bone reconstruc-

tion its mineral concentration in localized regions increases progressively and the bone can be seen as an arrangement of bone modeling units (BMU) with different degrees of mineralization [Peter and Peyrin (2011)].

The main cells involved in bone remodeling are presented in Figures 1.2, 1.4 and are described in the following:

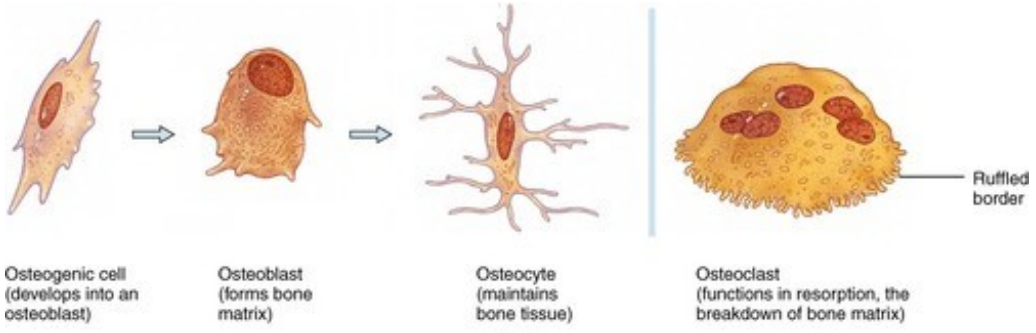

Figure 1.2: Bone cells (http://www.uaz.edu.mx/histo/TortorAna/ch06)

Osteoclasts are cells of large dimensions, that have more than one nucleus per cell and proceed from the hematopoietic lineage. They are attached to the bone surface at sites of active bone resorption and hold responsability for the mineralized tissue resorption. Through a ruffled edge, these cells secret bone-resorbing enzymes that digest the bone matrix.

Osteoblasts are derived from mesenchymal stem cells and fulfil the bone formation function of refilling the cavities made by octeoclasts (bone matrix synthesis and its subsequent mineralization).

Lining cells cover the majority of adult skeleton surface in the absence of osteoblasts and osteoclasts.

Osteocytes are osteoblasts gradually integrated within the newly formed osteoid, which in the end becomes calcified bone. Osteocytes located deep into bone matrix maintain contact with the ones newly integrated in the osteoid. Furthermore, they preserve junction with osteoblasts and bone lining cells placed on bone surfaces, through an expended network of cell processes (canaliculi). They are considered ideally located to respond to alterations in physical forces upon the bone and to transduce messages to cells on the bone surface, guiding them to initiate resorption or formation responses.
Moreover, osteocytes can be found in the cortical tissue, spread within the concentric lamellae and in the trabecular bone. They form a complex network (see Figure 1.3) considered significant in maintaining the viability and structural integrity of the bone.

Bone matrix

Osteoids are made of noncollagenous proteins and type I collagen (94%). Mineral salt, a crystalline complex of calcium and phosphate (hydroxyapatite), is a component of the osteoid's matrix. Due to the presence of this salt, the bone presents the features of hardness and rigidity. The structure of a calcified bone is the following: 70 % inorganic

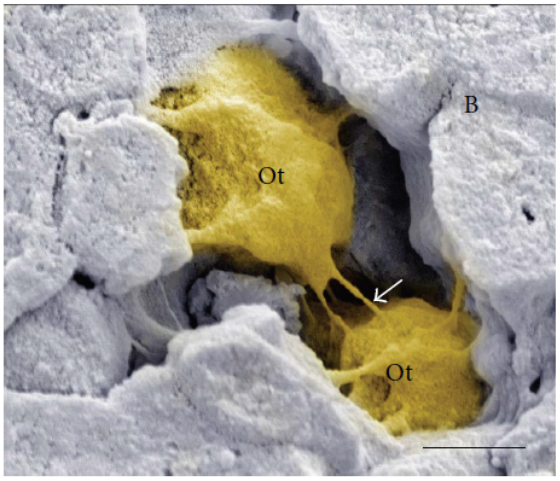

Figure 1.3: Scanning electron micrography showing the interconnected network (arrows) formed by two osteocytes (Ot) surrounded by bone matrix (B). Scale bar: 2 μm [Florencio-Silva *et al.* (2015)].

mineral (hydroxyapatite), about 25 % organic matrix (2-5% of which are cells) and 5% water.

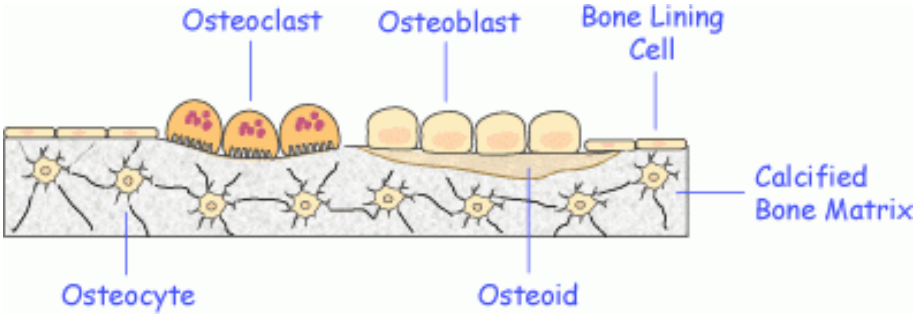

Figure 1.4: The bone cells involved in the remodeling process (http://www.iofbonehealth.org).

1.2 Osteoporosis

Osteoporosis is defined by the World Health Organization (WHO) as a systemic skeletal disease characterized by low bone mass and micro-architectural deterioration of bone tissue, leading to enhanced bone fragility and a consequent increase in fracture risk [$Consensus1991, Consensus1993$].

Osteoporosis is a disease which in most of the cases affects the aged persons. After the age of 50, 40% of the women and 13% of the men are affected by osteoporosis. Also, 24% of the aged patient die every year after having a hip fracture [Peter and Peyrin (2011)].

The most frequent and important of the related fractures are shown in Figure 1.6 and

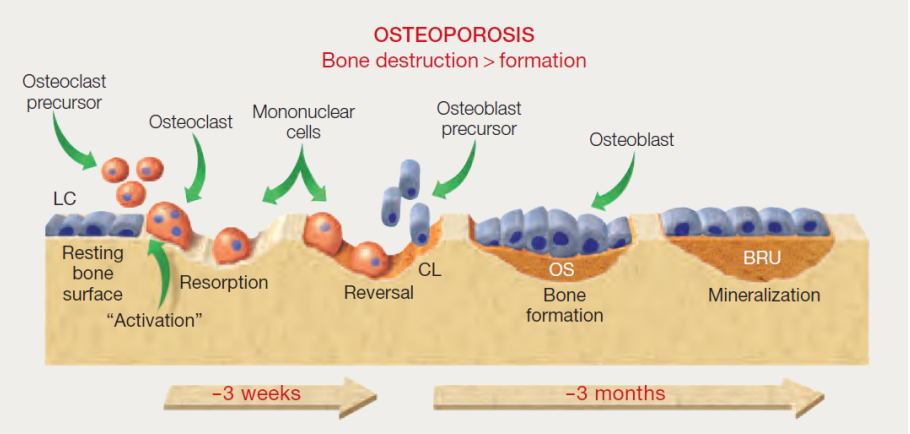

Figure 1.5: Representation of the bone remodeling cycle in osteoporosis. Osteoporotic bone shows an increase in the length of the remodeling cycle and reduced capacity to lay down a new mineralized bone matrix. Abbreviations: BRU, bone remodeling unit; CL, cement line; LC, lining cells; OS, osteoid. (www.medscape.com)

are those of the proximal femur, vertebrae and distal forearm (Colles' fracture) [Melton *et al.* (1989)].

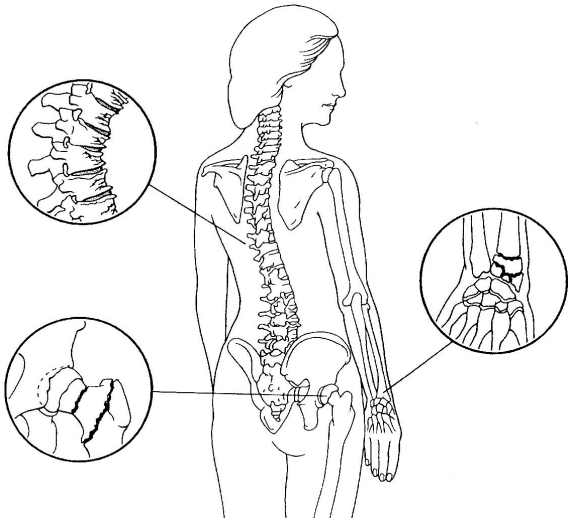

Figure 1.6: Bone fractures areas in osteoporosis [Office of the Surgeon General (US) (2004)].

Figure 1.7 presents the alteration of the trabecular micro-structure and the low bone mass in the case of osteoporosis localized at proximal femur.

Compression fractures of thoracic vertebrae lead to loss of height and progressive thoracic kyphosis. Lower ribs eventually rest on ileac crests and downward pressure on viscera causes abdominal distention (see Figure 1.8) [Office of the Surgeon General (US) (2004)].

In [Riggs and Melton III (1983)] are presented two distinct syndromes of the involutional osteoporosis (the common form of osteoporosis):

- Type I (postmenopausal): typically affects women within 15-20 years after their

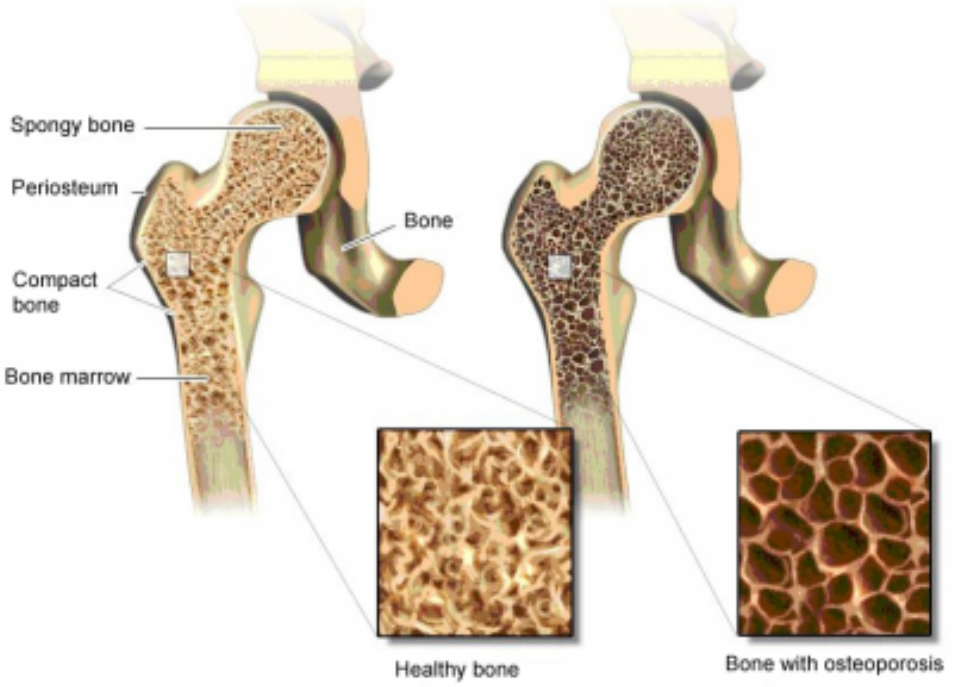

Figure 1.7: Osteoporosis Bone (https://www.informedhealth.org/osteoporosis.2610.en.html)

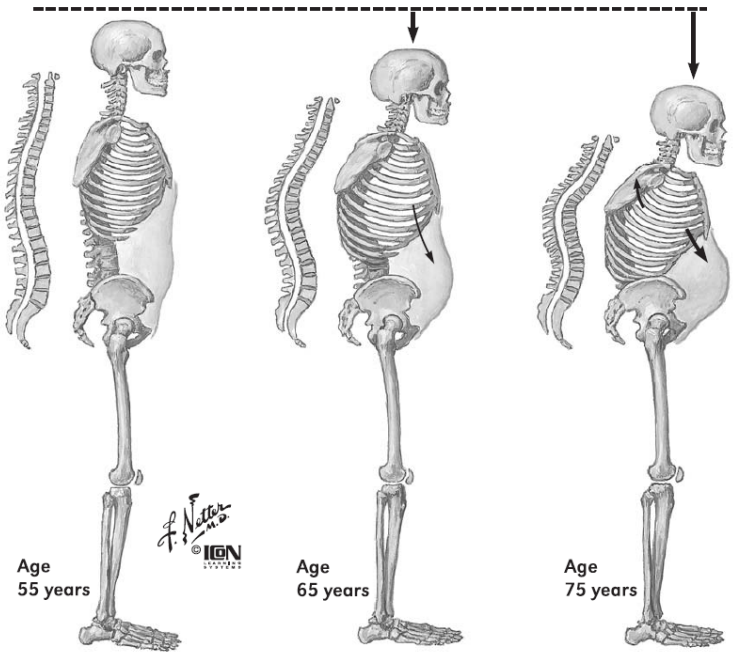

Figure 1.8: Progressive spinal deformity in osteoporosis [Office of the Surgeon General (US) (2004)]

menopause and the loss of trabecular bone is more predominant, resulting in fractures of

vertebrae and wrist.

- Type II (age-related): can occur at any age but the predominant form is in both men and women age 70 and older; it is twice as common in women. In this case both cortical and trabecular bone are lost, resulting in hip fractures as well.

Osteoporosis is diagnosed (conform the World Health Organization) when the bone mineral density (BMD) is 2.5 standard deviations or more below the mean peak bone mass (average of young, healthy adults) as measured by dual X-ray absorptiometry (DXA). This system is a two-dimentional, projection-based radiographic technique at two energy spectrum that measures integral BMD of both cortical and trabecular bone (areal BMD). The number of standard deviations of the BMD is called T-score. Figures 1.9 and 1.10 present the distribution of the BMD in healthy woman aged 30-40 years and in women of different ages.

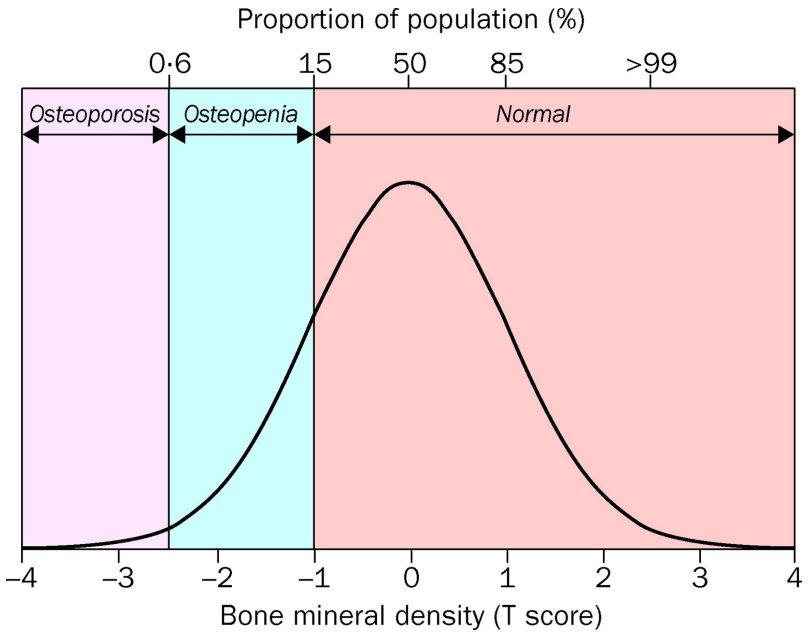

Figure 1.9: Distribution of bone mineral density in healthy women aged 30-40 years [Kanis (2002)]

However, the BMD can estimate between 70% and 75% of the variance in strength [Ammann and Rizzoli (2003)]. The remaining variance is due to bone macro- and micro-structure, tissue composition and microdamage [Seeman and Delmas (2006), Chapurlat and Delmas (2009)]. Therefore, it becomes necessary to develop new bone fragility evaluation techniques in particular methods taking into account bone micro-architecture.

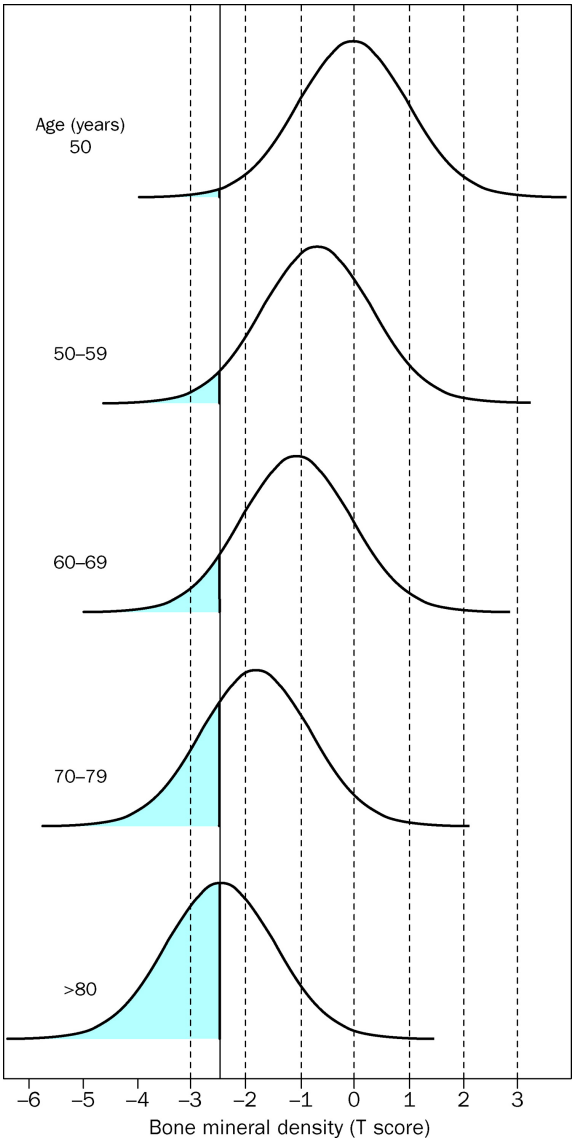

Figure 1.10: Distribution of bone mineral density in women of different ages, and the prevalence of osteoporosis (blue). T score below -2.5 = osteoporosis [Kanis (2002)].

1.3 Conventional investigation of bone micro-architecture

Histomorphometry represents the conventional evaluation technique of the bone architecture but other non-destructive image based techniques are more and more used for this purpose. Still, systems as micro-CT can not provide information about cellular function and remodeling activity, which continues to be the domain of bone histology [Burghardt *et al.* (2011)].

Figure 1.11 shows the trabecular bone in a normal postmenopausal women and in a subject with postmenopausal osteoporosis. The loss of bone volume and trabecular connectivity is strongly associated with the latter case.

At the trabecular bone level, morphometric parameters such as the trabecular bone

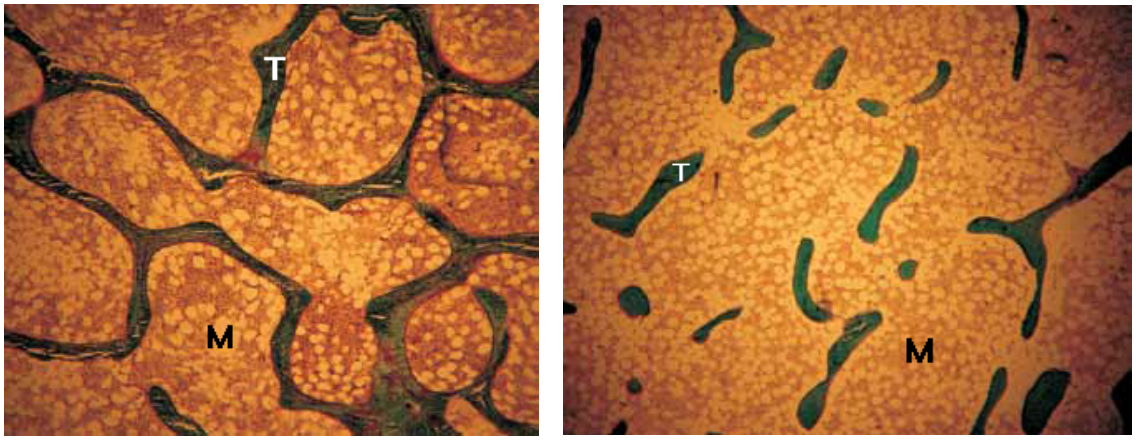

(a) (b)

Figure 1.11: (a) Trabecular bone in a normal postmenopausal woman. Note well preserved trabecular connectivity. (b) Trabecular bone in a subject with postmenopausal osteoporosis demonstrating marked reduction in cancellous bone volume and loss of connectivity. (T: trabeculae; M: marrow) [Kulak and Dempster (2010)]

volume fraction (the ration of bone volume to total volume BV/TV), trabecular thickness (TB.Th), trabecular separation (Tb.Sp) and trabecular number (TB.N) are traditionally assessed from bone biopsies by two-dimensional histomorphometry [Parfitt *et al.* (1987)]. From the other measured parameters, we recall the Euler number [Odgaard and Gundersen (1993)], that offers relevant information about the connectivity of the bone structure.

1.4 X-ray investigation of bone micro-architecture

1.4.1 Principle of X-ray CT

The principle of X-ray CT relies on a data acquisition step followed by a data processing step. During data acquisition, attenuations of X-ray beams passing through the body are measured on 1D or 2D detector, providing one projection. The X-ray source is then sequentially rotated and new measurements are collected. When a complete rotation angle of 180^o has been done, the data are processed through an image reconstruction algorithm based on Radon transform [Feldkamp *et al.* (1984)] providing a digital image. The bone matrix is composed from calcium hydroxyapatite that assures a high contrast in CT images between soft and mineralized tissues.

1.4.2 Clinical CT and Quantitative CT

Clincal CT allows to obtain images up to a spatial resolution around 500 μm in the transverse direction. If it is well adapted for imaging bone at the organ level, its spatial resolution is limited for the quantification of bone trabeculae.

To measure volumetric BMD and to be able to characterize the bone geometry and density, 3D quantitative CT (QCT) can be used. Compared to DXA, this technique

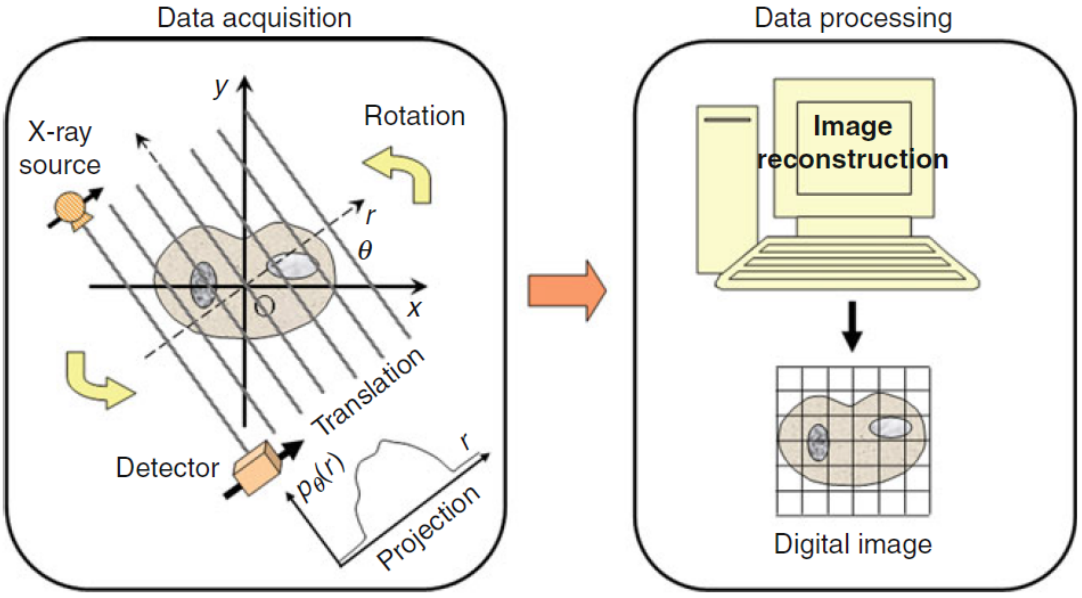

Figure 1.12: The two steps of data acquisition and data processing in the first generation of X-ray CT. [Peyrin and Engelke (2012)]

can examine cortical and trabecular BMD independently. Although it involves greater radiation exposure, it may be used as an alternative to spine and hip DXA measurements. For this purpose, a calibration phantom made from objects with known hydroxyapatite (HA) concentrations, which is the major constituent of bone mineral, will be scanned together with the patient. The BMD_{tiss} value of a given pixel will be calculated from the CT value, CT_{tiss}, of the pixel by:

$$BMD_{tiss} = CT_{tiss} \frac{200}{CT_{200} - CT_0}, \tag{1.1}$$

where CT_{200} and CT_0 are the measured CT values for HA concentration of 200 mg/cm^3 and water equivalent material without HA (HA=0 mg/cm^3) that compose the phantom. In 2015, The International Society for Clinical Densitometry (ISCD) gave new official position regarding the use of QCT and pQCT. We recall herein the main of them:

- For density-based QCT measurements the in-scan calibration phantom can be replaced by asynchronous calibration if scanner stability is maintained.

- Femoral neck and total hip T-scores calculated from 2D projections of QCT data are equivalent to the corresponding DXA T-scores for diagnosis of osteoporosis in accordance with the WHO criteria.

- Total femur trabecular BMD measured by QCT predicts hip fractures as well as hip BMD measured by DXA in postmenopausal women and older men.

1.4.3 Micro-CT

An important alternative evaluation method of bone micro-architecture is the 3D X-ray microtomography (micro-CT), a non destructive technique which provides 3D images with a high and isotropic spatial resolution in each direction. Moreover, this technique avoids sample preparation. CT systems having a spatial resolution between 1 and 100 μm are referred to as micro-CT systems and can evaluate ex-vivo the human bone micro-architecture. Moreover, these systems can offer the possibility of longitudinal in-vivo investigations in small animals, such as mice and rats.

The first micro-CT scanner developed for the evaluation of the three-dimensional micro-structure of trabecular bone was described in [Feldkamp *et al.* (1989)]. Starting with the first commercially available bone micro-CT scanner in 1994, this technique became a standard in bone research [Rüegsegger *et al.* (1996)].

A cone-beam with a polychromatic X-ray source is typically used for conventional laboratory micro-CT. For dedicated ex-vivo scanners the source and detector remain in a fixed position during the scan, while the specimen rotates in the field of view. Conversely, in the case of preclinical micro-CT systems for small animals, the x-ray source and detector are rotating and translating about the field of view while a fixed gantry is utilized.

There are many studies in the last two decades investigating the age and gender related changes on the bone structure using micro-CT images [Hildebrand *et al.* (1999), Ding *et al.* (2002), Hulme *et al.* (2007)]. In the clinical research, a minimally invasive bone biopsy is typically acquired from the iliac crest [Jiang *et al.* (2005)]. The trabecular micro-architecture of these type of samples it correlated to vertebral fractures, as shown in [Ito *et al.* (1998), Genant *et al.* (2006)]. Moreover, as presented in [Akhter *et al.* (2007)], the changes of the bone micro-structures caused by menopause may be observed on micro-CT scan of iliac crest (Figure 1.13).

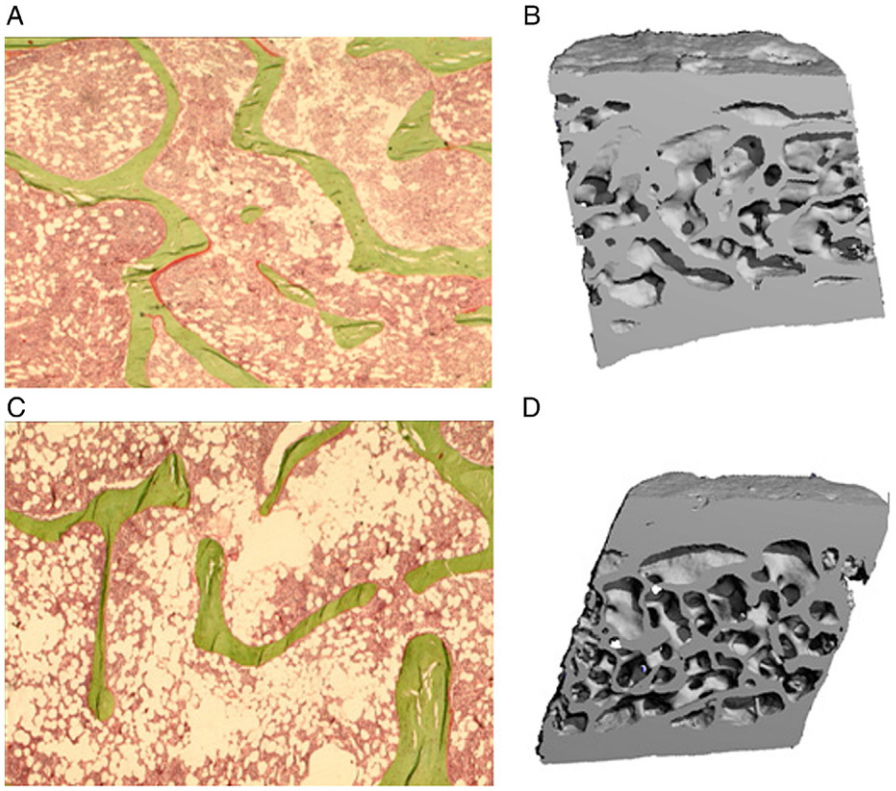

Figure 1.13: A typical pre- and post-menopausal bone biopsy; histomorphometry (A and C) and micro-CT scan (B and D) from a single subject is shown. The micro-CT scan for post-menopausal shows greater trabecular spacing as compared to that of the pre-menopausal iliac crest bone biopsy [Akhter *et al.* (2007)].

1.4.4 Synchrotron Micro-CT

Synchrotron Micro-CT technique is offering better image quality with higher signal to noise ratio (SNR) in smaller acquisition times compared to X-ray micro-CT. Thus Synchrotron micro-CT is often used as a reference technique to evaluate emerging imaging modalities.

A spatial resolution between 5-10 μm is appropriate to study bone micro-structure. In 1989, Engelke was the first who showed the feasibility of 3D Synchrotron micro-CT of bone samples [Engelke *et al.* (1989)]. In 1994, Bonse presented 3D images of iliac biopsies with a cubic voxel size of 8 μm [Bonse *et al.* (1994)].
At the European Synchrotron Radiation Facility (ESRF), Figure 1.14, located in Grenoble (France), Peyrin et al. developed a 3-dimensional synchrotron micro-tomography to study bone architecture [Salomé *et al.* (1999)] at beamline ID 19. The setup of this beamline is presented in Figure 1.15.

The ESRF is the most intense source of synchrotron-generated light, producing X-rays 100 billion times brighter than the X-rays used in hospitals. The circumference of

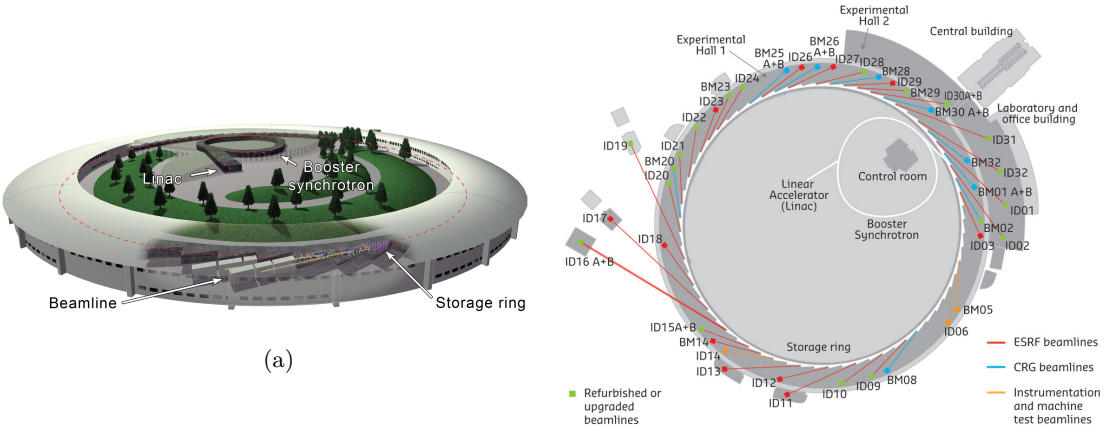

(a) (b)

Figure 1.14: The European Synchrotron Radiation Facility and the available beamlines (http://www.esrf.eu)

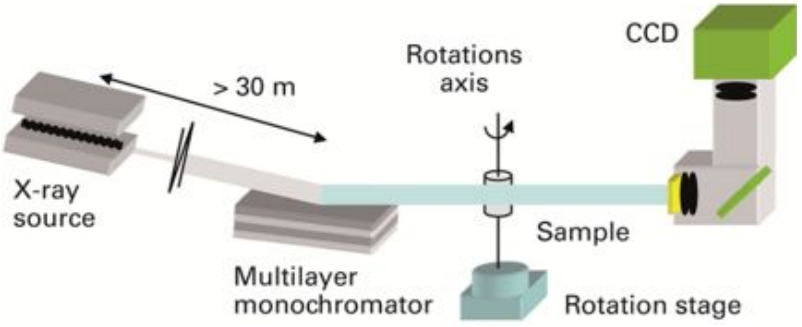

Figure 1.15: Experimental setup for computed tomography at ESRF beamline ID19 (http://www.esrf.eu).

the circular tunnel, the storage ring where the electrons are accelerated, has 844 meters. An example of a slice of the same sample imaged with the SR micro-CT and a Desktop micro-CT is presented in Figure 1.16.

A synchrotron source like the ESRF is a third generation source, also as APS (Chicago, USA) and Spring'8 (Himeji, Japan). Other third generation sources but with a lower critical energy are Sincrotrone Trieste (Trieste, Italy), SLS (Zürich, Switzerland), ALS (Berkeley, USA), SOLEIL (Orsay, France) [Peter and Peyrin (2011)].

Moreover, this technique makes it possible to quantify the local degree of mineralization in bones in three-dimensions simultaneously to the bone micro-architecture. The differences of the image's gray level intensity is associated to various stages of mineralization during bone remodeling process. This investigation method was proposed and compared to quantitative micro-radiography by [Nuzzo *et al.* (2002)b] and also applied to study the effect of etidronate in osteoporosis treatment [Nuzzo *et al.* (2002)a].

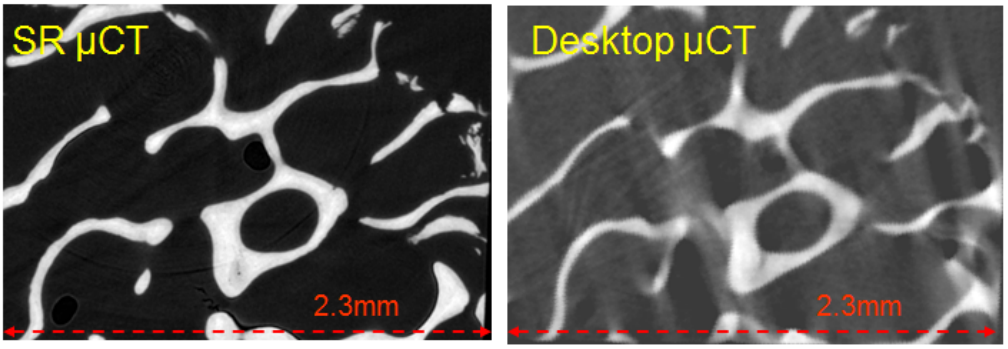

Figure 1.16: A comparison of a slice of the same biopsy sample using a SR micro-CT (left) and a Desktop micro-CT (right) [Nuzzo *et al.* (2002)b]

1.4.5 High Resolution peripheral Quantitative CT

Recent High Resolution peripheral Quantitative CT (HR-pQCT) devices can measure three-dimensional bone micro-architecture and volumetric bone mineral density (BMD) *in vivo* with previously unachievable accuracy and with relatively low-dose radiation [Cheung *et al.* (2013)]. Moreover, bone strength and fracture risk can be estimated non-invasively by applying computer-based finite element analysis (FEA) modeling to reconstructed images.

Commercialized by only a single manufacturer (XtremeCT; SCANCO Medical AG, Brüttisellen, Switzerland), HR-pQCT scanners are available in a limited number of pilot research sites in the world [Boutroy *et al.* (2005), Burghardt *et al.* (2013)]. Although this technique is not yet used in clinical diagnosis of bone related diseases, effects of different medical treatment [Seeman *et al.* (2010), Burghardt *et al.* (2010)b, Rizzoli *et al.* (2010), Macdonald *et al.* (2010)], age-related changes and gender differences of bone micro-architecture were better understood with the help of HR-pQCT [Boutroy *et al.* (2005), Khosla *et al.* (2006), Burghardt *et al.* (2010)a, Macdonald *et al.* (2011)].

This technique typically provides *in vivo* 3D images of the bone at peripheral sites (radius and tibia) with an isotropic voxel size of 82 μm. The effective radiation doze is around 3-5 μSv [Krug *et al.* (2010)]. For comparison, a chest X-ray exposes patients to a radiation dose of 0.1 mSv. The average annual limit dose internationally recommended not to be exceeded for planned radiation exposure is of 20 mSv/year, measured over a period of five years [Wrixon (2008)].
The standard protocol recommended by SCANCO Medical AG is considered in many publications [Boutroy *et al.* (2005), Khosla *et al.* (2006)]. In the acquisition process the patient's forearm or ankle is immobilized in a carbon fiber shell (Figure 1.17) fixed within the gantry of the scanner.

A scout view, essentially a two-dimensional x-ray scan, is acquired to define the tomographic scan region (Figure 1.18). Burghardt et al., mentioning the studies published in [Mueller *et al.* (2009)], remarks that the default radius axial scan partially includes the

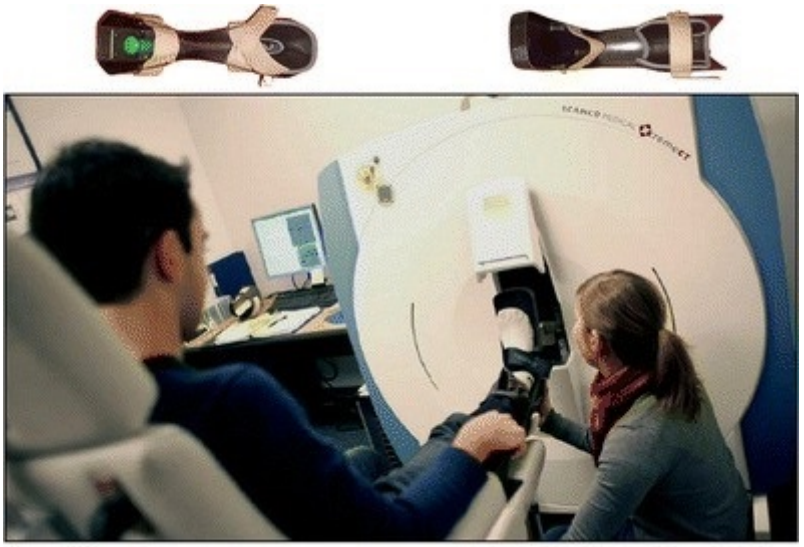

Figure 1.17: A typical setup of HR-pQCT for patient measurements. At top, the casts used for securing the forearm and lower leg is shown [Cheung *et al.* (2013)].

most common site, which is most strongly correlated to the experimental fracture of the forearm under a simulated falling load [Burghardt *et al.* (2011)].
The reconstructed images (3D volumes of 110 slices corresponding to a region of 9.02 mm in length) are then analyzed with the offered protocol. This includes the identification of the periosteal boundary and the individual segmentation of the cortical and trabecular bone tissue. Figure 1.19 shows typical HR-pQCT images of the radius and tibia bone. 3D reconstructions are also presented for the two identified bone tissues. Due to the fact that a global threshold is applied as segmentation method, for subjects with thin or highly porous cortical bone, incomplete and underestimated cortical structure can be extracted [Davis *et al.* (2007)]. Moreover, after binarization, quantitative parameters of trabecular bone architecture as the ones presented in section 1.4.6 can be computed. Nevertheless, by comparing this technique to micro-CT at higher spatial resolution, it was shown that some of these parameters were particularly sensitive to the segmentation [Krause *et al.* (2014)]. Thus, methods for improving the segmentation were investigated [Burghardt *et al.* (2007), Davis *et al.* (2007)].

As in the case of QCT or ex-vivo micro-CT, the attenuation values of HR-pQCT images can be converted to hydroxypatite mineral densities using a beam-hardening correction and a phantom calibration procedure. Volumetric BMD, that can offers a better evaluation of the micro-structure, is determined independently for cortical and trabecular bone.
For example, Figure 1.20 illustrates a case where two subjects with the same areal BMD value actually present substantial differences in the micro-structure of the trabecular bone and in the aspect of the cortical bone. The bone connectivity of the subject B is strongly deteriorated compared to that of the subject A. This analysis was possible with the help of the resolution that HR-pQCT system holds for in-vivo examination.

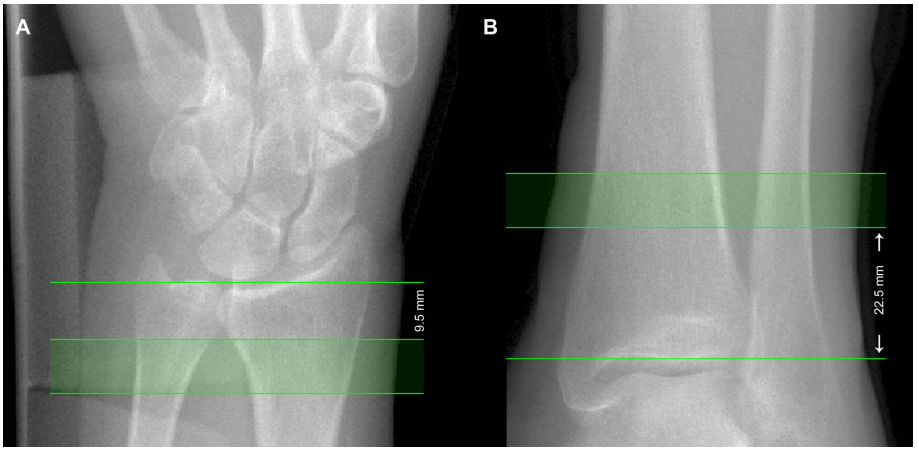

Figure 1.18: Scout acquisition used to define the HR-pQCT scan region for the distal radius (A) and distal tibia (B). The solid green region corresponds to the imaging location and consists of 110 slices spanning 9.02 mm longitudinally. In the radius the scan region is fixed 9.5 mm proximal from the mid-jointline, while in the tibia the scan region is 22.5 mm proximal from the tibial plafond [Krug *et al.* (2010)] .

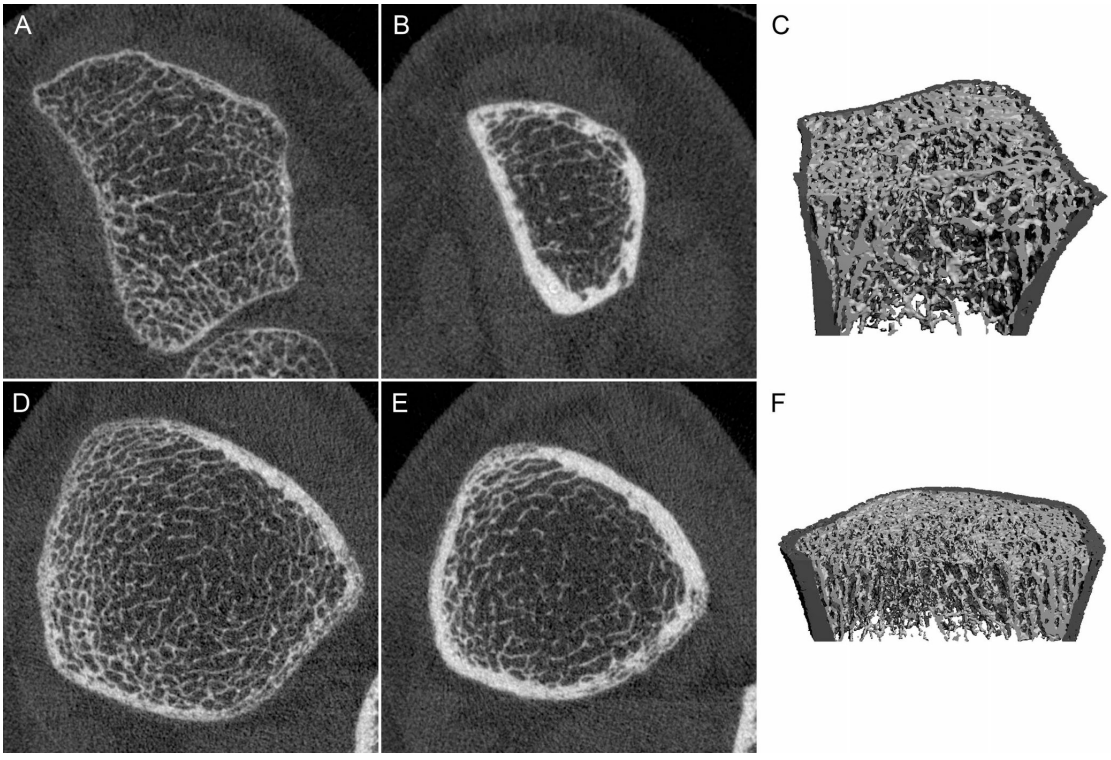

Figure 1.19: Typical HR-pQCT images from the distal radius (A-C) and distal tibia (D-F). Images A and D correspond to the distal most slices of the scan, while images B and E correspond to the proximal most slices. Images C and F are 3D reconstructions of the extracted mineralized structure with the segmented cortical compartment highlighted in dark gray [Krug *et al.* (2010)].

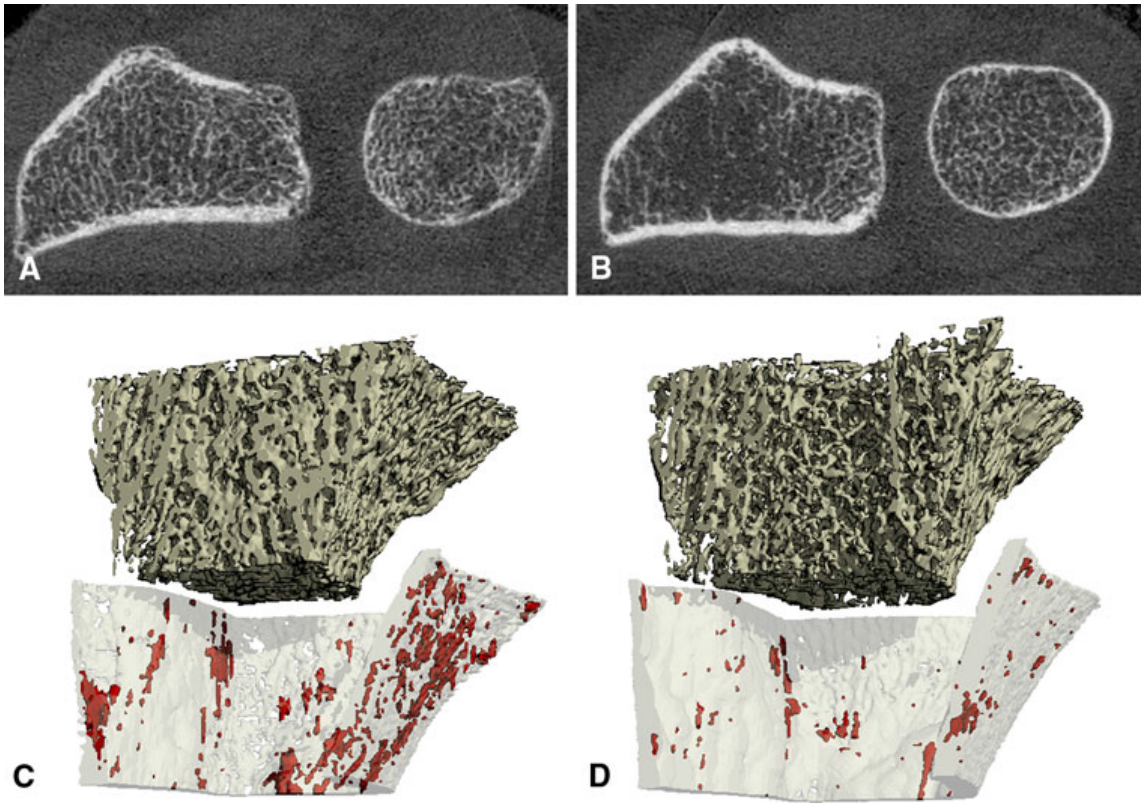

Figure 1.20: (A, B) Cross-sectional HR-pQCT images through the distal radius show two individuals with identical areal BMD by DXA at the ultradistal radius but substantial differences in trabecular and cortical structure. (C, D) Three-dimensional renderings of the cortical and trabecular bone compartments and intracortical porosity (highlighted in red) [Burghardt *et al.* (2011)].

Moreover, Figure 1.21 presents normal and pathological morphology of the trabecular micro-architecture.

From the limitations of this technique we recall the fact that common and important sites for osteoporotic fragility fractures, as lumber spine or proximal femur, cannot be scanned *in-vivo*. Furthermore, the acquisition method does not take into account the differences in bone length, that may be a source of variability in cross-sectional studies [Boyd (2008)]. An important aspect, related to the resolution of the system, was discussed in [Tjong *et al.* (2012)]. Even though the resolution of HR-pQCT scanners is an improvement for in-vivo investigation, compared to the correspondent micro-CT images (for bone samples), 82 μm can introduce a not negligible bias in the quantification of the bone subjects. A better resolution makes the segmentation step easier and in the end the trabecular micro-structure is correctly quantified and not overestimated as shown in Figure 1.22.

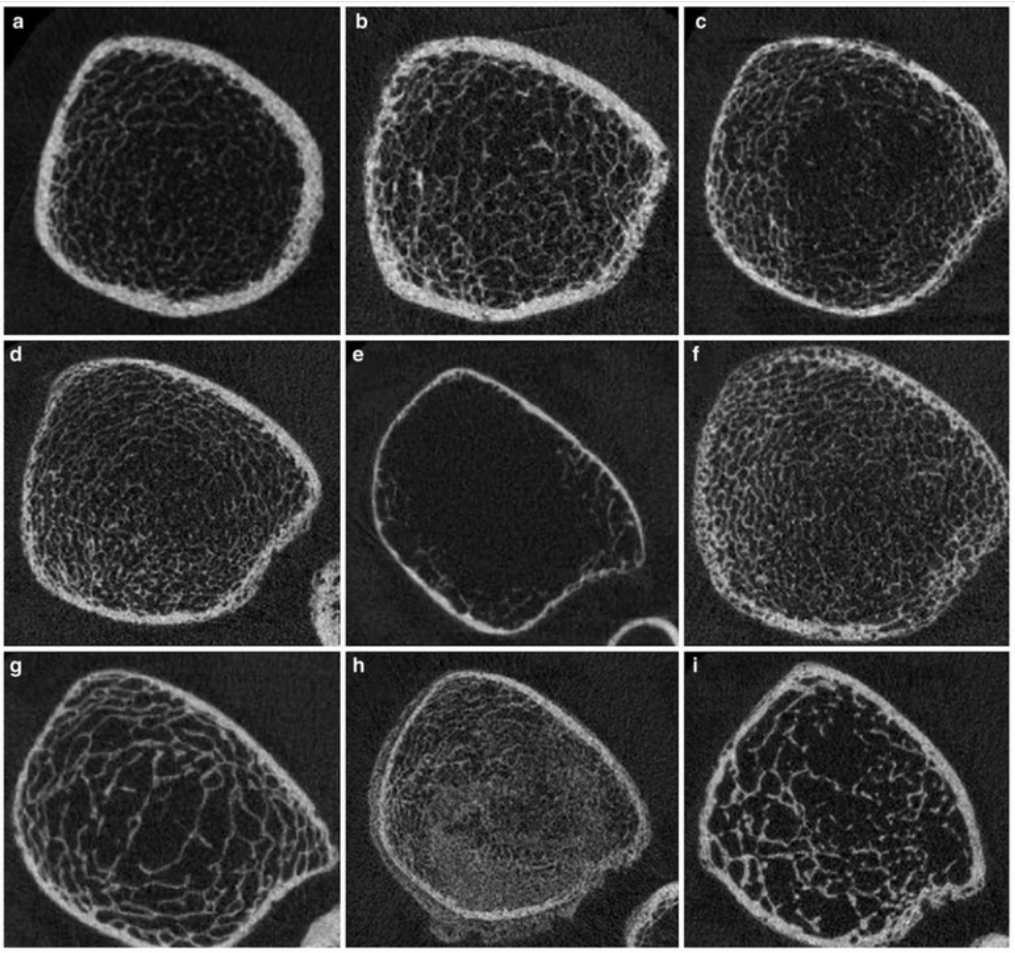

Figure 1.21: Normal morphology and pathologic examples of HR-pQCT images of ultradistal tibia. **a** Normal tibial bone microstructure in a middle-aged woman; **b-c** postmenopausal osteoporosis; **d** premenopausal osteoporosis; **e** young patient with post-traumatic paralysis of lower limbs; **f** postmenopausal woman with type-2 diabetes mellitus and fractures; **g** renal osteodystrophy; **h** healing insufficiency fracture; **i** osteogenesis imperfecta (Sillence type I) [Patsch and Bauer (2013)]

1.4.6 3D bone parameters

The same parameters presented in the section 1.3 can be extended for 3D CT bone images (see Figure 1.23 for a schematic illustration).

Other parameters considered are the Euler number (χ) [Ohser *et al.* (2011)] and the density of connectivity (Conn.D in mm^{-3}) that normalize the connectivity (β_1) by the total volume and:

$$\beta_1 = \beta_0 + \beta_2 - \chi \tag{1.2}$$

where β_0, β_2 are the number of the connected components and the number of cavities [Odgaard (1997)].

In Figure 1.24 we present the standard quantitative HR-pQCT parameters that are

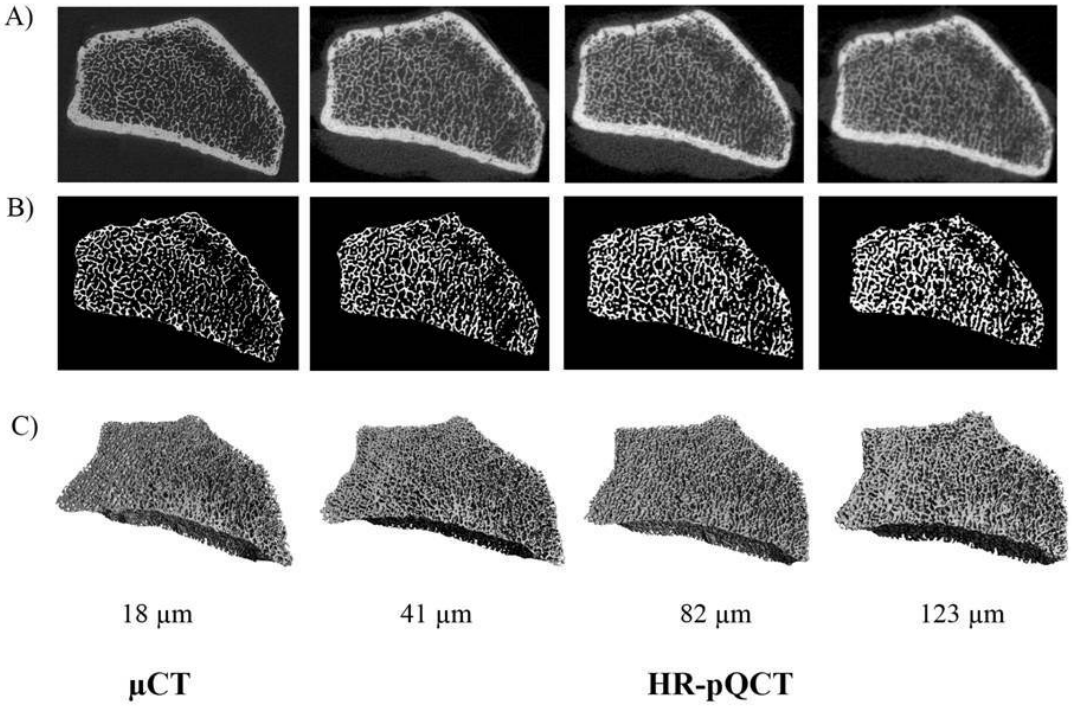

Figure 1.22: Representative images of the trabecular segmentation for both μCT and HR-pQCT images. (A) Grayscale images acquired by the respective scanners. (B) Trabecular segmentation of a single slice. (C) 3D representation of the trabecular volume [Tjong *et al.* (2012)]

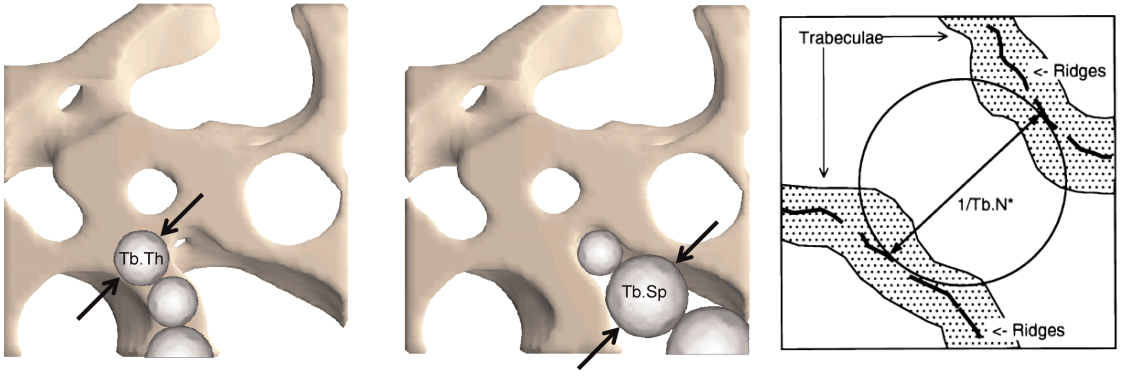

(a) (b) (c)

Figure 1.23: Schematic representation of algorithm used for direct 3D calculation of (a) trabecular thickness, (b) trabecular separation and (c) trabecular number [Bouxsein *et al.* (2010), Laib and Rüegsegger (1999)]

measured also for micro-CT images.

The structural model index (SMI), based on surface convexity, estimates the degree of the trabecular structure of rode-like or plate-like elements [Hildebrand and Rüegsegger (1997)]. Rods are elongated and cylindrical regions, whereas plates are extensive, flatter regions. SMI can take values between 0 and 4, 0 for a flat plane, 3 for cylindrical rods

	Abbreviation	Description	Standard unit
Metric measures			
Total volume	TV	Volume of entire region of interest	mm^3
Bone volume	BV	Volume of region segmented as bone	mm^3
Bone surface	BS	Surface area of the region segmented as bone	mm^2
Bone volume ratio*	BV/TV	Ratio of bone volume to total volume in region of interest	%
Bone surface ratio	BS/BV	Ratio of bone surface area to bone volume	%
Trabecular thickness*	Tb.Th	Mean thickness of trabeculae	mm
Trabecular thickness SD	Tb.Th.SD	Measure of homogeneity of trabecular thickness	mm
Trabecular separation*	Tb.Sp	Mean space between trabeculae	mm
Trabecular separation SD	Tb.Sp.SD	Measure of homogeneity of trabecular spacing	mm
Trabecular number*	Tb.N	Mean number of trabeculae per unit length	per mm
Cortical thickness (original)*	Ct.Th	Average cortical thickness	mm
Cortical porosity	Ct.Po	Cortical porosity	%
Bone mineral density (D100)*	BMD	Total volumetric density	mg HA/cm^3
Cortical bone mineral density (Dcomp)*	Ct.BMD	Cortical volumetric density	mg HA/cm^3
Trabecular bone mineral density (Dtrab)*	Tb.BMD	Trabecular volumetric density	mg HA/cm^3
Total bone area*	Tt.Ar	Cross-sectional area	mm^2
Non-Metric Measures			
Structural model Index	SMI	Measure of trabecular structure (0 for plates and 3 for rods	
Degree of anisotropy	DA	1 is isotropic, >1 is anisotropic by definition; DA = length of longest divided by shortest mean intercept length vector	
Connectivity density	Conn.D	Extent of trabecular connectivity normalized by TV	mm^{-3}
Cross-sectional moment of inertia	Imin, Imax	minimum and maximum moments of inertia	mm^4

*Standard HR-pQCT measures are indicated

Figure 1.24: HR-pQCT parameters with units [Cheung *et al.* (2013)]

and 4 for spheres. The algorithm which determines the SMI is based on covering all the surface of the trabecular bone with triangles. After that, the surface area of the bone's structure before and after an infinitesimal dilation is compared to its volume.

Furthermore, algorithms to determine rod-like and plate-like elements for independently quantification are presented in [Bonnassie *et al.* (2003), Stauber and Müller (2006), Liu *et al.* (2008), Peyrin *et al.* (2010)]. An example of local topological analysis for distal radius trabecular bone is presented in Figure 1.25.

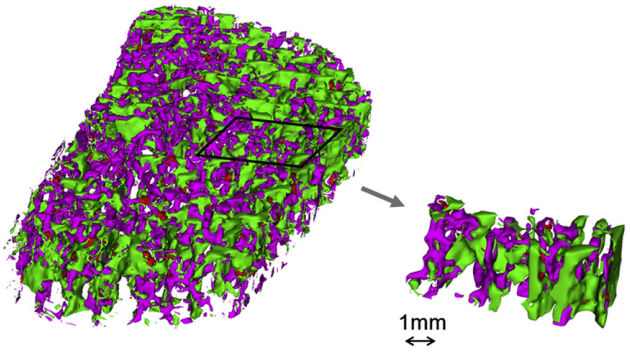

Figure 1.25: Local topological analysis (LTA) of a distal radius trabecular bone (in purple: pixels of rod-like trabeculae; in green: pixels of plate-like trabeculae) [Pialat *et al.* (2012)].

On the other hand, cortical bone parameters are analyzed, such as cortical thinning, cortical porosity [Bousson *et al.* (2004)], and more recently studied, the cortical ultrastructure (merging of Haversian canals, clustering of osteons and the distribution of osteosyte lacunae).

Chapter 2

Background

This chapter will shortly present the main theoretical background necessary to illustrate the problems encountered in the micro-CT and HR-pQCT bone image analysis and the proposed approaches to enhance the quantification of the trabecular bone microarchitecture.

2.1 Linear inverse problems in image restoration

Having a linear operator A defined as $A : X \to Y$ we say that we solve a **direct problem** if for a given element $f \in X$ we find $g \in Y$

$$g = Af, \tag{2.1}$$

Sometimes, we know the output $g \in Y$ and the operator A and we want to determine the input f. In this case we say that we solve the **inverse problem**. The theory was originally developed for Hilbert spaces like L_2 or Sobolev spaces. It was extended to Banach spaces useful for the TV regularization [Scherzer *et al.* (2008)].

The inverse problem defined above is said to be **well-posed on the pair of spaces** (X,Y) [Hadamard (1902)] if the following three conditions are satisfied:

1. There exists a solution for all $g \in Y$
2. The solution is unique
3. The solution depends continuously on the output g.

This implies that the operator A has to be bijective and A^{-1} has to be continuous. A solution can then be computed directly (provided that A^{-1} can be computed):

$$f = A^{-1}g, \tag{2.2}$$

When the problem does not satisfy these conditions it is said to be **ill-posed**.

Linear inverse problems are encountered in many engineering applications and they play a major role in image processing. For example, image deconvolution and restoration problems are crucial in medical imaging or image and video coding. Such problems can be formulated as:

$$g^{\delta} = Af + w, \tag{2.3}$$

where g^{δ} represents the measured data, f the ideal image, w an additive noise corrupting the measurements with the noise level δ and A a linear transform like blurring by a given kernel or the composition of a smoothing operation and of an under-sampling operator. These problems are ill-posed and small changes in the data can have big effects on the solutions.
The solution of this type of problem is not necessarily unique. In the following, if it is unique, the solution of $Af = g$ will be denoted f^* and corresponds to the ground-truth.

2.2 Regularization methods

In this thesis, we try to inverse the ill-posed deconvolution or super-resolution problem with variational regularization approaches. The Baysian framework represents another way to formalize and solve the same types of ill-posed problems [Molina (1994), Ruiz *et al.* (2015)], that will not be described herein, but it is related to our variational approach.
A well-known way to solve an ill-posed inverse problem as (2.3) is by adding prior information and then constructing a regularization functional such as:

$$J(f) = \frac{\mu}{2}\left\|Af - g^{\delta}\right\|^2 + R(f) \tag{2.4}$$

The functional $J(f)$ is composed of two terms. The first term is the data term, data fidelity term or also called misfit term and measures the distance between the estimate and the measurements. The second term imposes an a priori on the derived solution and is called the regularization term. μ is the regularization parameter and its value has a high influence on the image result, balancing the contribution of the two terms [Scherzer *et al.* (2008)].

By minimizing (2.4):

$$f(\mu) \in \arg\min_{f} J(f). \tag{2.5}$$

we obtain the desired solution, the restored image obtained after applying the regularization method for a given parameter μ.

A good regularization method must be well-defined, stable and convergent [Scherzer *et al.* (2008)].
A regularization method is said to be convergent if $f(\mu) \to f^*$, when $\delta \to 0$ for a proper choice of $\mu \to 0$.
A regularization method is called stable if for a fixed μ, $f(\mu)$ depends continuously on g^δ.

The regularization methods differ through the regularization term included in the functional to be minimized. We detail next some of the most used regularization terms and some more recent ones.

2.2.1 Regularization term

Tikhonov and Sobolev regularization

The Tikhonov regularization [Tikhonov and Arsenin (1977)] involves the L_2 norm of the image. The Sobolev regularization is based on the squared L_2 norm of the gradient of the image and is given by:

$$R_{Sobolev}(f) = \int_\Omega \underbrace{\left(\frac{\partial f(\boldsymbol{r})}{\partial x}\right)^2 + \left(\frac{\partial f(\boldsymbol{r})}{\partial y}\right)^2}_{||\nabla f(\boldsymbol{r})||_2^2} dr. \tag{2.6}$$

where $\boldsymbol{r}(x, y)$ represents the pixel location and $\Omega \subset \mathbb{R}^2$.
The prior information assumed in this case is the uniform smoothness of the image.

Total Variation regularization

The Total Variation regularization was introduced in [Rudin *et al.* (1992)] to solve the noise removal problem. After that, the TV regularization was applied to problems like image reconstruction [Combettes and Pesquet (2004), Bioucas-Dias *et al.* (2006), Beck and Teboulle (2009)], inpainting [Chan and Shen (2002)] and zooming [Chambolle (2004)]. This regularization is based on summing the L_2 norm of the spatial gradient of the image:

$$R_{TV}(f) = \int_\Omega \underbrace{\sqrt{\left(\frac{\partial f(\boldsymbol{r})}{\partial x}\right)^2 + \left(\frac{\partial f(\boldsymbol{r})}{\partial y}\right)^2}}_{\|\nabla f(\boldsymbol{r})\|_2} d\boldsymbol{r}. \tag{2.7}$$

In fact, this regularization is defined for the space of bounded variation functions and it is only a semi-norm, as the Total Variation of a constant function is 0. This functional is convex but not differentiable. It is therefore difficult to minimize the regularization

functional. One approach is to smooth the functional, replacing $\|u\|$ by $\sqrt{\epsilon^2 + \|u\|^2}$ to obtain a differentiable penalty and then use the gradient descent method (or any smooth optimization method).

$$R_{TV,\epsilon}(f) = \int_\Omega \sqrt{\epsilon^2 + \|\nabla f(\boldsymbol{r})\|^2} dr. \tag{2.8}$$

Figure 2.1 presents the smoothing of the absolute value (red curve) in 1D for two different ϵ values. The blue curve is the absolute value of the $[-5, 5]$ interval.

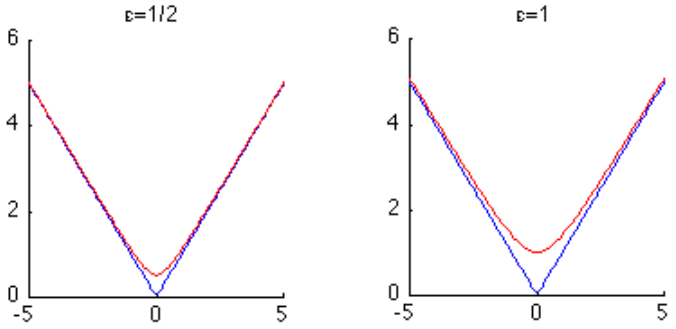

Figure 2.1: Smoothing of the absolute value in 1D

TV regularization is widely used in many applications due to its convexity, invariance to image shifts and rotations and also for the ability to preserve edges. However, the TV regularization results present patchy or cartoon-like staircase artifacts. Different approaches were proposed in order to overcome these problems. Farsiu et al. introduced in 2004 an improved TV regularization considering the bilateral TV in the case of multi frame super-resolution [Farsiu *et al.* (2004)]. Also, in [Peyré *et al.* (2011)] a non-local TV regularization is applied for inverse problems like super-resolution, inpainting, compressive sensing. More recent studies of this regularization method involve higher order derivative to attenuate the staircase effect as in [Hu and Jacob (2012), Lefkimmiatis *et al.* (2012)a, Lefkimmiatis *et al.* (2012)b, Chan *et al.* (2000), Lysaker and Tai (2006), Yuan *et al.* (2009), Chambolle and Lions (1997), Chan *et al.* (2007), You and Kaveh (2000), Lysaker *et al.* (2003), Steidl (2005)].

Higher Degree Total Variation regularization

A reinterpretation of the classical TV regularization based on mixed $L_1 - L_2$ or $L_1 - L_1$ norms of the image's directional derivatives is presented in [Hu and Jacob (2012)]. It is the basis for a generalization to higher order TV regularization that will minimize the staircase artifacts.

Rotation steerability of directional derivatives

Considering the unit vector $u_0 = (cos(\theta), sin(\theta))$ as in Figure 2.2

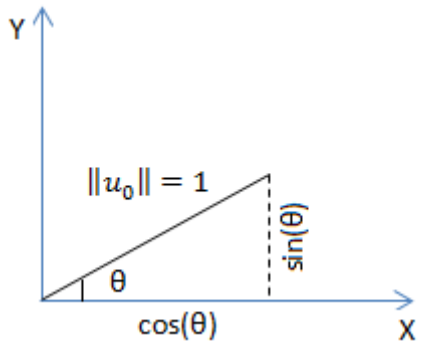

Figure 2.2: Unit vector in 2D

the first degree directional derivative of a function f along u_0 is given by:

$$\mathrm{D}_\theta^{(1)} f(\boldsymbol{r}) = \frac{\partial}{\partial \gamma} f(\boldsymbol{r} + \gamma u_\theta). \tag{2.9}$$

As mentioned in [Hu and Jacob (2012)], the directional derivatives of continuously differentiable functions are rotation steerable [Peyré *et al.* (2011), Chan *et al.* (2000)], in the sense that the derivative along any direction is a linear combination of the derivative in the x and y directions. To express the derivative along any direction we can use the formula:

$$\mathrm{D}_\theta^{(1)} f(\boldsymbol{r}) = \underbrace{[cos(\theta), sin(\theta)]}_{s_1^T(\theta)} \underbrace{\begin{bmatrix} \partial f(\boldsymbol{r})/\partial x \\ \partial f(\boldsymbol{r})/\partial y \end{bmatrix}}_{h_1(\boldsymbol{r})}. \tag{2.10}$$

where s^T denotes the transpose of the vector s.
The second degree directional derivative of the function f can be expressed by using the equation (2.10) for $\mathrm{D}_\theta^{(1)} f(\boldsymbol{r})$:

$$\begin{aligned} \mathrm{D}_\theta^{(2)} f(\boldsymbol{r}) &= \underbrace{[cos(\theta), sin(\theta)]}_{s_1^T(\theta)} \begin{bmatrix} \partial \mathrm{D}_\theta^{(1)} f(\boldsymbol{r})/\partial x \\ \partial \mathrm{D}_\theta^{(1)} f(\boldsymbol{r})/\partial y \end{bmatrix} \\ &= \underbrace{[cos^2(\theta), 2cos(\theta)sin(\theta), sin^2(\theta)]}_{s_2^T(\theta)} \underbrace{\begin{bmatrix} \partial^2 f(\boldsymbol{r})/\partial x^2 \\ \partial^2 f(\boldsymbol{r})/\partial x \partial y \\ \partial^2 f(\boldsymbol{r})/\partial y^2 \end{bmatrix}}_{h_2(\boldsymbol{r})}. \end{aligned} \tag{2.11}$$

More generally, the n^{th} degree directional derivative is rotation steerable and it can be

written as:

$$\mathrm{D}_\theta^{(n)} f(\boldsymbol{r}) = s_n^T(\theta) h_n(\boldsymbol{r}) \tag{2.12}$$

where $s_n(\theta)$ is a vector of trigonometric polynomials and $h_n(\boldsymbol{r})$ the vector of partial derivatives of f of order n.

Isotropic HDTV Regularization

The L_1 norm of the gradient magnitude of f can be interpreted as the mixed $L_1 - L_2$ norm of directional derivative of f as shown below:

$$\frac{1}{\sqrt{2}} \int_\Omega \|\nabla f(\boldsymbol{r})\|_2 \, d\boldsymbol{r} = \int_\Omega \underbrace{\sqrt{\frac{1}{2\pi} \int_0^{2\pi} \left| \mathrm{D}_\theta^{(1)} f(\boldsymbol{r}) \right|^2 d\theta}}_{\left\| \mathrm{D}_\theta^{(1)} f(\boldsymbol{r}) \right\|_{L_2[0,2\pi]}} d\boldsymbol{r}. \tag{2.13}$$

It combines the L_1 norm for the position and the L_2 norm for the angles.

The proof of this equivalence is presented in [Hu and Jacob (2012)] and is based on the steerability property of the directional derivatives:

$$\begin{aligned}
\left\| \mathrm{D}_\theta^{(1)} f(\boldsymbol{r}) \right\|_{L_2[0,2\pi]}^2 &= \frac{1}{2\pi} \int_0^{2\pi} \left| s_1^T(\theta) h_1(\boldsymbol{r}) \right|^2 d\theta \\
&= h_1^T(\boldsymbol{r}) \left(\frac{1}{2\pi} \int_0^{2\pi} s_1(\theta) s_1^T(\theta) d\theta \right) h_1(\boldsymbol{r}) \\
&= h_1^T(\boldsymbol{r}) \underbrace{\left(\frac{1}{2\pi} \int_0^{2\pi} \begin{bmatrix} cos^2(\theta) & sin(2\theta)/2 \\ sin(2\theta)/2 & sin^2(\theta) \end{bmatrix} d\theta \right)}_{\frac{1}{2} I} h_1(\boldsymbol{r}) \\
&= \frac{1}{2} h_1^T(\boldsymbol{r}) h_1(\boldsymbol{r}) = |\nabla f(\boldsymbol{r})|^2 / 2.
\end{aligned} \tag{2.14}$$

The isotropic n^{th} degree TV penalty is defined as:

$$R_{IHDTV}^{(n)}(f) = \int_\Omega \left\| \mathrm{D}_\theta^{(n)} f(\boldsymbol{r}) \right\|_{L_2[0,2\pi]} d\boldsymbol{r} \tag{2.15}$$

Y. Hu and M. Jacob called this penalty (2.15) isotropic HDTV.

This penalty is invariant to rotations and translations and is also convex since it is obtained by summing the square magnitude of the function's directional derivatives along all directions and orientations. Due to the L_1 norm that preserves the directional derivatives in regions with high directional energy given by $\left\| \mathrm{D}_\theta^{(n)} f(\boldsymbol{r}) \right\|_{L_2[0,2\pi]}$, this penalty preserves the image features and is expected to avoid staircasing effects [Hu and Jacob (2012)].

By applying the steerability property of the directional derivatives we obtain:

$$\begin{aligned}\left\|\mathrm{D}_{\theta}^{(n)} f(\boldsymbol{r})\right\|_{L_2} &= \sqrt{\frac{1}{2\pi}\int_0^{2\pi}\left|\mathrm{D}_{\theta}^{(n)} f(\boldsymbol{r})\right|^2 d\theta} \\ &= \sqrt{h_n^T(\boldsymbol{r})\left(\frac{1}{2\pi}\int_0^{2\pi} s_n(\theta)s_n^T(\theta)\,d\theta\right)h_n(\boldsymbol{r})}.\end{aligned} \tag{2.16}$$

We will use the notation C_n as in [Hu and Jacob (2012)] for the symmetric matrix between brackets, with the elements $c_{i,j} = \frac{1}{2\pi}\int_0^{2\pi} s_i(\theta)s_j(\theta)d\theta$. The Isotropic HDTV regularizer becomes:

$$R_{IHDTV}^{(n)}(f) = \int_{\Omega}\sqrt{h_n^T(\boldsymbol{r})C_n h_n(\boldsymbol{r})}\,d\boldsymbol{r}. \tag{2.17}$$

In the case when n=2, the second-degree Isotropic Total Variation regularization we denote it simply R_{IHDTV} and is given by:

$$C_2 = \frac{1}{2\pi}\int_0^{2\pi} s_2(\theta)s_2^T(\theta)\,d\theta = \frac{1}{8}\begin{bmatrix}3 & 0 & 1\\ 0 & 4 & 0\\ 1 & 0 & 3\end{bmatrix} \tag{2.18}$$

where
$s_2(\theta) = \left[cos^2(\theta), sin(2\theta), sin^2(\theta)\right]^T$ and $h_2(\boldsymbol{r}) = \left[\frac{\partial^2 f(\boldsymbol{r})}{\partial x^2}, \frac{\partial^2 f(\boldsymbol{r})}{\partial x \partial y}, \frac{\partial^2 f(\boldsymbol{r})}{\partial y^2}\right]^T$.

This first reinterpretation of the classical TV regularizer, the $L_1 - L_2$ mixed norms presented above, will encourage the joint sparsity of the directional derivatives, resulting in isotropic smoothing of the image.

2.3 Super-resolution

The super-resolution (SR) problem consists in obtaining one or a set of high-resolution (HR) images from one or a set of low-resolution (LR) images [Farsiu *et al.* (2004)]. Thus, super-resolution problems can be classified into the following categories: single-input single-output (SISO) super-resolution, multi-input single-output (MISO) super-resolution, which is the classical super-resolution and multi-input multi-output (MIMO) super-resolution [Mohammad-Djafari (2008)].

In the last three decades, a variety of super-resolution methods have been proposed. These super-resolution methods can be divided into two main classes: frequency domain methods and spatial domain methods.

The first paper published regarding super-resolution was [R. Y. Tsai (1984)] and considered the MISO case. They applied this technique for terrestrial photographs taken by Landsat satellites. Their model involved aliasing and translation of a constant scene. The solution proposed in [R. Y. Tsai (1984)] was a frequency domain method based on the

shift property of the Fourier transform. This first approach did not consider the optical blur or a specific noise. After that, in [Tekalp *et al.* (1992)] is formulated this problem by including the point spread function of the imaging system and noise.

Nowadays, many of the publications on super-resolution are applying spatial domain methods due to the high flexibility in the choice of motion model, motion blur and optical blur, and the sampling process. Another important factor is that the constraints are much easier to formulate (e.q. Markov random fields).

In this thesis, we focus on variational approaches. Yet, to solve the super-resolution problem we may consider probabilistic methods [Schultz and Stevenson (1996)] [Tom and Katsaggelos (1994)] [Mohammad-Djafari (2008)] [Mohamad-Djafari (2013)] and optimization methods like projection onto convex sets (POCS) [Stark and Oskoui (1989)] [Patti *et al.* (1994)].

Many super-resolution methods were applied in medical and biological imaging [Lehmann *et al.* (1999)] [Schatzberg and Devaney (1992)] or aerial and satellite imaging [Shekarforoush *et al.* (1996)] but also to embedded low resolution imaging devices, such as mobile phones [Aguiar and Moura (2001)].

This thesis focuses on the single image super-resolution case. The mathematical model is expressed by the same equation (2.3) but where g^δ represents the low resolution image, f is the high resolution image we would like to obtain, A is a linear, non-invertible, blurring and down-sampling operator, and w is an additive Gaussian white noise. Thus, having the intensity measurements denoted by g^δ, a low resolution blurred and noisy image, we aim to obtain the corresponding high resolution image, f.

Figure 2.3: Effects of reducing spatial resolution. A 1024x1024, 8-bit image down-sampled to size 32x32 pixels [Gonzalez and Woods (2002)].

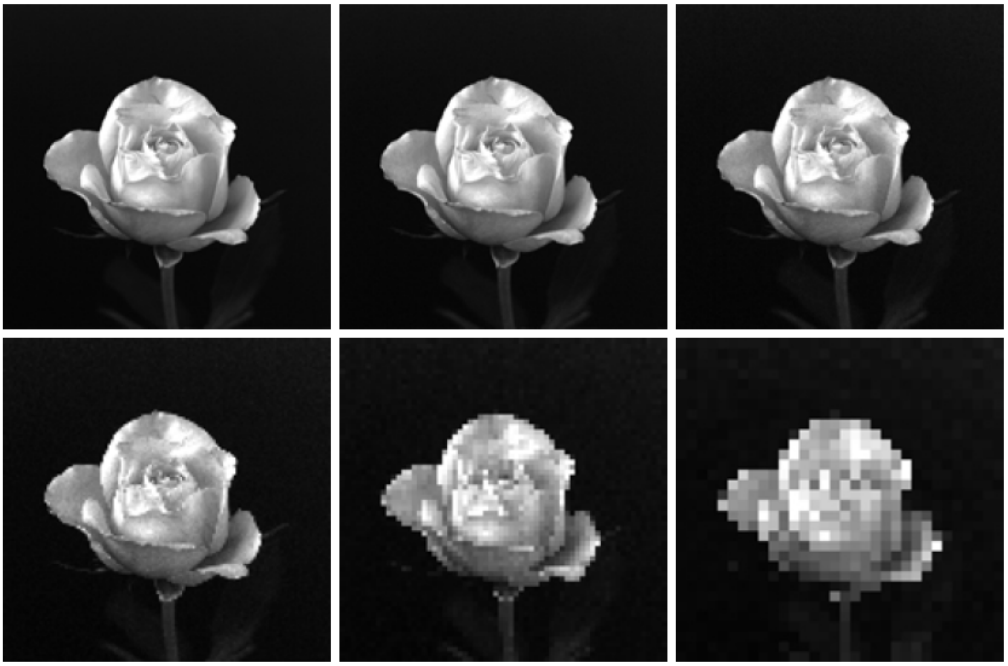

Figure 2.4: (a) 1024x1024, 8-bit image. (b) 512x512 image resampled into 1024x1024 pixels by row and column duplication. (c) through (f) 256x256, 128x128, 64x64, and 32x32 images resampled into 1024x1024 pixels [Gonzalez and Woods (2002)].

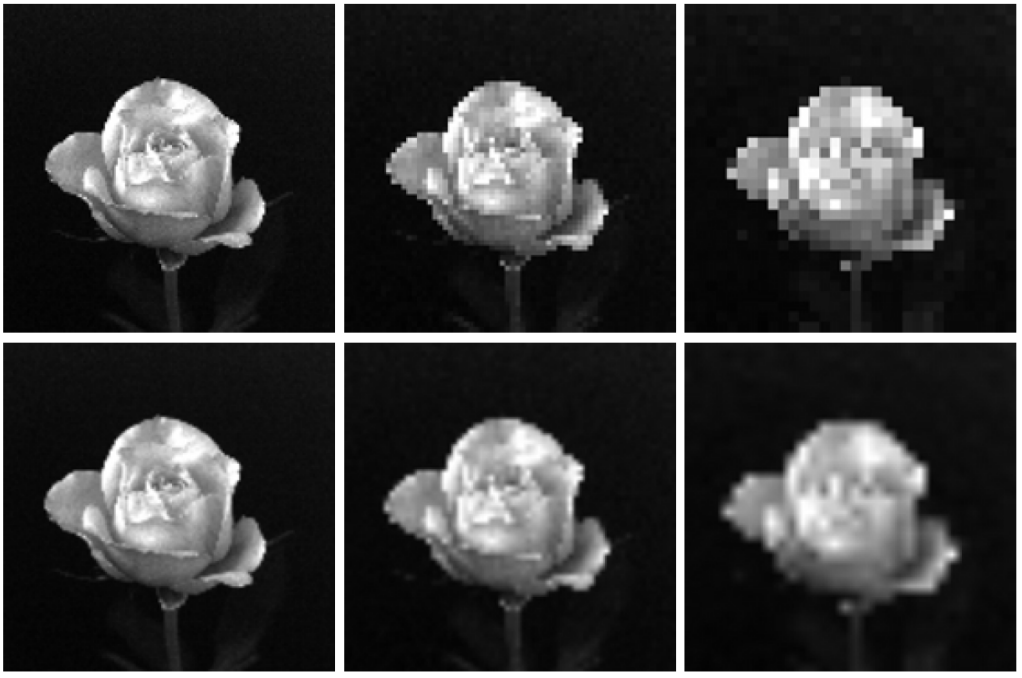

Figure 2.5: Top row: images zoomed from 128x128, 64x64, and 32x32 pixels to 1024x1024 pixels, using nearest neighbor gray-level interpolation. Bottom row: same sequence, but using bilinear interpolation [Gonzalez and Woods (2002)].

2.4 Blind deconvolution and super-resolution

In blind deconvolution and super-resolution problems, the unknown image must be recovered and at the same time the blurring kernel must be estimated. A review of variational bayesian blind image deconvolution is presented in [Ruiz *et al.* (2015)].

In the framework of variational methods, the following functional considered can be written for blind deconvolution

$$J(A, f) = \|k * f - g^\delta\|^2 + \alpha_1 \|f - \overline{f}\|^2 + \alpha_2 \|k - \overline{k}\|^2 \tag{2.19}$$

where α_1 and α_2 are regularization parameters, k is the kernel, f the unknown image and g^δ the data, and $\overline{k}$, and $\overline{f}$ are first guess estimates.

Starting from this double regularization method, some approaches use an alternating minimization scheme with respect to f and k [You and Kaveh (1996), Chan and Wong (1998)].

It will be the approach followed in this work. Some convergence results can be found in for Sobolev regularization, but the result depends on $\overline{k}$ and $\overline{f}$ [Chan and Wong (2000)]. The conditions under which a minimum norm solution exists and is unique have been investigated in the work of [Justen and Ramlau (2006)]. A non-iterative numerical scheme is also proposed by the authors. Similar alternating approaches based on alternating minimization with proximal operators are presented in [Abboud *et al.* (2014)].

Most existing variational approaches to blind deconvolution are single-level since the image and the PSF appear in a single objective function that has to be minimized. More elaborate methods with bilevel optimization for finding the PSF are presented in [Hintermüller and Wu (2015)]. In the lower level, the total variation model is imposed. In the upper level, an objective functional is considered, which incorporates the statistical information on the image and the PSF.

2.5 Optimization methods

Different optimization methods are used in this thesis. Recently, the proximal methods based on proximal operators have been much developed. These methods are used for sums of convex lower semi-continuous functions [Combettes and Pesquet (2007), Combettes and Pesquet (2008)].

These methods have not been considered in this manuscript. The basic conjugate gradient method is often used in this work, and the minimization of the regularization functional is performed with the Alternate Direction Method of Multipliers (ADMM).

2.5.1 Conjugate gradient

The conjugate gradient method was developed by Magnus Hestenes and Eduard Stiefel in 1952 [Hestenes and Stiefel (1952)] and it is a widely used algorithm for solving a linear

system as:

$$Ax = b \tag{2.20}$$

where A is a symmetric positive-definite matrix. It is an iterative method so it can be applied to sparse systems that are too large to be solved by direct methods such as the Cholesky decomposition. The conjugate gradient (CG) is a very effective method since at each iteration only a small number of vectors are necessary for the next update and have to be kept in memory. The name of the method derives from the fact that a sequence of conjugate (or orthogonal) vectors is generated. These vectors are the residuals of the iterates that can be interpreted also as the gradients of a quadratic functional, the minimization of which is equivalent to solving the linear system.

Starting with an initial guess of $x^{(0)}$, at step i the iterate $x^{(i)}$ is updated by a multiple (α_i) of the search direction vector $p^{(i)}$:

$$x^{(i)} = x^{(i-1)} + \alpha_i p^{(i)}. \tag{2.21}$$

The corresponding residual $r^{(i)} = b - Ax^{(i)}$ is updated as:

$$r^{(i)} = r^{(i-1)} - \alpha_i q^{(i)} \text{ where } q^{(i)} = Ap^{(i)} \tag{2.22}$$

where $\alpha_i = {r^{(i-1)}}^T r^{(i-1)} / {p^{(i)}}^T A p^{(i)}$.

The search direction is updated using the residual:

$$p^{(i)} = r^{(i)} - \beta_{i-1} p^{(i-1)} \tag{2.23}$$

where the choice $\beta_i = {r^{(i)}}^T r^{(i)} / {r^{(i-1)}}^T r^{(i-1)}$ ensures that $p^{(i)}$ and $Ap^{(i-1)}$ - or equivalently, $r^{(i)}$ and $r^{(i-1)}$ - are orthogonal [Barrett *et al.* (1994)].

To speed up the CG method we can use a preconditioner M, symmetric and positive definite, that can approximate A and is easier to invert it. The linear system $Ax = b$ will be indirectly determined by solving:

$$M^{-1}Ax = M^{-1}b. \tag{2.24}$$

The aim of using a preconditioner is to improve the condition number of a matrix that measures the sensitivity of a linear system's solution to errors in the data. Moreover, this number gives an indication of the results' accuracy from the matrix inversion and the linear equation solution. A condition number close to 1 indicates a well-conditioned matrix.

Figure 2.6 is presenting the pseudocode of the Preconditioned Conjugate Gradient Method when a preconditioner M is used. In the case when the preconditioner $M = I$ we obtain the unpreconditioned version of the algorithm. In the pseudocode the instruction

solve (line 3) has to be removed and z replaced by r (line 4, 6 and 9).

Geometric interpretation of the CG method and of other related methods can be found

Compute $r^{(0)} = b - Ax^{(0)}$ for some initial guess $x^{(0)}$
for $i = 1, 2, \ldots$
  solve $Mz^{(i-1)} = r^{(i-1)}$
  $\rho_{i-1} = r^{(i-1)^T} z^{(i-1)}$
  if $i = 1$
    $p^{(1)} = z^{(0)}$
  else
    $\beta_{i-1} = \rho_{i-1}/\rho_{i-2}$
    $p^{(i)} = z^{(i-1)} + \beta_{i-1} p^{(i-1)}$
  endif
  $q^{(i)} = Ap^{(i)}$
  $\alpha_i = \rho_{i-1}/p^{(i)^T} q^{(i)}$
  $x^{(i)} = x^{(i-1)} + \alpha_i p^{(i)}$
  $r^{(i)} = r^{(i-1)} - \alpha_i q^{(i)}$
  check convergence; continue if necessary
end

Figure 2.6: The pseudocode for the Preconditioned Conjugate Gradient Method [Barrett *et al.* (1994)]

in [Shewchuk (1994), Křížek and Korotov (2004)] and are presented in Figure 2.7.

(a) quadratic form

(b) Conjugate gradient

Figure 2.7: Geometrical interpretation of the conjugate gradient method [Křížek and Korotov (2004)]

As we have seen in Figure 2.7 (a) the linear problem (2.24) is equivalent to the mini-

mization of the quadratic form:

$$J(x) = \frac{1}{2}x^T Ax - b^T x + c \tag{2.25}$$

The optimality condition $gradJ = 0$ can be rewritten as $Ax - b = 0$ thus $Ax = b$ for positive-define A. We recall in Figure 2.8 the graphical representation of a quadratic form for a positive or negative-define matrix. In the case of a singular and positive-indefinite matrix, we will have a set of solutions given by a line that runs through the bottom of the valley. For an indefinite matrix, methods like CG can't be applied.

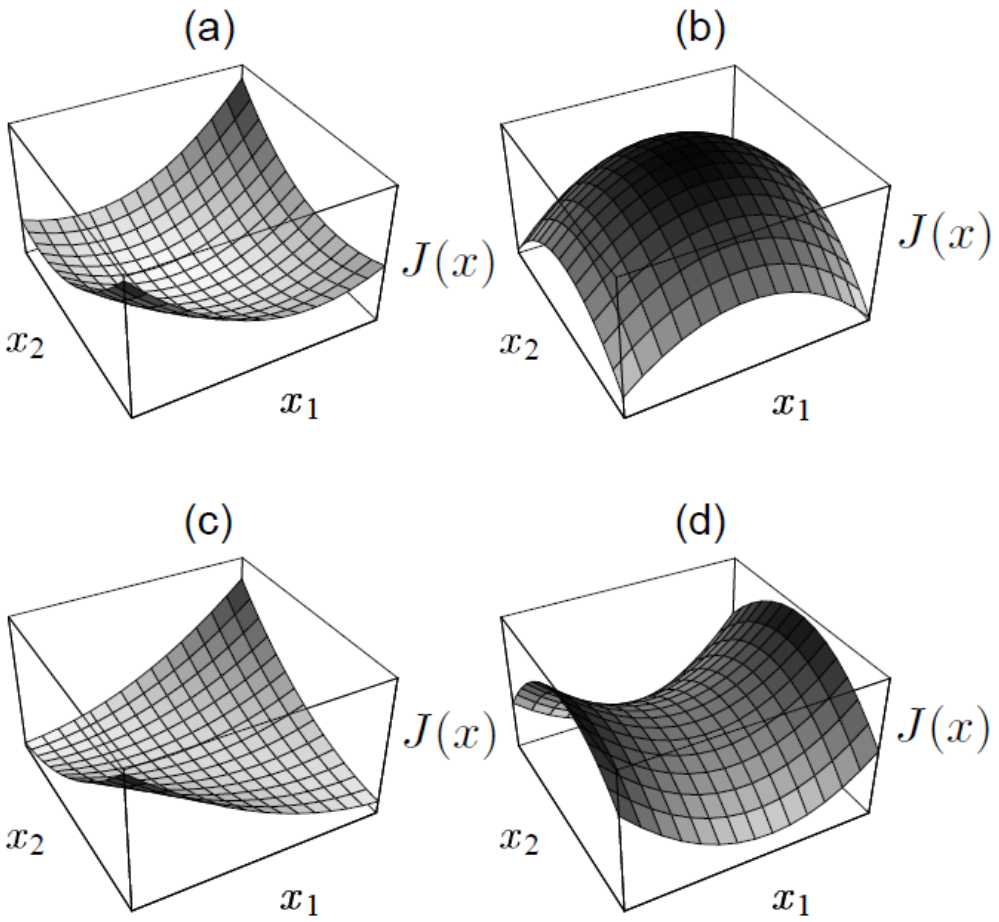

Figure 2.8: Graphical representation of: (a) Quadratic form for a positive-definite matrix. (b) For a negative-definite matrix. (c) For a singular and positive-indefinite matrix. (d) For an indefinite matrix [Shewchuk (1994)].

2.5.2 Majorization-Minimization Algorithm

Having a non-differentiable penalty, one approach to solve an optimization problem is to apply a majorization-minimization (MM) algorithm. This type of algorithm proposes first to find a new quadratic functional $J^{(m)}(f)$ that depends on the current iterate $f^{(m)}$ and majorizes the original functional $J(f)$:

$$J(f) \leq J^{(m)}(f), \forall f; \; J^{(m)}(f^{(m)}) = J(f^{(m)}). \tag{2.26}$$

After that, the penalty to minimize will become the quadratic one, thus, a simpler functional for a minimization algorithm as conjugate gradient:

$$f^{(m+1)} = arg\,\min_{f} J^{(m)}(f). \tag{2.27}$$

A frequent used MM algorithm is the Iterated Reweighted Least Square (IRLS) algorithm.

2.5.3 Alternating Direction Method of Multipliers

The minimization of the regularization functional is performed with the Alternate Direction of Minimization method [Boyd *et al.* (2011), Esser (2009)].

The principle of the method is to construct an augmented Lagrangian with dual variable which takes into account the constraints on the function to reconstruct, and to use splitting techniques. The minimization is performed iteratively on the splitting and dual functions. This method is linked with the proximal methods. Its convergence properties have also been studied [Boyd *et al.* (2011)].

2.6 Segmentation

There is an enormous amount of work concerning the segmentation problem. Some review can be found for example in [Aubert and Kornprobst (2002)]. The segmentation step subdivides an image into its constituent parts or objects.

Some approaches in the literature use the geodesic active contour and level-set formalism. Others are based on the Mumford-Shah functional, with two unknowns: the intensity function and the edges. One of the difficulty of this method is to approximate the regularization functional. The latter involves the Hausdorff measure of the set of edges which extends the notion of length to nonsmooth sets.

Some work have shown that the Mumford Shah functional can be used for the regularization of linear inverse ill-posed problems [Ramlau and Ring (2010), Jiang *et al.* (2014)].

These publications are very interesting for us because in most cases, the deconvolution or super-resolution problem are considered separately from the segmentation problem.

Recently, some researchers have studied these inverse problems with the Potts regularization which is a special case of the Mumford Shah functional [Storath *et al.* (2014), Wein-

mann *et al.* (2015)]. This work uses the L_0 norm of the gradient of the image f, $\|\nabla f\|_0$. This regularization term is non-convex and the minimization of the regularization functional sets convergence and implementation problems.

2.7 Metrics of image quality

Considering the type of images involved in the restoration process, different metrics were developed to measure the image quality improvement. We recall below some of the most frequently used metrics. For the next subsections the reference image is denoted as f^* and the restored image as f. The total number of the image pixels is denoted with n.

2.7.1 Mean Squared Error (MSE)

The mean squared error (MSE) is based on the difference pixel by pixel (error) between two images, the reference image and the restored one. The computation of MSE is given by the expression:

$$MSE = \frac{1}{n}\sum_{i=1}^{n}(f_i^* - f_i)^2 \tag{2.28}$$

By this metric a smaller value of MSE is associated to a better restored image.

2.7.2 Peak Signal-to-Noise Ratio (PSNR)

The Peak Signal-to-Noise Ratio (PSNR) is another metric used to measure the image quality based on MSE and the dynamic of the reference image given by the difference between the maximum and the minimum value of the image:

$$PSNR = 10\log_{10}\frac{(\max(f^*) - \min(f^*))^2}{MSE} \tag{2.29}$$

This metric is measured in decibels and a better restored image will have a higher PSNR value.

2.7.3 Dice Similarity Coefficient

The DICE similarity coefficient (DSC) first proposed by [Dice (1945)], is based on the accuracy of the overlapping of two binary images (i.e. segmented images), denoted herein A and B:

$$DICE = 2\frac{A \cap B}{A + B} \tag{2.30}$$

A DICE value of 1 will represent a perfect overlap and a value of 0, no overlap. In the case of partial overlap, the DICE coefficient has the drawback of not accounting the way the images are overlapping and this must be interpreted by visual evaluation of the structures.

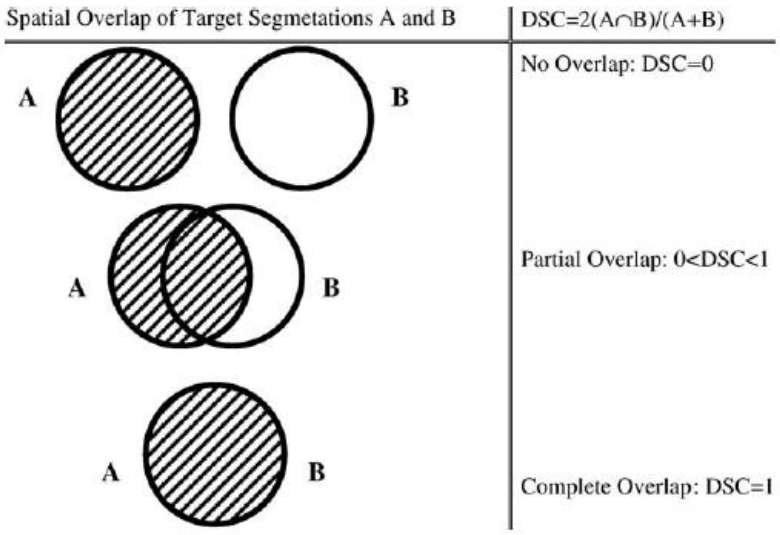

Figure 2.9: The Dice similarity coefficient representing spatial overlap and reproducibility [Zou *et al.* (2004)].

Chapter 3

Total Variation based Super-Resolution

3.1 Introduction

The analysis of trabecular bone micro-structure has an important role in the investigation and diagnosis of bone loss diseases. Recent studies (see Figure 1.22) showed that the analysis of *in-vivo* HR-pQCT images of trabecular bone is biased by the lack of resolution of the images [Tjong *et al.* (2012)]. Quantitative bone parameters as BVTV and the bone connectivity are influenced by the quality of the bone micro-structure segmentation. In order to overcome this drawback of the HR-pQCT bone images we started our research by super-resolution based image restoration techniques.

Super-resolution is an active field of research [Chaudhuri (2002), Park *et al.* (2003)]. Traditionally, super-resolution requires several low-resolution images. As our aim is to improve the resolution of *in-vivo* images we will consider the inverse problem set with a single input image. Since the images we are interested in display quasi binary structures, we can strongly rely on a total variation (TV) prior model, thus improving the resolution from a single image.

The restoration of an image with an improved resolution from a single low-resolution image requires a model of the degradation the image undergoes during the acquisition process. Starting from a high-resolution image $\boldsymbol{f}$, the low-resolution image $\boldsymbol{g}^\delta$ can be modeled as resulting from a blurring followed by a down-sampling, with some added random fluctuations to account for different sources of noise:

$$\boldsymbol{g}^\delta = \boldsymbol{A}\boldsymbol{f} + \boldsymbol{w}, \tag{3.1}$$

where $\boldsymbol{g}^\delta \in \mathbb{R}^N$ denotes the N-pixels low-resolution image measured by the imaging system, $\boldsymbol{f} \in \mathbb{R}^{N'}$ denotes an $N' = N \times p^d$-pixels high-resolution image with super-resolution factor p in each of the d dimensions of the image, $\boldsymbol{A}$ is the linear operator accounting for blurring followed by down-sampling, and $\boldsymbol{w}$ is the (random) noise component.

Recovering a higher-resolution image $\boldsymbol{f}$ from the low-resolution image $\boldsymbol{g}^\delta$ amounts to solving a linear inverse problem. We consider maximum *a posteriori* restoration methods that estimate the high-resolution image $\boldsymbol{f}$ as the minimizer of a function of the form:

$$\boldsymbol{f}(\mu) = \arg\min_{\boldsymbol{f}} \frac{\mu}{2} \left\| \boldsymbol{A}\boldsymbol{f} - \boldsymbol{g}^\delta \right\|_2^2 + \mathcal{R}(\boldsymbol{f}) \,, \tag{3.2}$$

where the first term of the sum corresponds to the negative of the log-likelihood under a white Gaussian noise hypothesis, $\mathcal{R}(\cdot)$ is a regularization term (i.e., prior term) and μ is related to the noise variance and balances the relative weight of each of the two terms.

In the following work, we make the assumption that the blur operator is a shift invariant Gaussian taking into account the properties and the simplicity of this kernel. Although the model of the blur of the reconstructed CT images is not exactly the one proposed, we may find in the literature that it represents a good first estimation [Chen and Ning (2004)].

We have presented in section 2.2.1 some of the possible regularization methods applied until now to solve image reconstruction or restoration problems. We choose from these ones the classical TV approach and the recently generalized Isotropic High Degree Total Variation. In papers like [Lefkimmiatis *et al.* (2012)a, Hu and Jacob (2012)] the HDTV regularization functional is minimized with majorization-minimization algorithms. Various numerical methods have been used to solve the TV regularized deconvolution problem [Becker *et al.* (2011), van den Berg and Friedlander (2008)]. Yet, extensive numerical experiments show that algorithms based on the Alternating Direction Method of Multipliers (ADMM) are the state-of-the-art methods [Yang *et al.* (2009), Afonso *et al.* (2010), Ng *et al.* (2010)].

In this chapter, we extend the ADMM minimization method to isotropic HDTV regularization. We introduce a general formulation of the regularization term suited to both methods, TV and isotropic HDTV. A specific preconditioned conjugate gradient is proposed to circumvent the shift-variant effects produced by sub-sampling and up-sampling operations.The validation of the proposed approaches is performed from 2D experimental high-resolution micro-CT images of bone samples at 20 μm after simulating the effect of blur, loss of spatial resolution and noise.

The method and the results presented in this chapter have been published in the following article:
A. Toma , B. Sixou , L. Denis, J.B. Pialat, F. Peyrin, "Higher order Total Variation super-resolution from a single trabecular bone image", ISBI 2014, Beijing, China, April 2014, pp 1152-1155

3.2 Total Variation Super-resolution

When a discrete image $\boldsymbol{f}$ is considered, the isotropic Total Variation method presented in section 2.2.1 can be rewritten under the form:

$$\mathcal{R}_{\mathrm{TV}}(\boldsymbol{f}) = \sum_i \|\boldsymbol{D}_i \boldsymbol{f}\|\,, \tag{3.3}$$

where the sum is carried over all pixels of $\boldsymbol{f}$ and $\boldsymbol{D}_i$ is the discrete gradient operator at pixel i. For 2D case and the i^{th} pixel at the location (x, y), the first order finite difference operator $\boldsymbol{D}_i$ is defined by $\boldsymbol{D}_i : \mathbb{R}^{N'} \to \mathbb{R}^2$, $\boldsymbol{D}_i \boldsymbol{f} = (\boldsymbol{D}_i^x \boldsymbol{f}, \boldsymbol{D}_i^y \boldsymbol{f})$. If we consider the image $\boldsymbol{f}$ to have different sizes in the two dimensions, $N' = N'_x N'_y$, the horizontal and vertical difference operators are given by:

$$\boldsymbol{D}_i^x \boldsymbol{f} = \begin{cases} \boldsymbol{f}_{x+1,y} - \boldsymbol{f}_{x,y} & x < N'_x \\ 0 & x = N'_x \end{cases} \tag{3.4}$$

$$\boldsymbol{D}_i^y \boldsymbol{f} = \begin{cases} \boldsymbol{f}_{x,y+1} - \boldsymbol{f}_{x,y} & y < N'_y \\ 0 & y = N'_y \end{cases} \tag{3.5}$$

One drawback of TV is that it favors piecewise constant regions with disk-like shapes. It is therefore not very well adapted to restore thin structures [Lefkimmiatis *et al.* (2012)a].

3.3 Higher Degree Total Variation Super-resolution

The isotropic higher degree total variation (IHDTV) of order 2 can be written in a continuous framework as:

$$\mathcal{R}_{\mathrm{IHDTV}}(f) = \int \|\mathrm{D}_\theta^{(2)} f(\boldsymbol{r})\|_{\mathrm{L}_2[0,2\pi]}\, \mathrm{d}\boldsymbol{r}\,, \tag{3.6}$$

with $\mathrm{D}_\theta^{(2)}$ the directional derivative of order 2 in direction θ. This directional derivative can be expressed in 2D as a function of horizontal and vertical derivatives:

$$\mathrm{D}_\theta^{(2)} f(x,y) = \begin{bmatrix} \cos^2\theta & 2\cos\theta\sin\theta & \sin^2\theta \end{bmatrix} \begin{bmatrix} f_{xx} \\ f_{xy} \\ f_{yy} \end{bmatrix}, \tag{3.7}$$

with $f_{xx} \equiv \partial^2 f(x,y)/\partial x^2$, $f_{xy} \equiv \partial^2 f(x,y)/\partial x \partial y$ and $f_{yy} \equiv \partial^2 f(x,y)/\partial y^2$. The regularization term $\mathcal{R}_{\mathrm{IHDTV}}$ defined in equation (3.6) involves an isotropic L_2 norm corresponding to the integrated square magnitude of the directional derivative over all orientations:

$$\|\mathrm{D}_\theta^{(2)} f(\boldsymbol{r})\|^2_{\mathrm{L}_2[0,2\pi]} = \frac{1}{2\pi} \int_0^{2\pi} \left(\mathrm{D}_\theta^{(2)} f(\boldsymbol{r})\right)^2 \mathrm{d}\theta \,. \tag{3.8}$$

By integrating equation (3.7) over θ and applying a Cholesky factorization to the obtained matrix C_2 (2.18), the isotropic L_2 norm can be re-written under a simpler form, given here in the 2D case:

$$\left\|\mathrm{D}_\theta^{(2)} f(x,y)\right\|_{\mathrm{L}_2[0,2\pi]} = \left\| \begin{bmatrix} \frac{\sqrt{6}}{4} & 0 & \frac{1}{2\sqrt{6}} \\ 0 & \frac{1}{\sqrt{2}} & 0 \\ 0 & 0 & \frac{1}{\sqrt{3}} \end{bmatrix} \begin{bmatrix} f_{xx} \\ f_{xy} \\ f_{yy} \end{bmatrix} \right\|. \tag{3.9}$$

In a discrete setting, this regularization functional can be written under a form very similar to standard total variation:

$$\mathcal{R}_{\mathrm{IHDTV}}(\boldsymbol{f}) = \sum_i \|\boldsymbol{B}_i \boldsymbol{f}\| \tag{3.10}$$

where matrix $\boldsymbol{B}_i$ stands for a linear operator both performing discrete second order derivatives at pixel i and applying the linear transform given in equation (3.9).

3.4 Minimization algorithm

Restoration of a high-resolution image $\boldsymbol{f}(\mu)$ from a single low-resolution image requires solving an optimization problem of the form of equation (3.2). By introducing auxiliary variables $\boldsymbol{h}_i = (\boldsymbol{h}_i^1, \boldsymbol{h}_i^2) \in \mathbb{R}^2$, the minimization problem can be re-expressed as a constrained $\ell_2 + \ell_1$ minimization problem:

$$\begin{aligned} \boldsymbol{f}(\mu) = \underset{\boldsymbol{f},\,\{\boldsymbol{h}_i\}}{\arg\min} \; & \frac{\mu}{2} \left\|\boldsymbol{A}\boldsymbol{f} - \boldsymbol{g}^\delta\right\|_2^2 + \sum_i \|\boldsymbol{h}_i\| \,, \\ \text{s.t.} \quad & \boldsymbol{h}_i = \boldsymbol{P}_i \, \boldsymbol{f}, \;\; \forall i, \end{aligned} \tag{3.11}$$

where matrices $\boldsymbol{P}_i$ correspond either to the discrete gradient $\boldsymbol{D}_i$ at pixel i in the case of $\mathcal{R}_{\mathrm{TV}}$, or to $\boldsymbol{B}_i$ when second order $\mathcal{R}_{\mathrm{IHDTV}}$ is considered.

The optimization problem (3.11) can be solved efficiently by finding the saddle point of the augmented Lagrangian using the alternating direction method of multipliers (ADMM) [Yang *et al.* (2009), Afonso *et al.* (2010), Ng *et al.* (2010)]. The augmented Lagrangian associated to constrained problem (3.11) writes:

$$\mathcal{L}_{\mathrm{A}}(\boldsymbol{f}, \{\boldsymbol{h}_i\}, \{\boldsymbol{\lambda}_i\}) = \frac{\mu}{2} \left\| \boldsymbol{A}\boldsymbol{f} - \boldsymbol{g}^{\delta} \right\|_2^2 + \sum_i \|\boldsymbol{h}_i\| + \sum_i \left[\frac{\beta}{2} \|\boldsymbol{h}_i - \boldsymbol{P}_i\, \boldsymbol{f}\|^2 - \boldsymbol{\lambda}_i^{\mathrm{t}} (\boldsymbol{h}_i - \boldsymbol{P}_i\, \boldsymbol{f}) \right] , \tag{3.12}$$

with $\boldsymbol{\lambda}_i \in \mathbb{R}^2$ the Lagrange multipliers for the i^{th} equality constraint and β the Lagrangian parameter.

To find the saddle point of the augmented Lagrangian, the ADMM method alternates between three updates:

$$\begin{aligned} \boldsymbol{f}^{k+1} &= \arg\min_{\boldsymbol{f}} \mathcal{L}_{\mathrm{A}}(\boldsymbol{f}, \boldsymbol{h}_i^k, \boldsymbol{\lambda}_i^k) \\ \boldsymbol{h}_i^{k+1} &= \arg\min_{\boldsymbol{h}} \mathcal{L}_{\mathrm{A}}(\boldsymbol{f}^{k+1}, \boldsymbol{h}, \boldsymbol{\lambda}_i^k) \\ \boldsymbol{\lambda}_i^{k+1} &= \boldsymbol{\lambda}_i^k - \beta(\boldsymbol{h}_i^{k+1} - \boldsymbol{P}_i \boldsymbol{f}^{k+1}) \end{aligned} \tag{3.13}$$

Thus the ADMM iterates become:

1. Update of the high-resolution reconstruction $\boldsymbol{f}$, by (approximately) solving the linear system:
$$\boldsymbol{H}\boldsymbol{f}^{k+1} = \mu \boldsymbol{A}^{\mathrm{t}} \boldsymbol{g}^{\delta} + \sum_i \boldsymbol{P}_i^{\mathrm{t}} (\beta \boldsymbol{h}_i^k - \boldsymbol{\lambda}_i^k) ,$$
with $\boldsymbol{H} = \mu \boldsymbol{A}^{\mathrm{t}}\boldsymbol{A} + \sum_i \beta \boldsymbol{P}_i^{\mathrm{t}} \boldsymbol{P}_i$.

2. Update of the auxiliary variables $\boldsymbol{h}_i$, by applying a soft-thresholding operator $\mathcal{S}_\beta$:
$$\boldsymbol{h}_i^{k+1} = \mathcal{S}_\beta \left(\boldsymbol{P}_i \boldsymbol{f}^{k+1} + \boldsymbol{\lambda}_i^k / \beta \right) ,$$
with $\mathcal{S}_\beta(\boldsymbol{u}) = \max\left(1 - \frac{1}{\beta\|\boldsymbol{u}\|}, 0\right) \cdot \boldsymbol{u}$.

3. Update of the Lagrange multipliers $\boldsymbol{\lambda}_i$:
$$\boldsymbol{\lambda}_i^{k+1} = \boldsymbol{\lambda}_i^k - \beta \left(\boldsymbol{h}_i^{k+1} - \boldsymbol{P}_i \boldsymbol{f}^{k+1} \right) .$$

More details about how the updates were obtained can be found in the Appendix C.

The convergence of the ADMM algorithm is summarized by the following theorem [Ng *et al.* (2010), Wang *et al.* (2008), Frick *et al.* (2011)]:

Theorem 3.4.1. *The sequence* $(\boldsymbol{f}^k, \{\boldsymbol{h}_i^k\}, \{\boldsymbol{\lambda}_i^k\})$ *generated by the ADMM algorithm converges to a Kuhn-Tucker point* $(\boldsymbol{f}(\mu), \{\boldsymbol{h}_i^*\}, \{\boldsymbol{\lambda}_i^*\})$ *of the problem, which corresponds to a saddle point of the Lagrangian. With the augmented Lagrangian given in (3.12), the*

Karush-Kuhn-Tucker (KKT) conditions can be written as:

$$\mu \boldsymbol{A}^t(\boldsymbol{A}\boldsymbol{f}(\mu) - \boldsymbol{g}^\delta) = -\sum \boldsymbol{P}_i^t(\boldsymbol{\lambda}_i^*), \quad \boldsymbol{\lambda}_i^* \in \partial\|\boldsymbol{P}_i\boldsymbol{f}(\mu)\|_2, \quad \boldsymbol{h}_i^* = \boldsymbol{P}_i\boldsymbol{f}(\mu) \tag{3.14}$$

In our super-resolution problem, the hessian $\boldsymbol{H}$ that has to be inverted in the first update step is not shift invariant, thus it can not be diagonalized by Discrete Fourier Transform (DFT). In order to speed up the calculation, a diagonal preconditioner is used in the Fourier domain. Let $\boldsymbol{S}$ be the sub-sampling matrix, and $\boldsymbol{W}_0 = \boldsymbol{S}^{\mathrm{t}}\boldsymbol{S}$. The hessian matrix can be decomposed into:

$$\boldsymbol{H} = \sum_{s=0}^{p^d-1} \boldsymbol{H}_s\boldsymbol{W}_s\,, \tag{3.15}$$

where $\boldsymbol{H}_s$ are circulant matrices and $\boldsymbol{W}_s$ shifted versions of $\boldsymbol{W}_0$. The chosen preconditioner $\boldsymbol{M}$ is the closest to matrices $\boldsymbol{H}_s$ as measured by Frobenius norm:

$$\boldsymbol{M} = \arg\min_{\boldsymbol{X}} \sum_{s=0}^{p^d-1} \|\boldsymbol{X} - \boldsymbol{H}_s\|_F^2\,. \tag{3.16}$$

Since $\boldsymbol{M}$ and $\boldsymbol{H}_s$ are circulant, equation (3.16) can be diagonalized in Fourier domain:

$$\tilde{m}_k = \frac{1}{p^d}\sum_{s=0}^{p^d-1} \tilde{h}_{s,k}\,. \tag{3.17}$$

The Fourier transform $\tilde{m}_k$ at frequency k of the impulse response of shift-invariant operator $\boldsymbol{M}$ thus corresponds to the average of transfer functions $\tilde{h}_{s,k}$. The inverse of the preconditioner is then readily obtained by element-wise inversion in Fourier domain.

3.5 Numerical experiments

In order to compare the performance of the two regularization schemes, the methods were tested on CT bone images artificially deteriorated. Also, a comparison with up-sampling by bicubic interpolation is presented.

Considering the high quality of the parallel-beam synchrotron micro-CT images (see Figure 1.16) we have chosen four slices (Figure 3.1) from different human bone samples, cylinder core of 10 mm, at a voxel size of 10 μm. First, the bone volumes were reconstructed from 1500 2D projections using the Filtered back projection algorithm [Salomé *et al.* (1999)] and further resampled at 20 μm. Each Region of Interest, that is a 2D gray level image in the range of (0, 255), was artificially deteriorated by a Gaussian blur denoted $\boldsymbol{G}$, a sub-sampling operator, $\boldsymbol{S}$, and an additive Gaussian noise. The process of obtaining the low resolution image is presented in Figure 3.2.

Figure 3.3 illustrates on image 4 (Figure 3.1(d)) the deterioration process step by step, considering a Gaussian point spread function of standard deviation $\sigma_{blur} = 4.85$

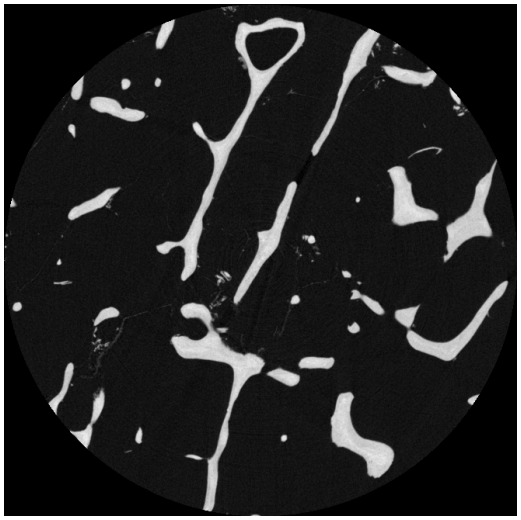

(b) image 1 (tb317)

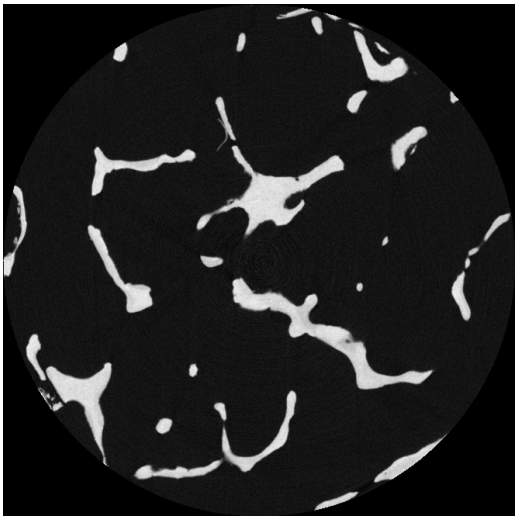

(c) image 2 (tb331)

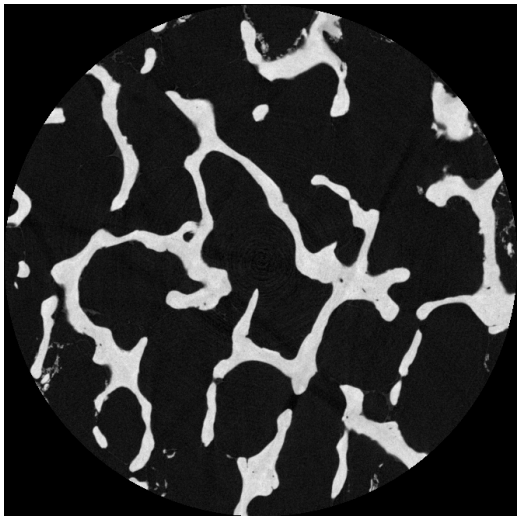

(d) image 3 (tb332)

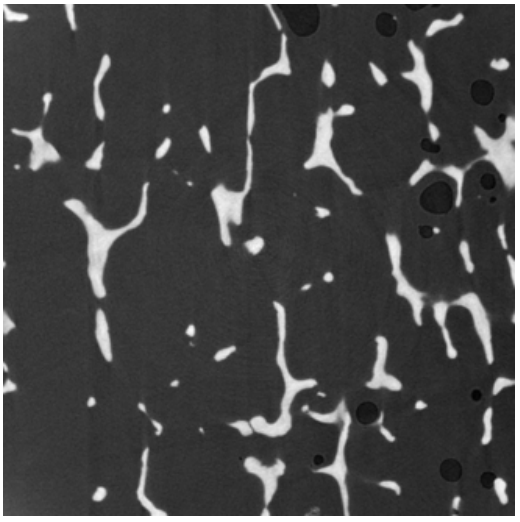

(a) image 4 (calca47b)

Figure 3.1: Synchrotron micro-CT test images

(corresponding to the estimated blur from real images), a sub-sampling rate of $p = 4$ and a Gaussian noise with a standard deviation $\sigma = 1$.

The same steps were applied to all test images. The ADMM iterations were stopped when

$$\frac{\|f^{k-1} - f^k\|_2}{\|f^k\|_2} < \epsilon \tag{3.18}$$

were the value of ϵ was chosen to ensure the convergence of the methods. The image quality obtained was measured with the Peak Signal-to-Noise Ratio (PSNR) defined as in (2.29). Since our final goal is to quantify bone micro-architecture after the segmentation of bone from background, we introduce additional parameters computed after segmentation. The image is segmented by applying the Otsu threshold. Then, we calculate the DICE coefficient defined as in (2.30), the bone surface (in mm^2), and the Euler number (χ)

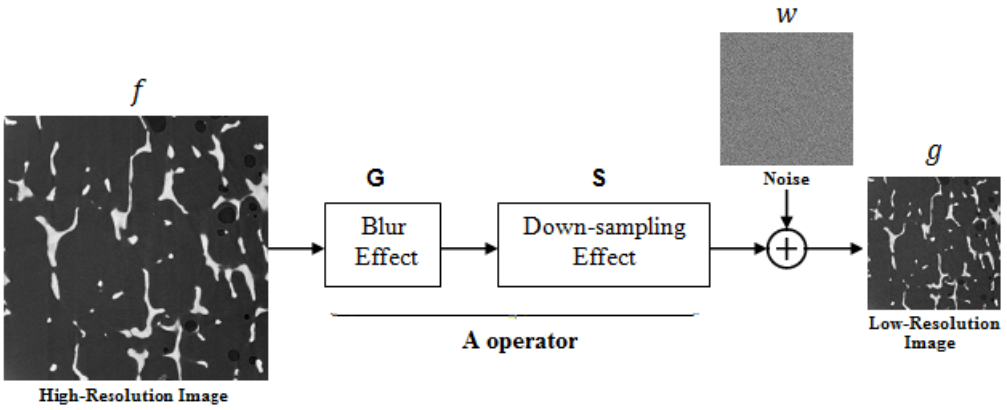

Figure 3.2: Low-resolution image simulation

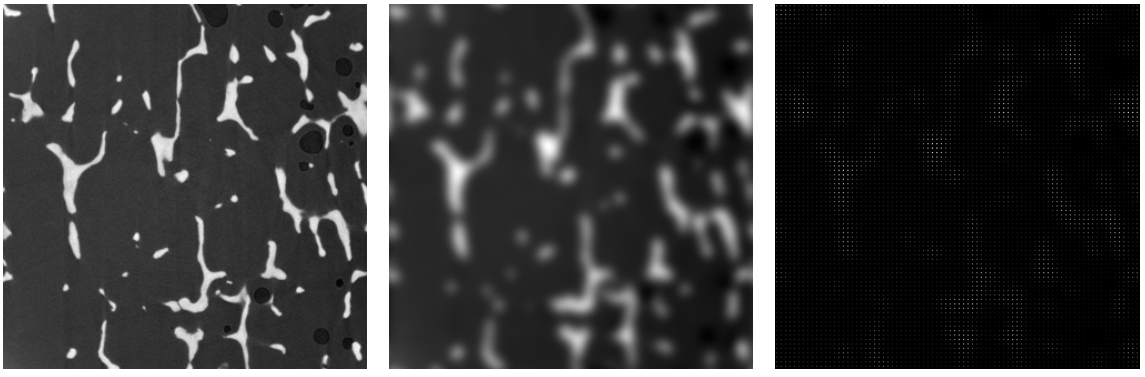

(a) $\boldsymbol{f}$ (b) $G\boldsymbol{f}$ (c) $SG\boldsymbol{f}$

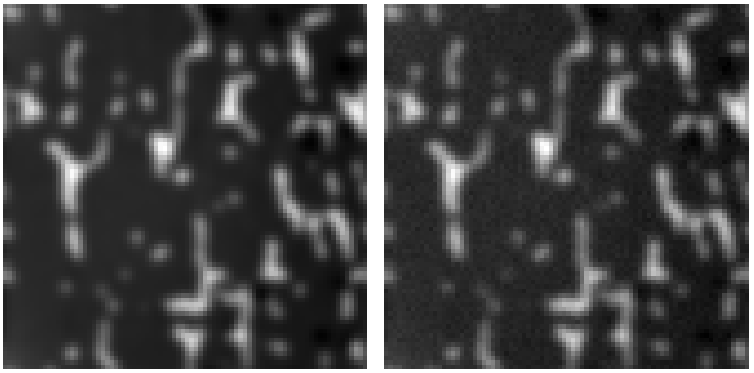

(d) $\boldsymbol{g}$ (e) $\boldsymbol{g}^{\delta}$

Figure 3.3: Low resolution image simulation - step by step.

reflecting the connectivity.

3.6 Results and discussion

For each method studied, the regularization parameter μ is chosen to obtain the maximum PSNR. For a given value of the regularization parameter μ, the ADMM algorithm was applied to obtain the saddle point of the Lagrangian for TV and IHDTV regularization and the PSNR value of the obtained image was computed. The evolution of the PSNR as

a function of μ is displayed in Figure 3.4 for the two methods in the case of test image 4. From these curves the optimal regularization parameters can be estimated.

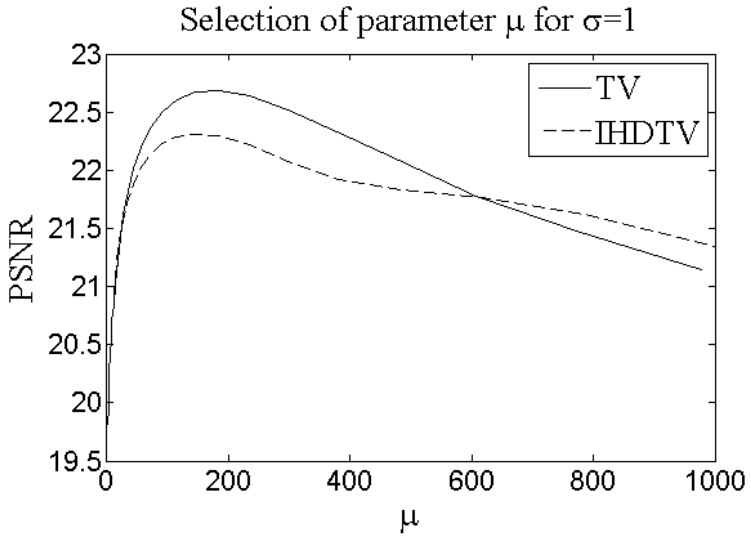

Figure 3.4: Evolution of PSNR for TV and IHDTV methods (test image 4).

Figure 3.5 shows the restoration of the image with TV ADMM iterations for the optimal parameters μ and β. Figure 3.5 (f) corresponds to the final ADMM iteration image for which the stopping criteria value is $\epsilon = 5 \cdot 10^{-5}$. For a fixed regularization parameter μ, the β parameter is chosen in order to have the fastest decrease of the regularization functional, as shown in Figure 3.6 for a given regularization parameter in case of image 3.

We show in Figure 3.7 the influence of the regularization parameter μ and β. All images are at the final ADMM iteration when the stopping condition is achieved.

For two selected images (image 3 and 4), the ground truth, the low resolution and the images obtained with bicubic interpolation and super-resolution methods with the optimal regularization parameters are displayed in Figure 3.8 and Figure 3.9.

By visual inspection of these images it is clear that TV and IHDTV improve the results given by interpolation. A more extensive comparison between the different methods is based on the quantitative parameters summarized in Figure 3.10 and in Table 1-4. We report the PSNR, the DICE coefficient, the bone surface and the Euler number.

Table 3.1: Quantitative parameters (image 1 - tb317).

Parameter	**Reference**	**Bicubic interpolation**	**TV**	**IHDTV**
PSNR	-	16.633	**20.719**	20.237
DICE	1	0.698	0.861	**0.865**
Euler no.	37	14	22	**25**
Bone surface (mm^2)	2.266	3.781	**2.689**	2.759

The results show that the TV based methods gives similar results considering the

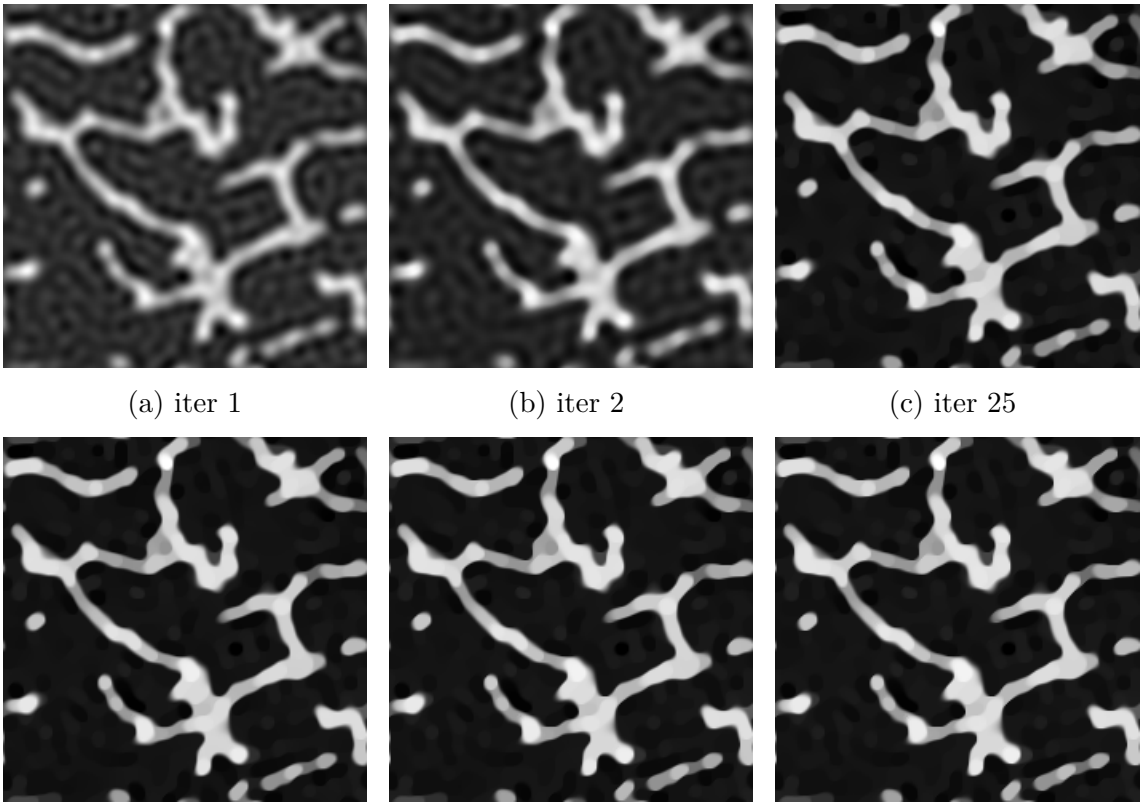

(a) iter 1 (b) iter 2 (c) iter 25

(d) iter 50 (e) iter 113 (f) iter 181

Figure 3.5: The evolution of the image with the ADMM iterations for the optimal parameters μ and β.

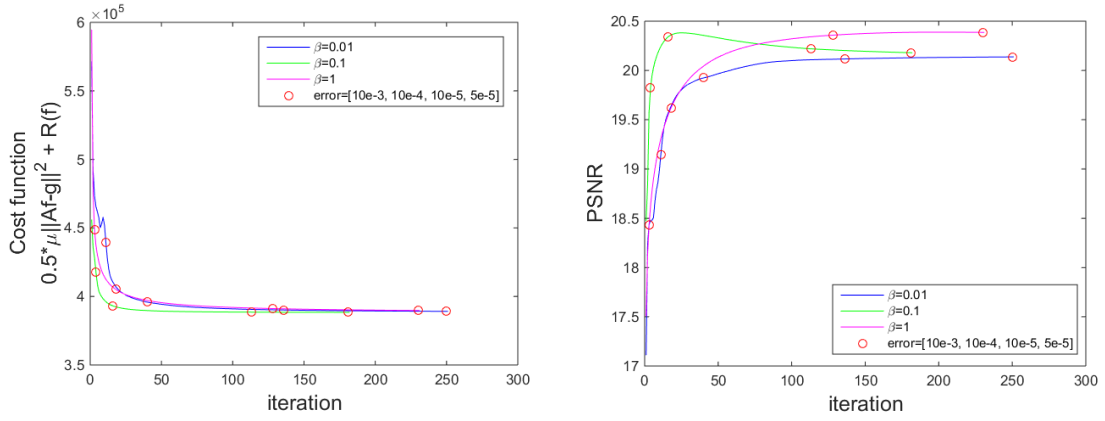

(a) The cost function (b)The PSNR evolution

Figure 3.6: (a) The choice of β for the optimal regularization parameter $\mu = 138$. $\beta = 0.1$ is chosen as it minimizes faster the cost function. (b) The corespondent PSNR evolutions curves.

PSNR. The DICE coefficients are also very similar. However, better results are obtained for the bone surface for the TV method. The same conclusions were obtained for different

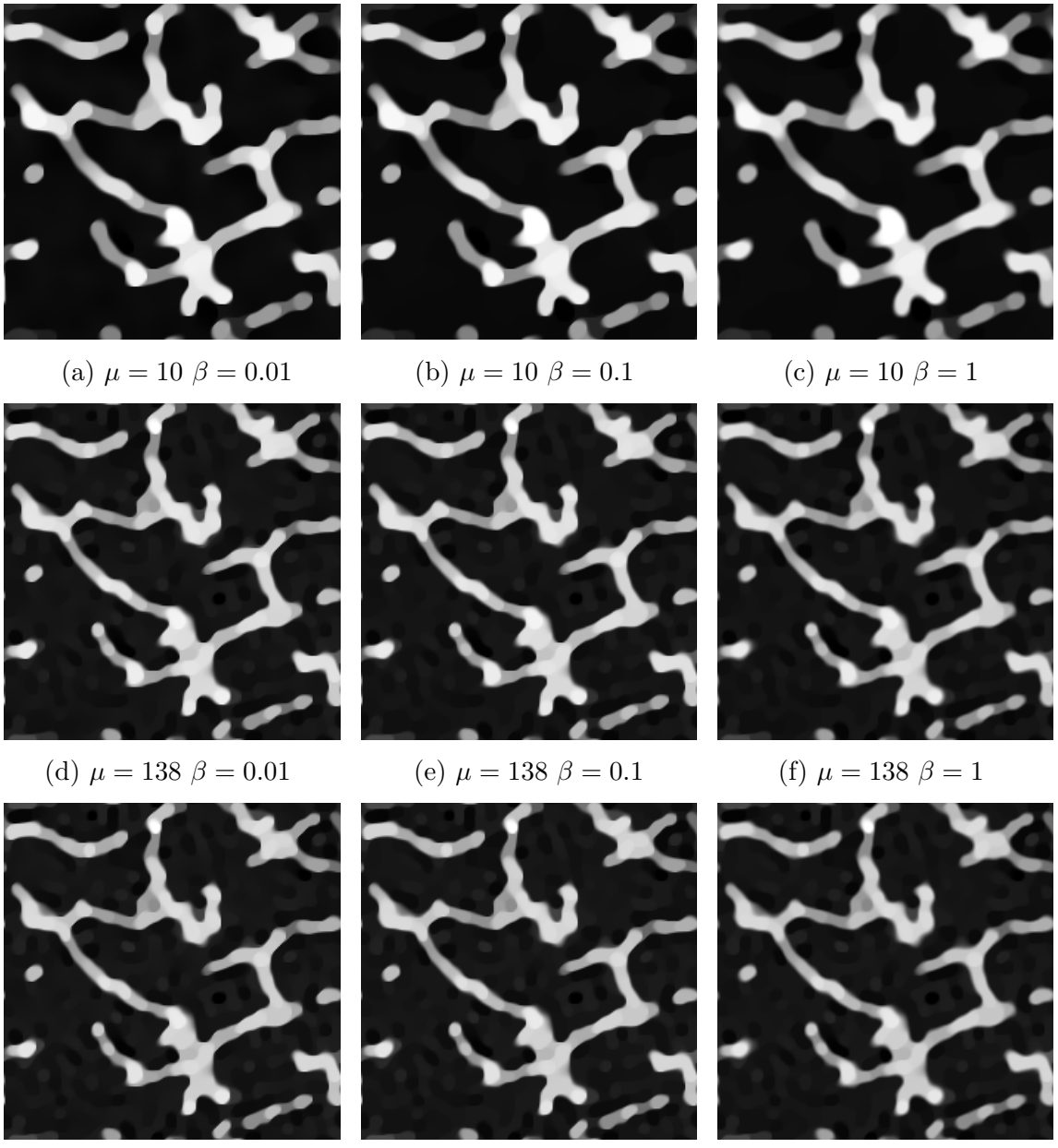

(a) $\mu = 10$ $\beta = 0.01$ (b) $\mu = 10$ $\beta = 0.1$ (c) $\mu = 10$ $\beta = 1$

(d) $\mu = 138$ $\beta = 0.01$ (e) $\mu = 138$ $\beta = 0.1$ (f) $\mu = 138$ $\beta = 1$

(g) $\mu = 200$ $\beta = 0.01$ (h) $\mu = 200$ $\beta = 0.1$ (i) $\mu = 200$ $\beta = 1$

Figure 3.7: The influence of the regularization parameter μ and β for TV ADMM super-resolution.

Table 3.2: Quantitative parameters (image 2 - tb331).

Parameter	**Reference**	**Bicubic interpolation**	**TV**	**IHDTV**
PSNR	-	16.962	**22.052**	20.935
DICE	1	0.762	**0.904**	0.902
Euler no.	19	13	15	**16**
Bone surface (mm^2)	2.216	3.222	**2.488**	2.555

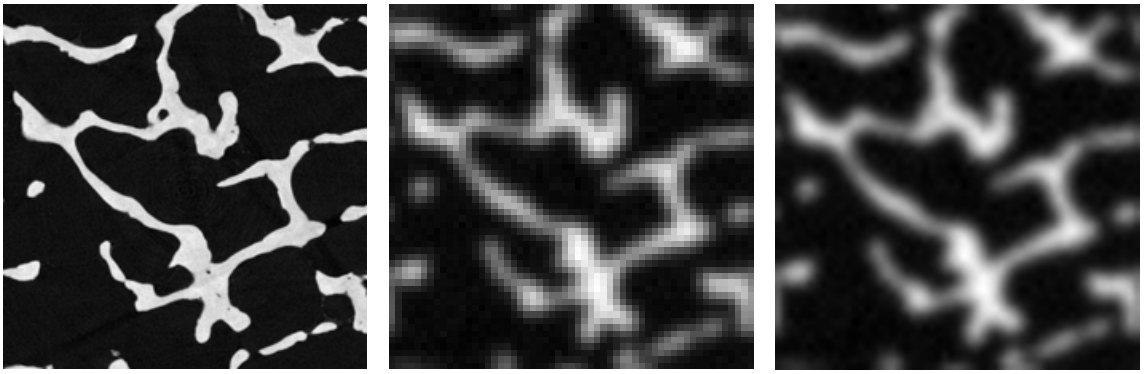

(a) $\boldsymbol{f}$ (b) $\boldsymbol{g}^{\delta}$ (c) Bicubic interpolation

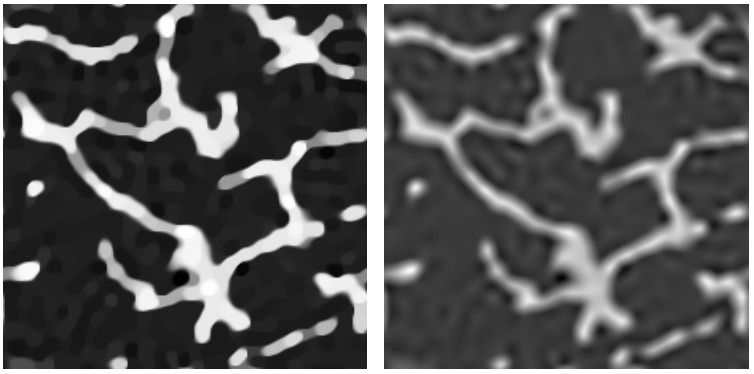

(d) $\boldsymbol{f}_{TV}$ (e) $\boldsymbol{f}_{IHDTV}$

Figure 3.8: Comparison of experimental super-resolution results (image 3).

Table 3.3: Quantitative parameters (image 3 - tb332).

Parameter	Reference	Bicubic interpolation	TV	IHDTV
PSNR	-	15.03	**20.55**	19.02
DICE	1	0.80	0.9201	**0.9202**
Euler no.	15	12	17	**15**
Bone surface (mm^2)	4.04	5.69	**4.49**	4.54

Table 3.4: Quantitative parameters (image 4 - calca47b).

Parameter	Reference	Bicubic interpolation	TV	IHDTV
PSNR	-	18.95	22.36	**22.54**
DICE	1	0.654	**0.811**	0.809
Euler no.	68	48	60	60
Bone surface (mm^2)	3.95	7.23	**5.336**	5.489

values of ϵ. The bone volume and the Euler number are important indicators of bone strength. It can be seen that the error is considerably reduced with respect to the interpolated image and even more by comparison to the degraded image, which is at the same

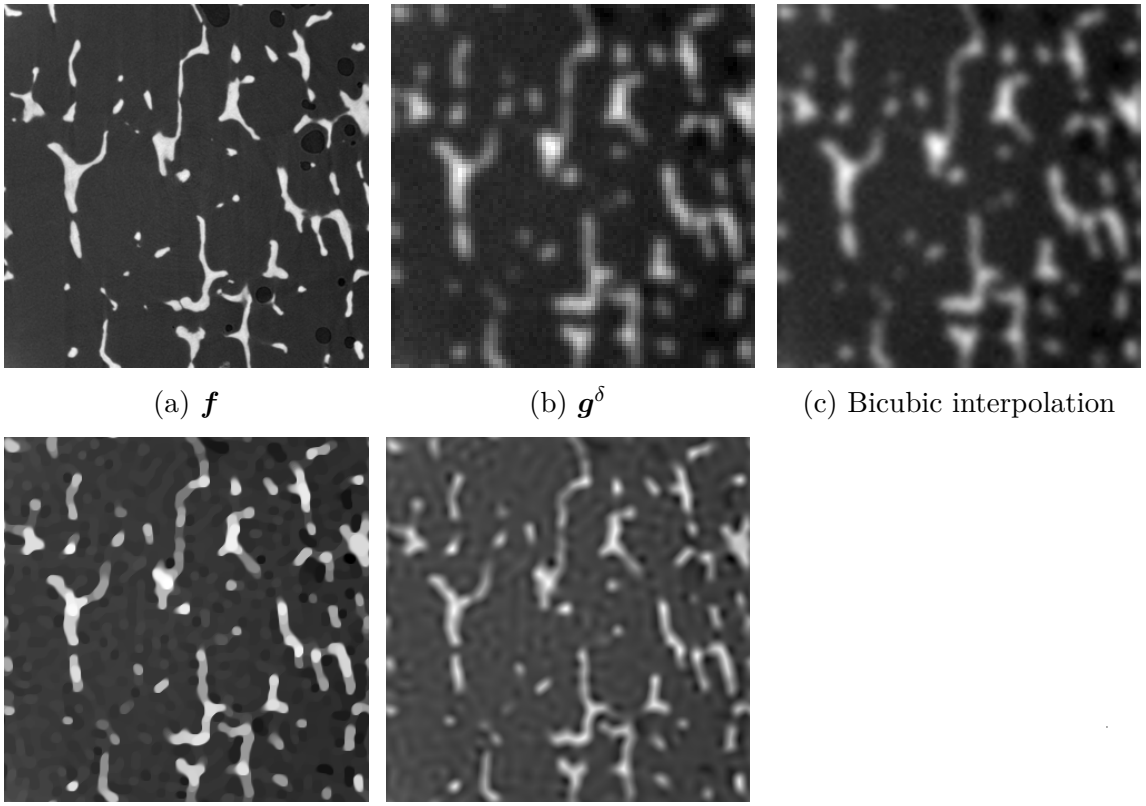

(a) $\boldsymbol{f}$ (b) $\boldsymbol{g}^{\delta}$ (c) Bicubic interpolation

(d) $\boldsymbol{f}_{TV}$ (e) $\boldsymbol{f}_{IHDTV}$

Figure 3.9: Comparison of experimental super-resolution results (image 4).

resolution as that used in clinical trials.

3.7 Conclusions

In this chapter, we proposed to improve the spatial resolution of bone micro-structure CT images by super-resolution techniques. We compared a standard interpolation method and super-resolution methods based on standard TV and the recently proposed Isotropic Higher Order TV scheme.

We recasted each regularization into a similar expression and derived an efficient minimization scheme based on ADMM algorithm. Since the hessian matrix in super-resolution problems does not have a block circulant with circulant block structure, a preconditioned conjugate gradient algorithm has been proposed to speed up the calculation. A comparison of the regularization approaches is done on noisy low-resolution images of the bone micro-structure in terms of PSNR, structural and segmentation parameters. Both TV methods surpass the results of bicubic interpolation with respect to all criteria. TV and IHDTV give similar results.

We continue our research in the framework of TV ADMM method considering that our final goal is the quantification of resulted binary images. Thus, in the context of segmen-

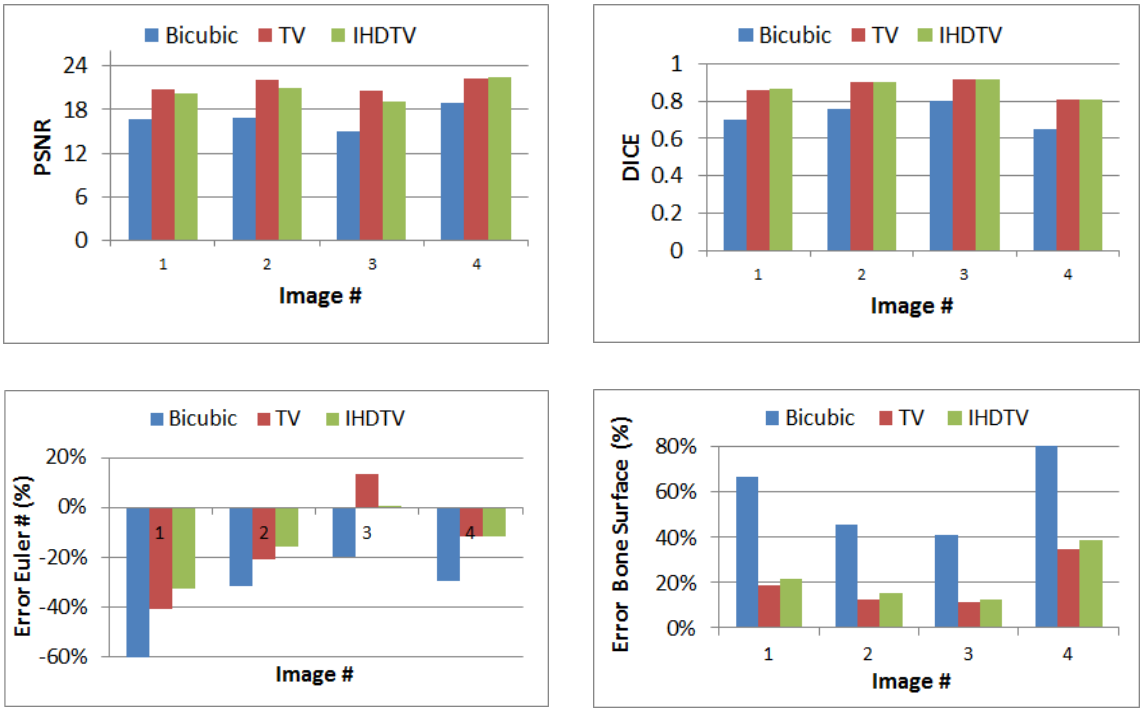

Figure 3.10: PSNR, DICE, Euler #, Bone surface for TV and IHDTV Super-resolution.

tation, TV is preferred as it provides an image that is closer to a piecewise constant model. Next chapter considers the problem of regularization parameter selection in deconvolution and super-resolution TV regularization minimized with ADMM.

Chapter 4

Regularization Parameter Selection

When an ill-posed problem is solved by regularization approaches, the parameter that balances the two terms of the functional has a very important role in the quality of the solution. Thus, in this chapter we will focus on how we select the regularization parameter to be as close as possible to the optimal one.

We propose a fast and simple method to select the regularization parameter for the restoration with TV regularization of an image f from a blurred, noisy image g^δ with various sub-sampling rates. Our contribution in this field is to design an iterative method following the idea of the model function for Tikhonov regularization from [Kunisch and Zou (1998)].

The outline of this chapter is the following. We start by a state of the art of the regularization parameter selection methods. In Section 4.2, we present the linear inverse problem studied, the Morozov discrepancy principle, a damped version of it, and some convergence results associated to our regularization parameter selection method and the ADMM/TV algorithm chosen to estimate the regularized solutions. In Section 4.3, the new method for the selection of the regularization parameter is presented. In Section 4.4, we detail the UPRE method that will be used for comparison. In Section 4.5, numerical results are given to demonstrate the effectiveness of the approach for deconvolution or super-resolution problems. Concluding remarks are given in the last section.

The method and the results presented in this chapter have been published in the following journal:
A. Toma, B. Sixou, F. Peyrin, (2015) "Iterative choice of the optimal regularization parameter in TV image restoration", Journal of Inverse Problems and Imaging, 9(4): 1171-1191

4.1 State of the art

In order to obtain a good reconstructed image, it is necessary to choose an optimal regularization parameter. A very common approach is to try various values until the reconstruction solution is satisfactory. For large scale problems, an exhaustive search with a grid of points of regularization parameters values is very slow. Several methods have been studied for the optimal selection of the regularization parameter for Tikhonov regularization. Approaches like the discrepancy principle and the Unbiased Predictive Risk Estimator are based on a knowledge of the noise level δ [Vogel (2002), Morozov (1984), Blu and Luisier (2007), Eldar (2009), Ramani *et al.* (2008), Vaiter *et al.* (2013), Deledalle *et al.* (2014), Ramani *et al.* (2012), Vonesch *et al.* (2008)]. The L-curve method and the Generalized Cross-Validation can be used without the knowledge of this noise level [Golub *et al.* (1979), Hansen and O'Leary (1993)]. Furthermore, an iterative choice of the regularization parameters based on the Morozov discrepancy principle applied with a model function has been proposed in [Kunisch and Zou (1998)].
For TV regularization, fewer methods have been investigated. Regarding denoising problems, [Aujol and Gilboa (2006)] have proposed a method where the denoised result is close to the optimal, in the SNR sense. An extension of the Unbiased Predictive Risk Estimator to TV regularization has been shown to give a good estimate of the regularization parameter [Lin *et al.* (2010)]. A method exploiting the Generalized Cross-Validation technique has been proposed in [Liao *et al.* (2009)]. Babacan et *al.* [Babacan *et al.* (2008)a, Babacan *et al.* (2008)b] have studied a bayesian variational method for solving TV deconvolution and super-resolution problems. A new approach based on a proximal point method applied to the dual formulation of the TV regularization problem and the discrepancy principle has been proposed recently [Wen and Chan (2012)].

4.2 TV regularization, Morozov based principles and ADMM approach

4.2.1 Problem formulation

Let Ω be a bounded open domain with Lipschitz boundary. In the following, we consider a linear operator $A : L_2(\Omega) \to L_2(\Omega)$. We assume that A is injective and continuous. We consider the regularization functional:

$$J_{\mu,g^\delta}(f) = \mu \frac{\|Af - g^\delta\|^2}{2} + R_{TV}(f) \tag{4.1}$$

where μ is a regularization parameter. The Total Variation regularization has been extensively studied in [Scherzer *et al.* (2008), Ambrosio *et al.* (2000)]. The following theorem summarizes the main convergence and stability results.

Theorem 4.2.1. *Let A be a linear and bounded operator $A : L_2(\Omega) \to L_2(\Omega)$, satisfying $Aq \neq 0$ for all constants $q \in L_2(\Omega)$. The space $L_2(\Omega)$ is assumed to be endowed with its weak topology. Then:*

- the TV semi-norm is convex and lower semicontinuous with respect to the weak topology on $L_2(\Omega)$.

- the level sets $\{f \in L_2(\Omega),\ \mu\frac{\|Af-g^\delta\|^2}{2} + R_{TV}(f) \leq M\}$ are sequentially pre-compact with respect to the weak topology on $L_2(\Omega)$, for any positive numbers M and μ.

- consequently, the regularization with the TV semi-norm is well-defined, stable and convergent.

Let (g_k) be a sequence converging toward g^δ, and f_k be a minimizer of the regularization functional J_{μ,g_k}, the stability of the regularization method means that every convergent subsequence of (f_k) converges to a minimizer of $J_{\mu,g}$. Let (δ_k) be a sequence of positive numbers converging to 0, and (g_k) a sequence such that $\|g-g_k\| \leq \delta_k$, the TV regularization method is convergent and thus for a good choice of the parameter $\mu(\delta_k)$, the sequence (f_k) has a convergent subsequence. The limit is a minimal norm solution [Scherzer *et al.* (2008)].

4.2.2 Morozov and modified Morozov principle, basic properties

With the Morozov discrepancy principle [Engl *et al.* (1996)], the regularization parameter is chosen such that the discrepancy term is equal to the known noise level δ on the observed data, so that the following equation for μ holds :

$$\|Af(\mu) - g^\delta\| = \delta \tag{4.2}$$

In some cases, the use of the Morozov discrepancy principle may not lead to an optimal regularization parameter. As suggested in [Kunisch (1993), Kunisch and Zou (1998)], a

damped Morozov equation may be more satisfactory. We have therefore considered the damped equation:

$$\|g^\delta - Af(\mu)\|^2 + \mu^\gamma R_{TV}(f(\mu)) = \delta^2 \tag{4.3}$$

where the exponent γ has to be chosen.

We first study the range of the functions $P(f(\mu)) = \|g^\delta - Af(\mu)\|^2$ and $P_\gamma(f(\mu)) = \|g^\delta - Af(\mu)\|^2 + \mu^\gamma R_{TV}(f(\mu))$. We define:

$$\eta = \inf\{\|Af - g^\delta\|, f \in L_2(\Omega)\} \tag{4.4}$$

and

$$\nu = \inf\{\|Af_C - g^\delta\|, f_C = C \text{ on } \Omega, C \in \mathbb{R}\} \tag{4.5}$$

We denote f_0 the value of f for which the minimum ν is obtained. We are first interested in some basic properties of P_γ and P. The proofs are similar to the one given in [Kunisch (1993)], but some changes are necessary because of the use of the TV regularization term.

Lemma 4.2.2. *For $\gamma \leq -1$, $P_\gamma(f(\mu)) \geq \nu^2$ as $\mu \to 0$. As $\mu \to \infty$, $P_\gamma(f(\mu)) \to \eta^2$. The same results hold for P.*

Proof. The minimum of $J_\mu(f)$ is obtained for $f(\mu)$ and $R_{TV}(f_0) = 0$ thus:

$$\begin{aligned}\frac{\|Af(\mu) - g^\delta\|^2}{2} + \mu^{-1} R_{TV}(f(\mu)) &\leq \frac{\|Af_0 - g^\delta\|^2}{2} + \mu^{-1} R_{TV}(f_0) \\ &\leq \frac{\nu^2}{2} + \mu^{-1} R_{TV}(f(\mu))\end{aligned}$$

consequently $\|Af(\mu) - g^\delta\| \leq \nu$ and $R_{TV}(f(\mu)) \leq \mu \frac{\|Af_0 - g^\delta\|^2}{2}$.

Therefore $R_{TV}(f(\mu)) \to 0$ as $\mu \to 0$. Let $< f >$ be the average value of $f(\mu)$ on Ω, $(R_{TV}(f(\mu)) - < f >) \to 0$ as $\mu \to 0$. As the TV semi-norm is equivalent to the BV norm for functions with zero average value [Scherzer *et al.* (2008)], this result implies $\|(f(\mu) - < f >)\|_{BV} \to 0$ as $\mu \to 0$. Thus $f(\mu) \to < f >$ in $L_2(\Omega)$ since BV is continuously embedded in $L_2(\Omega)$ [Scherzer *et al.* (2008)]. The operator A is continuous on $L_2(\Omega)$ and thus $\|Af(\mu) - g^\delta\|^2 \to \|A < f > - g^\delta\|^2$ as $\mu \to 0$. Consequently $P_\gamma(f(\mu)) \geq \nu^2$ as $\mu \to 0$

For $\epsilon > 0$, we consider f_ϵ such that $\|Af_\epsilon - g^\delta\| \leq \eta + \epsilon$.

$$\begin{aligned}\frac{\|Af(\mu) - g^\delta\|^2}{2} + \mu^{-1} R_{TV}(f(\mu)) &\leq \frac{\|Af_\epsilon - g^\delta\|^2}{2} + \mu^{-1} R_{TV}(f_\epsilon) \\ &\leq \frac{(\eta + \epsilon)^2}{2} + \mu^{-1} R_{TV}(f_\epsilon)\end{aligned}$$

and thus for $\mu \geq 1$ and $\gamma \leq -1$, $\mu^\gamma < \frac{2}{\mu}$ and

$$\|Af(\mu) - g^\delta\|^2 + \mu^\gamma R_{TV}(f(\mu)) \leq (\eta + \epsilon)^2 + 2\mu^{-1} R_{TV}(f_\epsilon) \tag{4.6}$$

On the other hand, $\|Af(\mu) - g^\delta\|^2 + \mu^\gamma R_{TV}(f(\mu)) \geq \eta^2$.

Let $\mu_1 = 2R_{TV}(f_\epsilon)/\epsilon^2$, then it follows from (4.6) that for $\mu \geq \mu_1$, $\sqrt{P_\gamma(f(\mu))} \leq \eta + 2\epsilon$ and thus $P_\gamma(f(\mu)) \to \eta^2$ as $\mu \to \infty$. From the former results, it follows that $P(f(\mu)) \geq \nu^2$ as $\mu \to 0$ and $P(f(\mu)) \to \eta^2$ as $\mu \to \infty$. □

4.2.3 Convergence results

The convergence rates of regularized solutions for ill-posed operator equations require additional properties of the true solution f^* of the equation $Af = g$ such as source conditions. Convergence rates results can be obtained in terms of Bregman distance between the true and the regularized solution [Burger and Osher (2004), Resmerita (2005), Scherzer *et al.* (2008)]. The Bregman distance is a measure of the difference between two elements in a Banach space [Kiwiel (1997), Bregman (1967)]. The use of this distance has now evolved as a standard tool for error measure. For a element $\xi \in \partial R_{TV}(v)$, where $\partial R_{TV}(v)$ denotes the subdifferential of TV at v, the Bregman distance with respect to TV between u and v at ξ is defined by: $D_{TV}^{\xi}(u, v) = R_{TV}(u) - R_{TV}(v) - \langle \xi, u - v \rangle$. In the following, we assume the standard source condition holds and $\tau \in L_2(\Omega)$ exists such that:

$$\xi = A(f^*)^* \tau \in \partial R_{TV}(f^*) \tag{4.7}$$

Some convergence results have been obtained for a priori choices of the regularization parameter [Scherzer *et al.* (2008), Grasmair (2011)] given by the following proposition:

Proposition 4.2.3. *Assuming that the former source condition holds, for the choice* $1/\mu \sim \delta$, *the Bregman distance between the regularized solution and the ground truth is* $D_{TV}^{\xi}(f(\mu), f^*) = O(\delta)$.

This control of the error in terms of Bregman divergence was extended by a l_2 control in the discrete setting [Fadili *et al.* (2013)]. We present here some convergence rates results as the error level $\delta \to 0$. We develop an error estimation when the regularization parameter $\mu(g^\delta, \delta)$ is chosen according to the modified Morozov principle (4.3). We first show that the TV norm of $f(\mu)$ is uniformly bounded if the modified Morozov principle is satisfied.

Lemma 4.2.4. *If the regularization parameter is chosen according to the modified Morozov principle,* $\mu > 2^{\frac{1}{\gamma+1}}$ *and* $\gamma < -1$, *the TV semi-norm of the regularized solution* $R_{TV}(f(\mu))$ *is uniformly bounded.*

Proof. From the definition of $f(\mu)$, we have:

$$\frac{\|Af(\mu) - g^\delta\|^2}{2} + \mu^{-1} R_{TV}(f(\mu)) \leq \frac{\delta^2}{2} + \mu^{-1} R_{TV}(f^*) \tag{4.8}$$

Combining the modified Morozov Principle and (4.8), we obtain:

$$\begin{aligned}\frac{\|Af(\mu)-g^\delta\|^2}{2}+\mu^{-1}R_{TV}(f(\mu)) &= \frac{\|Af(\mu)-g^\delta\|^2}{2}+(\mu^{-1}-\frac{\mu^\gamma}{2})R_{TV}(f(\mu))\\ &\quad+\frac{\mu^\gamma}{2}R_{TV}(f(\mu))\\ &= \frac{\delta^2}{2}+(\mu^{-1}-\frac{\mu^\gamma}{2})R_{TV}(f(\mu))\\ &\leq \frac{\delta^2}{2}+\mu^{-1}R_{TV}(f^*)\end{aligned}$$

and consequently $R_{TV}(f(\mu)) \leq \frac{1}{1-\frac{\mu^{\gamma+1}}{2}}R_{TV}(f^*)$. For $\mu \geq \mu_0$ with $\mu_0 > 2^{\frac{1}{\gamma+1}}$ and $\gamma+1<0$

$$R_{TV}(f(\mu)) \leq \frac{1}{1-\frac{\mu_0^{\gamma+1}}{2}}R_{TV}(f^*), \tag{4.9}$$

$R_{TV}(f(\mu))$ is thus uniformly bounded. □

Proposition 4.2.5. *If the regularization parameter is chosen according to the modified Morozov principle, the Bregman distance between the true solution and the regularized solution is given by* $D_{TV}^{\xi}(f(\mu),f^*) = O(\delta^{min(1,2(\gamma+1)/\gamma)})$.

Proof. From the proof of Proposition 3.41 in [Scherzer *et al.* (2008)], it can be shown that if assumption (4.7) holds, then there exist $\beta_1 \in [0,1[$, $\beta_2 \geq 0$ and $\xi \in \partial R_{TV}(f^*)$ such that:

$$\|Af(\mu)-g^\delta\|^2+\frac{1}{\mu}D_{TV}^{\xi}(f(\mu),f^*) \leq \delta^2+\frac{1}{\mu}(\beta_1 D_{TV}^{\xi}(f(\mu),f^*)+\beta_2(\|Af(\mu)-g^\delta\|+\delta)) \tag{4.10}$$

With the choice of $\mu(g^\delta,\delta)$ according to the modified Morozov principle:

$$\frac{1}{\mu}D_{TV}^{\xi}(f(\mu),f^*) \leq \frac{1}{\mu}(\beta_1 D_{TV}^{\xi}(f(\mu),f^*)+\beta_2(\|Af(\mu)-g^\delta\|+\delta))+\mu^\gamma R_{TV}(f(\mu)) \tag{4.11}$$

and thus

$$D_{TV}^{\xi}(f(\mu),f^*)(1-\beta_1) \leq \beta_2(\|Af(\mu)-g^\delta\|+\delta)+\mu^{\gamma+1}R_{TV}(f(\mu)). \tag{4.12}$$

The modified Morozov principle implies $\mu^\gamma R_{TV}(f(\mu)) \leq \delta^2$ and we obtain

$$D_{TV}^{\xi}(f(\mu),f^*)(1-\beta_1) \leq \beta_2(\|Af(\mu)-g^\delta\|+\delta)+\delta^{2(\gamma+1)/\gamma}R_{TV}(f(\mu))^{-1/\gamma} \tag{4.13}$$

and with (4.9), it results that:

$$\begin{aligned}D_{TV}^{\xi}(f(\mu),f^*)(1-\beta_1) &\leq \beta_2(\|Af(\mu)-g^\delta\|+\delta)+\frac{1}{1-\frac{\mu_0^{\gamma+1}}{2}}\delta^{2(\gamma+1)/\gamma}R_{TV}(f^*)^{-1/\gamma}\\ &\leq 2\beta_2\delta+\frac{1}{1-\frac{\mu_0^{\gamma+1}}{2}}\delta^{2(\gamma+1)/\gamma}R_{TV}(f^*)^{-1/\gamma}\end{aligned}$$

and therefore $D_{TV}^{\xi}(f(\mu), f^*) = O(\delta^{min(1,2(\gamma+1)/\gamma)})$. □

4.3 Proposed Morozov based regularization parameter selection methods

In this section, we detail two numerical schemes to choose the regularization parameter. We assume that $f(\mu)$ is a minimum R_{TV} norm solution and that it is unique. We first show, under restrictive conditions, the differentiability of the function f and of the value function E around μ, that are functional properties on which the iterative scheme relies.

4.3.1 Lipschitz continuity and differentiability of $f(\mu)$

We consider here the function $f : \mathbb{R} \to \mathbb{R}^N$ of the regularization parameter. The results in this section will be formulated in a discrete setting. They can be generalized to the continuous setting if the subdifferential of the discret TV semi-norm $\sum D_i^t(\partial\|D_i f(\mu)\|)$ is replaced by its continuous version.

Proposition 4.3.1. *Under the assumptions of Theorem 2.1, the regularized solution f is continuous around the regularization parameter μ.*

Proof. We first show that f is Lipschitz continuous around μ. Subtracting the KKT condition for $\mu + t$ and μ yields:

$$\mu A^t A(f(\mu+t) - f(\mu)) \in tA^t Af(\mu+t) + tA^t g^\delta - \sum D_i^t(\partial\|D_i f(\mu+t)\| - \partial\|D_i f(\mu)\|). \tag{4.14}$$

Taking the inner product with $f(\mu + t) - f(\mu)$, using the Schwarz inequality, considering that f is bounded and applying the monotonicity of the subdifferential, we obtain:

$$\mu\|A(f(\mu+t) - f(\mu))\|^2 \leq C_1|t|\|f(\mu+t) - f(\mu)\| \tag{4.15}$$

where C_1 is a positive constant and

$$\sum < \partial\|D_i f(\mu+t)\|_2 - \partial\|D_i f(\mu)\|_2, D_i(f(\mu+t) - f(\mu)) > \leq C_1|t|\|f(\mu+t) - f(\mu)\| \tag{4.16}$$

If A is injective, $\|A(f(\mu+t) - f(\mu))\|^2 \geq \alpha_{min}\|(f(\mu+t) - f(\mu))\|^2$, where α_{min} is the minimum singular value of A^tA and thus f is Lipschitz continuous around μ.

The regularization functional for the regularization parameter $\mu + t$ is minimized for $f(\mu + t)$ and thus:

$$(\mu+t)\frac{\|Af(\mu+t) - g^\delta\|^2}{2} + R_{TV}(f(\mu+t)) \leq (\mu+t)\frac{\|Af(\mu) - g^\delta\|^2}{2} + R_{TV}(f(\mu)) \tag{4.17}$$

and thus, there are constants C_2, C_3 such that:

$$\begin{aligned} 0 \leq R_{TV}(f(\mu+t)) - R_{TV}(f(\mu)) \leq & t\frac{\|Af(\mu)-g^\delta\|^2}{2} \\ & + \mu(\frac{\|Af(\mu)-g^\delta\|^2}{2} - \frac{\|Af(\mu+t)-g^\delta\|^2}{2}) \\ & \leq t\frac{\|Af(\mu)-g^\delta\|^2}{2} + C_2\|Af(\mu+t)-Af(\mu)\| \\ & \leq C_3\sqrt{t} \end{aligned} \tag{4.18}$$

where we have used (4.15).
From (4.16), we can deduce that, for all i, as $t \to 0$, $D_i f(\mu+t) = 0$ if and only if $D_i f(\mu) = 0$, and that the components of $D_i f(\mu)$ and $D_i f(\mu+t)$ have the same sign. Therefore, as $t \to 0$, we have, $R_{TV}(f(\mu+t)) - R_{TV}(f(\mu)) \sim R_{TV}(f(\mu+t) - f(\mu))$, and there is a positive constant C_4 such that

$$R_{TV}(f(\mu+t) - f(\mu)) \leq C_4\sqrt{t} \tag{4.19}$$

Let $BV(\Omega)_\diamondsuit$, the set of all functions of bounded variation with zero mean, then on $BV(\Omega)_\diamondsuit$ the TV and BV norm are equivalent [Scherzer *et al.* (2008)]:

$$R_{TV}(f) \leq \|f\|_{BV} \leq C_2 R_{TV}(f) \quad ,\forall \quad f \in BV(\Omega)_\diamondsuit \tag{4.20}$$

This property is also verified for the discrete TV semi-norm. Let us denote $\Delta f = f(\mu + t) - f(\mu)$, and $M : L_1(\Omega) \to L_1(\Omega)$ the averaging operator of a function f. The operator M is linear and continuous. In a continuous setting, the operator M is defined by:

$$M(f) = 1_\Omega \int_\Omega f(x) \quad ,\forall f \in L_1(\Omega) \tag{4.21}$$

where 1_Ω is the indicator function of the set Ω. Using the operator M we have:

$$\|f(\mu+t) - f(\mu)\|_1 \leq \|M(\Delta f)\|_1 + \|\Delta f - M(\Delta f)\|_1 \tag{4.22}$$

Under the assumption that the operator A is injective on the set of constant functions, we obtain that there is a positive constant C_5 such that:

$$\|M(\Delta f)\|_1 \leq C_5\|AM(\Delta f)\|_2 \tag{4.23}$$

Using (4.20) and (4.23), we get:

$$\begin{aligned} \|f(\mu+t) - f(\mu)\|_1 &\leq C_5\|AM(\Delta f)\|_2 + C_2 R_{TV}(\Delta f - M(\Delta f)) \\ &\leq C_5\|AM(\Delta f)\|_2 + C_2 R_{TV}(\Delta f) \end{aligned} \tag{4.24}$$

We now assume that the operator A commutes with M. It can be easily shown that it

is the case for the convolution integral operator investigated in the following. Using the continuity of M, (4.15) and (4.19), we thus obtain that, as $t \to 0$ there is positive constant D such that:

$$\begin{aligned} \|f(\mu+t) - f(\mu)\|_1 &\leq C_5 \|MA(\Delta f)\|_2 + C_2 R_{TV}(\Delta f) \\ &\leq D\sqrt{t} \end{aligned} \tag{4.25}$$

□

We now demonstrate that under some restricted injectivity condition, the regularized solution is a differentiable function of the regularization parameter.

Proposition 4.3.2. *Let us assume there exists a constant $E > 0$ such that the operator A is injective on the subset $\mathcal{C}$ of $BV(\Omega)$, defined by:*

$$\mathcal{C} = \{g \quad \in \quad BV(\Omega), \| \sum D_i^t \frac{D_i g}{\|D_i g\|} - \sum D_i^t \frac{D_i f(\mu)}{\|D_i f(\mu)\}\|} \| \leq E\} \tag{4.26}$$

Then, the regularized solution f is differentiable around the regularization parameter μ.

Proof. We now show that the function f is differentiable around μ and that its derivative is the unique solution ω of:

$$\mu A^t A\omega = A^t g^\delta - A^t A f(\mu) \quad a.e \tag{4.27}$$

We assume that the operator A is injective on the subset $\mathcal{C}$. Let $\epsilon = (f(\mu+t) - f(\mu)) - t\omega$. Dividing (4.14) by t and substracting (4.27), we obtain:

$$\langle \mu A^t A\epsilon, \epsilon \rangle = -\langle A^t A(f(\mu+t) - f(\mu)), \epsilon \rangle + \sum \langle \gamma_i, \epsilon \rangle. \tag{4.28}$$

with $\langle \gamma_i, \epsilon \rangle = -\langle (\partial \|D_i f(\mu+t)\|_2 - \partial \|D_i f(\mu))\|_2), D_i \epsilon \rangle$.

The optimality condition shows that as $t \to 0$, $f(\mu+t)$ belongs to the set $\mathcal{C}$. It is also the case for ϵ. By the Schwarz inequality:

$$\mu \alpha_{min} \|\epsilon\| \leq \|f(\mu+t) - f(\mu)\| + \sum \|\gamma_i\| \tag{4.29}$$

where α_{min} is the minimal singular value of $A^t A$ restricted to $\mathcal{C}$. When $t \to 0$, $\gamma_i \to 0$, since $\frac{D_i f(\mu)}{\|D_i f(\mu)\|}$ and $\frac{D_i f(\mu+t)}{\|D_i f(\mu+t)\|}$ are equal for all i as $t \to 0$. Therefore $\epsilon \to 0$ and f is thus differentiable around μ. □

4.3.2 Differentiability of the value function $E(\mu)$

In the following, we denote $E(\mu)$ the value obtained at the saddle point for $\mathcal{L}_{\mathrm{A}}(f(\mu), \{\boldsymbol{h}_i^*(\mu)\}, \{\lambda_i^*(\mu)\}, \mu)$.

Proposition 4.3.3. *The value function $E(\mu)$ is twice differentiable with $E'(\mu) = \frac{\|g^\delta - Af(\mu)\|^2}{2}$ and $E''(\mu) = \langle Af(\mu) - g^\delta, Af'(\mu) \rangle$, and $E'(\mu)$ is a decreasing function.*

Proof. The differentiability of E follows from its definition and from the differentiability of $f(\mu)$. Classical differentiability calculation rules gives:

$$\begin{aligned}\partial E(\mu) =&\mu\langle Af(\mu) - g^\delta, Af'(\mu)\rangle + \frac{\|g^\delta - Af(\mu)\|^2}{2} \\ &+ \sum \langle D_i^t \partial \|D_i f(\mu)\|_2, f'(\mu)\rangle.\end{aligned}$$

Taking into account the optimality condition, the first derivative of $E(\mu)$ is given by:

$$E'(\mu) = \frac{\|g^\delta - Af(\mu)\|^2}{2}. \tag{4.30}$$

Thus, the second derivative of $E(\mu)$ is given by:

$$E''(\mu) = \langle Af(\mu) - g^\delta, Af'(\mu)\rangle. \tag{4.31}$$

Using equation (4.27), $E''(\mu)$ can be rewritten:

$$E''(\mu) = -\langle \omega, \mu A^t A\omega\rangle = -\langle A\omega, \mu A\omega\rangle \tag{4.32}$$

We obtain $E''(\mu) \leq 0$. The function $E'(\mu)$ is decreasing and the value function $E(\mu)$ is monotonically increasing and concave. □

4.3.3 Proposed iterative scheme for the classical Morozov principle

In the framework of the Morozov discrepancy principle, the regularization parameter is chosen such that the discrepancy term is equal to the noise level δ, that is $\|g^\delta - Af(\mu)\| = \delta$. This condition can be written $2E'(\mu) = \delta^2$. In order to determine the regularization parameter and to solve the Morozov equation, we have used a two parameters model function. The approximate value of μ obtained is refined with a Newton method. Following the model function methodology in [Kunisch and Zou (1998)], it can be calculated a model function that preserves the main properties of $E'(\mu)$.

Proposition 4.3.4. *The discrepancy term $E'(\mu)$ can be approximated by the decreasing function, $\mu \to a\mu^{-2} + b$, with $(a, b) \in \mathbb{R}^2$.*

Proof. Upon differentiating the optimality condition with respect to μ, we obtain:

$$A^t(Af(\mu) - g^\delta) + \mu A^t(Af'(\mu)) = -\frac{d}{d\mu}\sum D_i^t \frac{D_i f(\mu)}{\|D_i f(\mu)\|_2}. \tag{4.33}$$

Taking the inner product of this equation with $f(\mu)$ and neglecting the second member, we obtain:

$$\langle (Af(\mu) - g^\delta), Af(\mu)\rangle + \mu\langle Af'(\mu), Af(\mu)\rangle = 0 \tag{4.34}$$

This equation will be rewritten:

$$\|Af(\mu) - g^\delta\|^2 + \mu\langle Af'(\mu), Af(\mu) - g^\delta\rangle = \mu\langle Af'(\mu), -g^\delta\rangle + \langle Af(\mu) - g^\delta, -g^\delta\rangle \quad (4.35)$$

If the right member is assumed constant, using (4.30) and (4.31), we get:

$$2E'(\mu) + \mu E''(\mu) = constant \quad (4.36)$$

Solving this differential equation, we obtain a decreasing and convex model function depending on two real parameters a and b:

$$E'(\mu) = a\mu^{-2} + b \quad (4.37)$$

which describes the main properties of the function $E'(\mu)$. □

As expected, this model function is decreasing and the value function $E(\mu)$ is concave. This model function yields an approximate value, μ_{approx}, of the regularization parameter obtained with the equation:

$$2E'(\mu) = \delta^2 \quad (4.38)$$

In a second step, we define the function $G(\mu)$ by:

$$G(\mu) = 2E'(\mu) - \delta^2 \quad (4.39)$$

In order to solve $G(\mu) = 0$, given two initial guess values close to μ_{approx}, μ_0 and μ_1, a sequence of iterates $(\mu_k)_{k\geq 0}$ is generated for $k \geq 1$ by:

$$\mu_{k+1} = \mu_k - \frac{2E'(\mu_k) - \delta^2}{2E''(\mu_k)} \quad (4.40)$$

where the value $f'(\mu_k)$ in $E''(\mu_k)$ is approximated with $\frac{f(\mu_k)-f(\mu_{k-1})}{\mu_k-\mu_{k-1}}$.

4.3.4 Proposed iterative scheme for the damped Morozov principle

With the damped Morozov principle [Kunisch (1993), Kunisch and Zou (1998)], we have to consider the modified equation:

$$\|g^\delta - Af(\mu)\|^2 + \mu^\gamma R_{TV}(f(\mu)) = \delta^2 \quad (4.41)$$

for a parameter γ. The first step of the iterative scheme is the same. For the Newton refinement step, we can redefine the function $G(\mu)$ as:

$$G(\mu) = \|g^\delta - Af(\mu)\|^2 + \mu^\gamma R_{TV}(f(\mu)) - \delta^2 \quad (4.42)$$

From an approximate value calculated with the model function of the classical Morozov principle, the optimal regularization parameter can be obtained with the Newton method by defining a sequence $(\mu_k)_{k\geq 0}$, given μ_0 and μ_1, two initial guess values close to μ_{approx} and applying:

$$\mu_{k+1} = \mu_k - \frac{G(\mu_k)}{G'(\mu_k)} \tag{4.43}$$

Taking into account the differentiability of the value function $E(\mu)$ for a smoothed version of the gradient, it is possible to demonstrate that $G(\mu)$ is decreasing for some values of μ and γ:

Proposition 4.3.5. *The function $\mu \to G(\mu)$ is strictly decreasing for $\gamma = -1$ and $\mu > 0$ and for $\gamma < -1$ and $\mu > 2^{1/(\gamma+1)}$.*

Proof. With the value function $E(\mu) = \frac{\mu\|g^\delta - Af(\mu)\|^2}{2} + R_{TV}(f(\mu))$, and $E'(\mu)$ given by (4.30), $G(\mu)$ can be rewritten as:

$$G(\mu) = 2E'(\mu)(1 - \frac{\mu^{\gamma+1}}{2}) + E(\mu)\mu^\gamma - \delta^2 \tag{4.44}$$

The first derivative of $G(\mu)$ is given by:

$$G'(\mu) = 2E''(\mu)(1 - \frac{\mu^{\gamma+1}}{2}) + \gamma\mu^{\gamma-1}R_{TV}(f(\mu)) \tag{4.45}$$

If γ is large and negative, and μ large enough, $G'(\mu) = 2E''(\mu)$, and the exact Morozov principle is recovered. We know that $E''(\mu) \leq 0$ and that $E'(\mu)$ is decreasing. It follows from (4.45), that for $\gamma = -1$, the function G is strictly decreasing. For $\gamma < -1$ and $\mu > 2^{1/(\gamma+1)}$, $G'(\mu) < 0$ and the function G is also strictly decreasing. □

This result implies that, if it exists, the solution to $G(\mu) = 0$ that solves the damped Morozov principle is unique.

4.4 Unbiased Predictive Risk Estimator method

In this section, we first briefly summarize the Unbiased Predictive Risk Estimator (UPRE) method for the TV regularization that will be used for comparison with our iterative methods. The UPRE approach has been studied in detail for optimal parameter selection for Tikhonov problems [Vogel (2002),Blu and Luisier (2007),Eldar (2009),Ramani *et al.* (2008),Vaiter *et al.* (2013)]. The predictive error for the parameter μ is defined as $p(\mu) = Af(\mu) - Af^*$. In the framework of the UPRE method, the optimal parameter μ is the minimizer of the predictive risk $\frac{\|p(\mu)\|^2}{N^2}$, where N^2 is the total number of pixels in the image. Recently, the UPRE method has been extended to TV regularization and to large-scale problems [Lin *et al.* (2010)]. As detailed in [Lin *et al.* (2010)], the optimal parameter is the minimizer of the Unbiased Predictive Risk Estimator which has the same functional form as the one for the Tikhonov regularization:

Theorem 4.4.1. *The Unbiased Predictive Risk Estimator of the predictive risk for TV regularization is given by:*

$$UPRE(\mu) = \frac{\|p(\mu)\|^2}{N^2} + \frac{2\sigma^2}{N^2} tr(C_{TV}(\mu)) - \sigma^2 \tag{4.46}$$

where σ^2 is the noise variance and $tr(.)$ denotes the trace operator. The influence matrix $C_{TV}(\mu)$ in the TV problem can be written as:

$$C_{TV}(\mu) = A(\mu A^t A + L(f(\mu)))^{-1} A^t \tag{4.47}$$

where the matrix $L(f(\mu))$ is given by:

$$L(f(\mu)) = D_x^t diag(\frac{1}{\|grad(f(\mu))\|_2}) D_x + D_y^t diag(\frac{1}{\|grad(f(\mu))\|_2}) D_y \tag{4.48}$$

In order to avoid divergencies in the numerical tests, the norm of the gradient of the image at pixel i is approximated by: $\sqrt{(D_i^x(f))^2 + (D_i^y(f))^2 + \epsilon}$ where ϵ is a smoothing constant.

For large scale problems the Singular Value Decomposition of A is not available and it is necessary to approximate the trace value $tr(C_{TV}(\mu))$ with an algorithm requiring only matrix-vector products. With the approach of Hutchinson [Hutchinson (1990)], the trace of a smooth function $F(M)$ of a symmetric positive definite matrix M can be evaluatued with the unbiased trace estimator: $E(u^t F(M) u) = tr(F(M))$ where u is white noise vector with standard deviation equal to $\sigma_u = 1$ and E denotes the expected value function. The choice of u that minimizes the variance in this estimator is the one for which the components of the vector are independant and take on the values of 1 and -1 with equal probability [Vogel (2002)]. The expectation value is evaluated with a number n_u of the random variable realization. In order to approximate the trace of $C_{TV}(\mu)$, we have to solve the linear system: $(\mu A^t A + L(f(\mu)))^{-1} A^t u = y$ for a given vector y which can be done with a conjugate gradient algorithm. In this work, in order to obtain the best reconstruction results, the $UPRE(N_{iter}, \mu)$ was calculated as a function of the number of iterates N_{iter} and as a function of the regularization parameter μ.

4.5 Numerical experiments

In order to show the effectiveness of our method for choosing the regularization parameter, we have considered two test problems: deconvolution and super-resolution. In the deconvolution case, the test image is blurred with a Gaussian kernel of standard deviation σ_{blur} and corrupted by additive Gaussian noise of standard deviation σ. In the super-resolution case, after the blur and the noise are applied, the image is also undersampled by a factor p, increasing the ill-posedness of the problem.
We start by finding the optimal regularization parameter that maximizes the PSNR of the

resulting images defined as in (2.29). Thus, an extensive sweeping of the regularization parameter values is performed. The deteriorated image is restored with the ADMM algorithm for each value of the regularization parameter μ. The ADMM iterations are stopped when $\frac{\|f^{k+1}-f^k\|_2}{\|f^k\|_2} < stop_{ADMM}$, where $stop_{ADMM}$ is a small positive constant.

In order to apply the classical and damped Morozov schemes described in section 4.3, we need to determine approximate values of the parameters a and b of the model function $E'(\mu)$, by first choosing two values μ_* and μ_{**} with $\mu_* < \mu_{**}$. For each of the regularization parameters, μ_* and μ_{**}, the blurred noisy image is restored with the ADMM algorithm and the values $E'(\mu_*)$ and $E'(\mu_{**})$ are calculated. If $2E'(\mu_*) \geq \delta^2$, μ_* is not changed, otherwise it is decreased. If $2E'(\mu_{**}) \leq \delta^2$, μ_{**} is not changed, otherwise it is increased. An approximate value for the regularization parameter, μ_{approx}, is obtained from the equation $\delta^2 = 2(a(\mu_{approx})^{-2} + b)$, where the noise level δ is evaluated with the standard deviation σ as $\delta^2 = N^2\sigma^2$. Starting from this approximate solution, the Newton method is applied to refine it. Considering $\mu_0 = \mu_{approx} + 0.1$ and $\mu_1 = \mu_{approx}$, the iterative formula given by (4.40) is applied for the classical Morozov principle while (4.43) for the damped one. For each iteration of the Newton method, the ADMM algorithm is applied to obtain the solution $f(\mu)$ with the same value $stop_{ADMM}$. The Newton iterations are stopped when $|\frac{\|Af(\mu_k)-g^\delta\|^2-\delta^2}{\delta^2}| < stop_{Newton}$.

4.6 Results and discussion

4.6.1 Deconvolution problem

The test image $f \in \mathbb{R}^{N^2}$ (N=330) to be reconstructed is displayed in Figure 4.1.(a). It is a slice of a bone synchrotron micro-CT sample at a voxel size of 20 μm [Salomé *et al.* (1999)].

We first consider the application of the methods to the noisy and blurred image shown in Figure 4.1.(b) where $\sigma_{blur} = 1.2$ and $\sigma = 4.3$. The noise level δ is evaluated as $\delta^2 = N^2\sigma^2 = 2 \cdot 10^6$. The noisy blurred image has a PSNR=24.89. The evolution of the PSNR of the image restored with the ADMM algorithm as a function of μ is displayed in Figure 4.2.(b). From this curve, the optimal value of the regularization parameter is $\mu_{OPT} = 0.7$ and the optimal PSNR of the reconstructed image is $PSNR(\mu_{OPT}) = 32.32$. A value $stop_{ADMM} = 5{\cdot}10^{-5}$ was considered to ensure the convergence of the regularization method.

We applied the Morozov principles to select the regularization parameter as described in section 4.5. With $\mu_* = 0.1$ and $\mu_{**} = 10$, the values obtained with (4.37) for a and b are $5.36 \cdot 10^3$ and $7.26 \cdot 10^5$, respectively. The approximate value for the regularization parameter was found to be μ_{approx}=0.14. By applying the Newton scheme for the classical Morozov principle, we observed that the convergence was fast and only four iterations were necessary. A value $stop_{Newton} = 0.001$ was considered. The final value of the regularization parameter was found to be $\mu_M = 0.34$. The final image obtained with μ_M is displayed

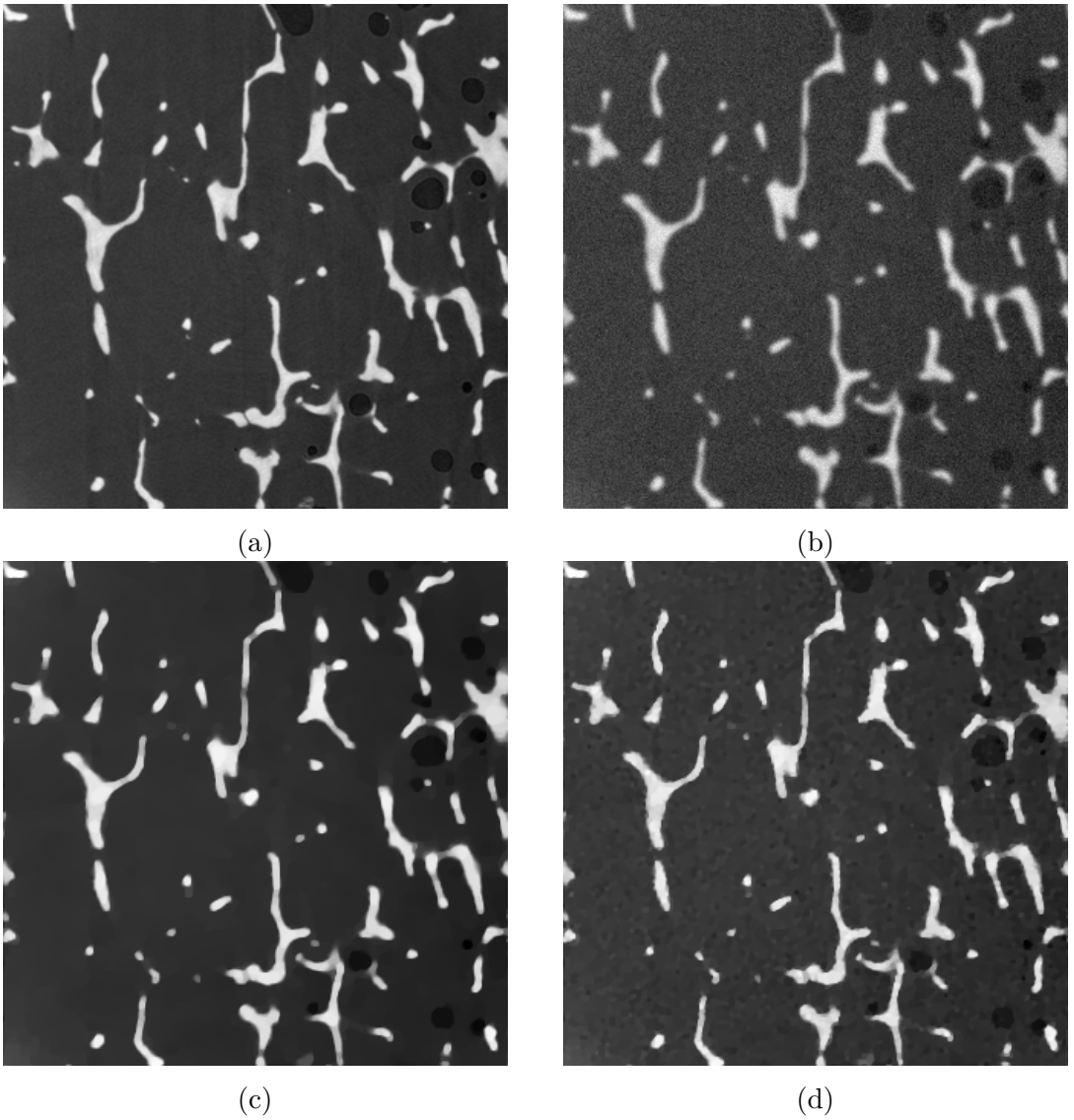

(a) (b)

(c) (d)

Figure 4.1: (a). Ground truth - Bone image; (b). Blurred and noisy image ($\sigma = 4.3$, $\sigma_{blur} = 1.2$.); (c). Restored image with μ_M; (d). Restored image with μ_{UPRE}.

in Figure 4.1.(c). Its PSNR value is $PSNR(\mu_M) = 31.71$ and it is close to the optimal value $PSNR(\mu_{OPT}) = 32.32$. The Figure 4.2.(a) displays the evolution of the data term $\|Af(\mu) - g^\delta\|^2$ as a function of the regularization parameter μ. The model function, the noise level and the iterates μ_k have been reported in the same Figure.

The damped Morozov method with $\gamma = -1$, was then applied by following the same scheme. A value $\mu_{DM} = 1.64$ was obtained after six Newton iterations (Figure 4.2.(c)), with a PSNR value equal to 31.43.

To compare, the UPRE method was also implemented for selecting the regularization parameter. The trace of the influence matrix was calculated with 50 white noise vectors u. The smallest ϵ value that gives a positive UPRE curve was chosen. The UPRE curves are rather noisy thus the mean and the standard deviation of μ and PSNR where estimated

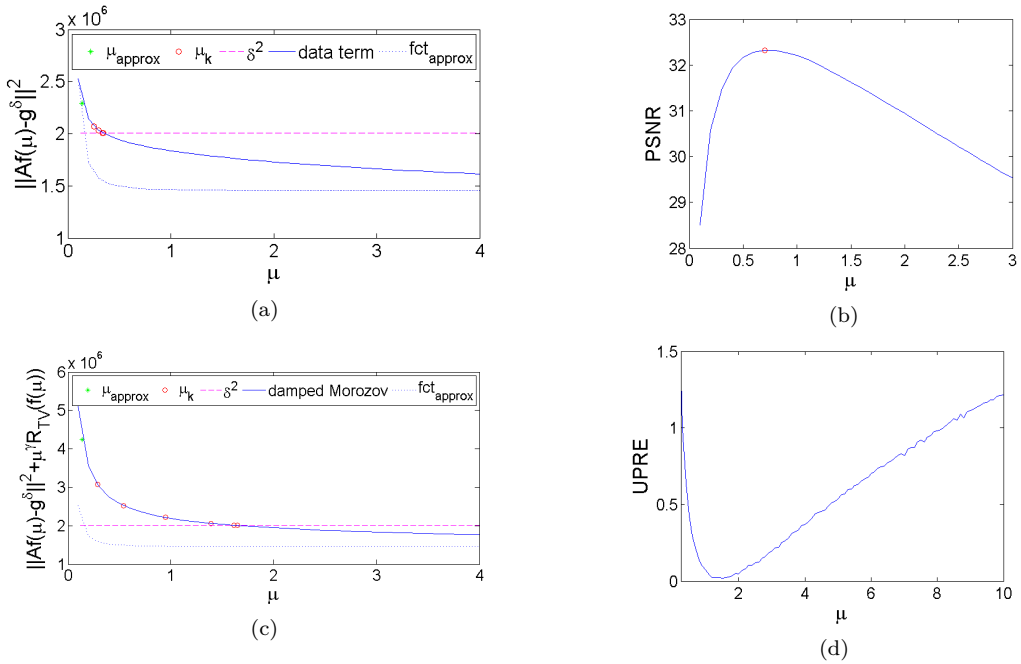

Figure 4.2: Deconvolution applied to the bone image for $\sigma = 4.3$ and $\sigma_{blur} = 1.2$: (a). The evolution of the data term for the classical Morozov method; (c). The evolution of the modified data term for the damped Morozov method; (b). and (d). The evolution of PSNR and UPRE as functions of the regularization parameter μ.

from five UPRE curves for the chosen ϵ. The evolution of the UPRE(μ) for the value of the smoothing parameter $\epsilon = 0.05$ as a function of the regularization parameter is displayed in Figure 4.2.(d) for $stop_{ADMM} = 5 \cdot 10^{-5}$. The UPRE($N_{iter}, \mu$) was also calculated as a function of the number of ADMM iterations, N_{iter}, for different μ values. Figure 4.3 shows the evolution of UPRE as a function of N_{iter} and μ.

The best mean regularization parameter obtained is $\mu_{UPRE} = 1.44$ with a PSNR=31.73 and the image obtained is displayed in Figure 4.1.(d).

In order to have a more extensive comparison of the regularization parameter selection methods, we have tested several noise and blur levels. The values of μ_M, μ_{DM} with $\gamma = -1$, μ_{UPRE}, μ_{OPT} and the PSNR values are summarized in Table 4.1. For low blur, the classical Morozov principle is better than the damped one. On the contrary, for high blur level, the damped Morozov principle improves the results obtained with the classical Morozov principle. The UPRE method is efficient except for the highest noise level case.

4.6.2 Super-resolution problem

In this section we investigate a more ill-posed problem, the super-resolution problem. The standard deviation of the Gaussian blurring kernel was $\sigma_{blur} = 4.85$ and a sub-sampling rate of $p = 4$ was applied to the images. An additional Gaussian noise with a standard deviation σ was added to the low-resolution image. The aim of the regularization approach is to estimate the high resolution image.

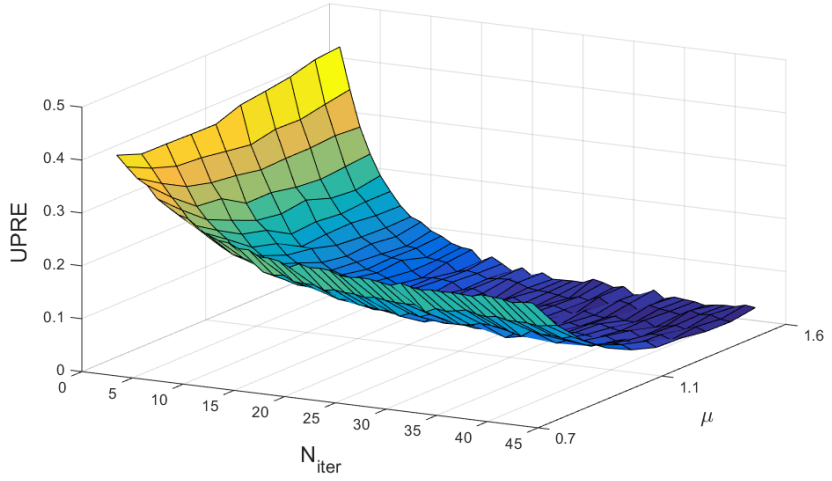

Figure 4.3: Evolution of UPRE as a function of N_{iter} and μ for deconvolution case, $\sigma = 4.3$, $\sigma_{blur} = 1.2$ - Bone image.

	$\sigma = 4.3, \sigma_{blur} = 1.2$		$\sigma = 6, \sigma_{blur} = 1.2$		$\sigma = 4.3, \sigma_{blur} = 3.6$	
Method	μ	PSNR	μ	PSNR	μ	PSNR
classical Morozov	0.34	**31.71**	0.24	**30.65**	0.95	23.52
damped Morozov	1.64	31.43	0.97	30.47	5.12	**24.61**
UPRE(μ)	1.46	31.66 ± 0.11	1.02	30.36 ± 0.08	5.64	24.58 ± 0.02
UPRE(N_{iter}, μ)	1.44	**31.73 ± 0.08**	0.99	30.42 ± 0.06	5.66	24.59 ± 0.02
optimal	0.70	**32.32**	0.46	**31.32**	4.71	**24.61**

Table 4.1: Comparison of regularization parameter selection methods for deconvolution case - Bone image.

Simulations were performed with several noise levels. To illustrate the method, we first detail the results obtained with $\sigma = 6$. Figure 4.4.(a) and 4.4.(b) display the high resolution and low resolution images. Figure 4.5.(b) displays the evolution of the PSNR for $\sigma = 6$. The best PSNR is 19.57. In this case, the optimal regularization parameter is $\mu_{OPT} = 6.2$. The regularization parameter estimated with the classical Morozov principle is $\mu_M = 2.22$, yielding a PSNR of 19.07, far from the optimal value. The evolution of the data term for this case is displayed in Figure 4.5.(a).

When applying the damped Morozov method with $\gamma = -1$, the obtained regularization parameter is $\mu_{DM} = 6.2$. The evolution of the data term weighted with the TV norm of the image f is shown in Figure 4.5.(c) as a function of the regularization parameter. The corresponding PSNR value is 19.57 which is very close to the optimal one. We obtain thus a very good estimation of the optimal regularization parameter.

To compare, the evolution of the UPRE(μ) term for $\sigma = 6$ with $\epsilon = 0.05$ is displayed in Figure 4.5.(d). The regularization parameter obtained is $\mu_{UPRE} = 13.48$ with a PSNR of

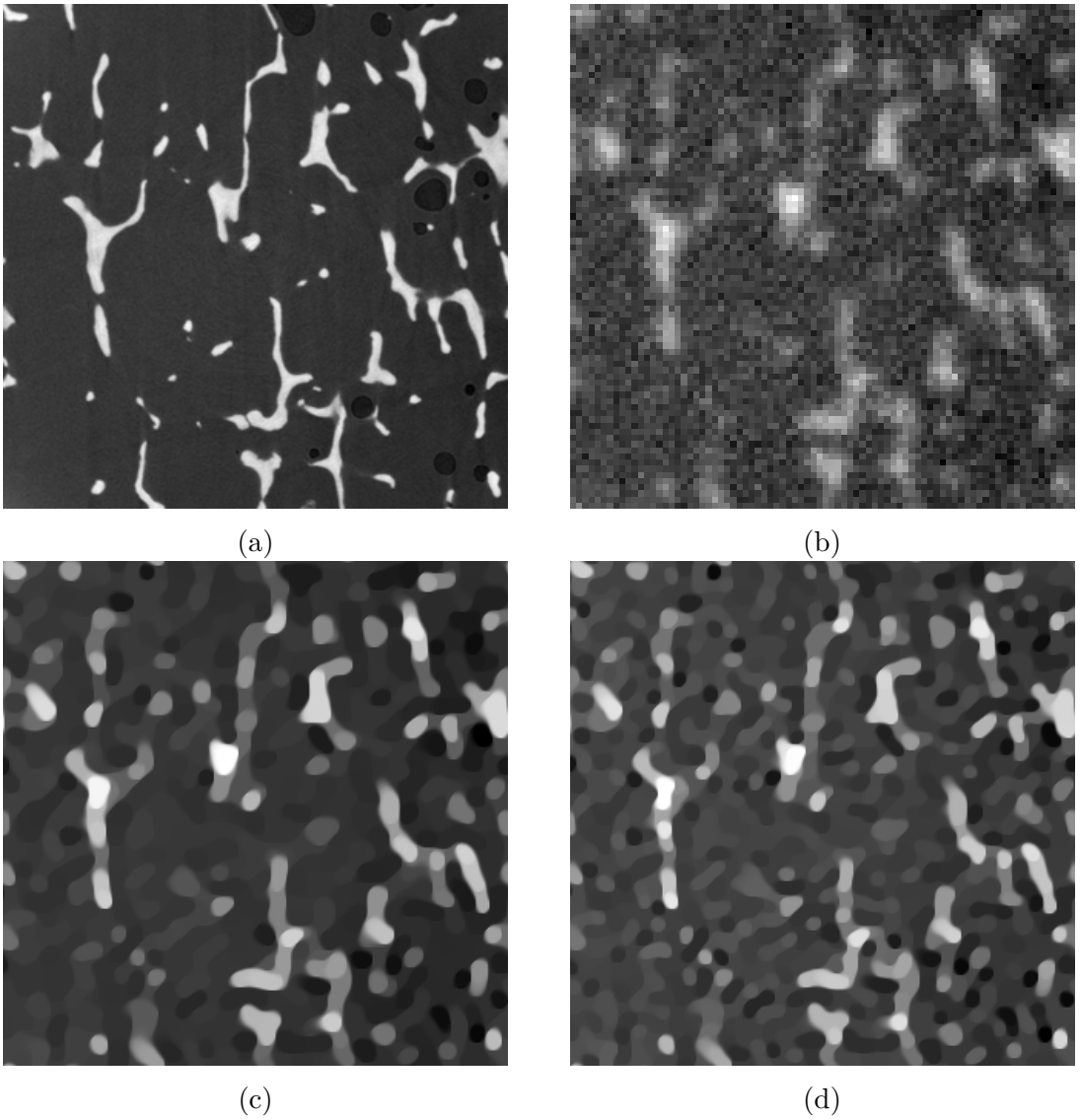

Figure 4.4: (a). Ground truth - Bone image; (b). Low resolution blurred and noisy image ($p = 4$, $\sigma = 6$, $\sigma_{blur} = 4.85$); (c). Restored image with μ_{DM}; (d). Restored image with μ_{UPRE}.

19.14, slightly lower than with the damped Morozov method. The images obtained with this two methods are displayed in Figures 4.4.(c)-(d).

Table 4.2 summarizes the values of the regularization parameters and the PSNR obtained for different noise levels. For all these noise levels, the UPRE method gives a better estimation of the optimal regularization parameter than the classical Morozov method. Yet, the damped Morozov method is more effective than the UPRE approach for this super-resolution problem.

Super-resolution test problem for other images

To assess the potential of the proposed method in other domains of application, we

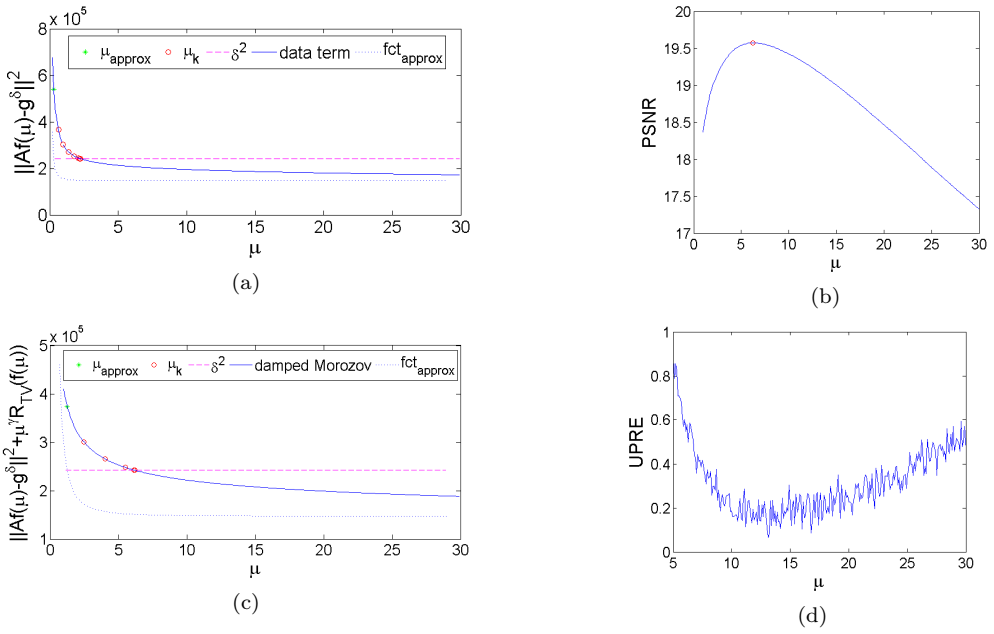

Figure 4.5: Super-resolution applied to the bone image for $p = 4$, $\sigma = 6$ and $\sigma_{blur} = 4.85$: (a). The evolution of the data term for the classical Morozov method; (c). The evolution of the modified data term for the damped Morozov method; (b). and (d). The evolution of PSNR and UPRE as function of the regularization parameter μ.

	$\sigma = 1$		$\sigma = 4.3$		$\sigma = 6$	
Method	μ	PSNR	μ	PSNR	μ	PSNR
classical Morozov	25.43	21.38	3.45	19.49	2.22	19.07
damped Morozov	141.5	**22.28**	10.94	**20.06**	6.2	**19.57**
UPRE(μ)	198.4	22.25 $\pm$ 0.01	18.26	19.93 $\pm$ 0.01	13.2	19.17 $\pm$ 0.07
UPRE(N_{iter}, μ)	199.6	22.25 $\pm$ 0.005	18.36	19.92 $\pm$ 0.02	13.48	19.14 $\pm$ 0.09
optimal	158.7	**22.28**	11.5	**20.06**	6.2	**19.57**

Table 4.2: Comparison of regularization parameter selection methods for super-resolution case - Bone image.

made additional experiments on the usual Cameraman (N=512) and Lena (N=512) images. The simulation parameters of the super-resolution problem where: p=4, $\sigma_{blur} = 4.85$ and two noise levels $\sigma = 4.3$ and $\sigma = 6$.

The results are summarized in Table 4.3 and Table 4.4. Resulting images are displayed in Figures 4.6 - 4.9. In most cases, the UPRE method provides better results than the classical Morozov method. Yet, the damped Morozov method leads to a more accurate estimation of the optimal regularization parameter. It should be emphasized that the methods developed with the classical and damped Morozov principles are very fast and do not rely on an extensive sweeping of the regularization parameter values.

	$\sigma = 4.3$		$\sigma = 6$	
Method	μ	PSNR	μ	PSNR
classical Morozov	3.15	23.74	1.95	23.38
damped Morozov	13.34	**24.11**	7.58	**23.72**
UPRE(μ)	19.91	23.99 $\pm$ 0.05	12.24	23.50 $\pm$ 0.06
UPRE(N_{iter}, μ)	18.94	24.01 $\pm$ 0.04	10.91	23.58 $\pm$ 0.06
optimal	10.97	**24.14**	5.83	**23.74**

Table 4.3: Comparison of regularization parameter selection methods for super-resolution case - Cameraman image.

	$\sigma = 4.3$		$\sigma = 6$	
Method	μ	PSNR	μ	PSNR
classical Morozov	2.48	23.51	1.73	23.23
damped Morozov	13.11	**23.77**	7.89	**23.42**
UPRE(μ)	17.55	23.63 $\pm$ 0.03	11.33	23.17 $\pm$ 0.18
UPRE(N_{iter}, μ)	17.19	23.65 $\pm$ 0.04	11.34	23.18 $\pm$ 0.15
optimal	8.85	**23.83**	4.63	**23.53**

Table 4.4: Comparison of regularization parameter selection methods for super-resolution case - Lena image.

4.7 Conclusions

In this chapter, we have proposed new iterative methods to determine the optimal regularization parameter in linear inverse problems with TV regularization. For a given regularization parameter, the TV regularization functional is minimized with the classical ADMM algorithm. Our approach is based on the classical Morozov principle or on a damped version of this principle. The convergence properties of the regularization method for this choice of the regularization parameter have been demonstrated. Based on the regularity properties of the Augmented Lagrangian value function, it was shown that the data term can be approximated by a simple model function. This model function for the data term of the regularization functional is first obtained from the reconstructed images with two different regularization parameters. An approximate value of the regularization parameter is calculated with the model function approximating the discrepancy term. Then the solution is refined with a Newton iterative method on the basis of the Morozov principle or its damped version. This new approach has been compared with the one based on the UPRE, for deconvolution and super-resolution test problems, in the case of various noise and blur levels and for different images.

In the deconvolution case, the damped Morozov principle is the most efficient method for the highest blur level. Otherwise, the classical Morozov principle offers the best esti-

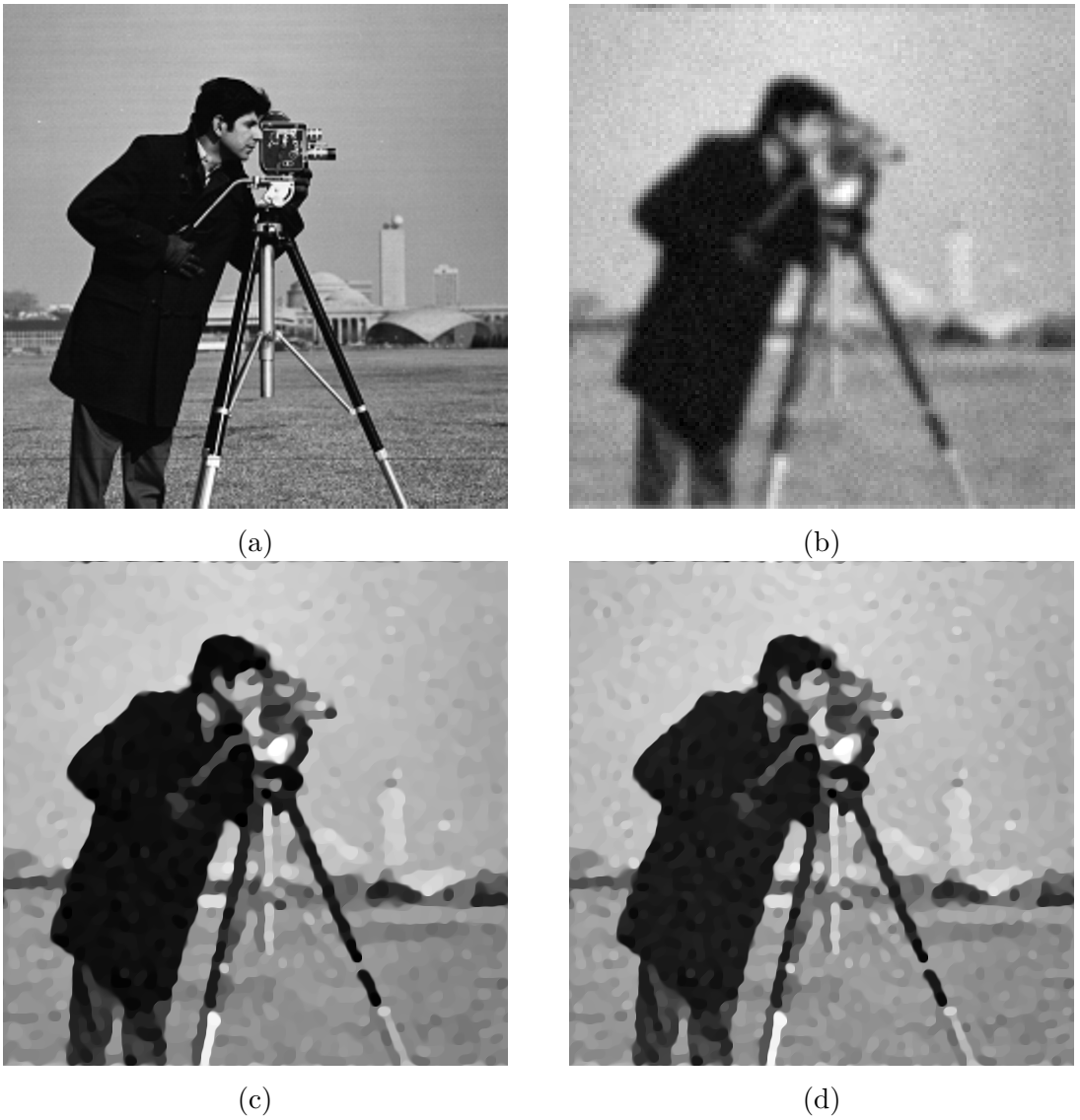

Figure 4.6: (a). Ground truth - Cameraman image; (b). Low resolution blurred and noisy image ($p = 4, \sigma_{blur} = 4.85, \sigma = 4.3$); (c). Restored image with μ_{DM}; (d). Restored image with μ_{UPRE}.

mation of the optimal regularization parameter. For the super-resolution case, the UPRE method outperforms the classical Morozov method. Yet, a more accurate estimation of the optimal regularization parameter is obtained with the damped Morozov principle, where the data term is weighted by a TV term. The iterative schemes based on the new model function presented in this work are very fast and avoid an extensive sweeping of the regularization parameter values.

(a) (b) (c) (d)

Figure 4.7: (a). Ground truth - Cameraman image; (b). Low resolution blurred and noisy image ($p = 4, \sigma_{blur} = 4.85, \sigma = 6$); (c). Restored image with μ_{DM}; (d). Restored image with μ_{UPRE}.

Figure 4.8: (a). Ground truth - Lena image; (b). Low resolution blurred and noisy image ($p = 4, \sigma_{blur} = 4.85, \sigma = 4.3$); (c). Restored image with μ_{DM}; (d). Restored image with μ_{UPRE}.

(a) (b)

(c) (d)

Figure 4.9: (a). Ground truth - Lena image; (b). Low resolution blurred and noisy image ($p = 4, \sigma_{blur} = 4.85, \sigma = 6$); (c). Restored image with μ_{DM}; (d). Restored image with μ_{UPRE}.

Chapter 5

Joint Super-Resolution/Segmentation

In chapter 3 we have seen that super-resolution methods followed by simple thresholding are improving the bone quantitative analysis. As the trabecular bone images are presenting quasi-binary structure and in the end we are interested in the segmentation of it, we turned our attention to joint super-resolution/segmentation methods to solve our problem in one step.

This chapter is organized as follows. We start by presenting the state of the art of joint restoration/segmentation methods. In the second section we formulate the joint segmentation/super-resolution problem as a linear inverse problem, following the approach of [Paul *et al.* (2013)]. In the next section, we detail how to perform the minimization of the regularization functional using the Alternating Direction Method of Multipliers (ADMM). Then, the validation of the proposed approach is performed on experimental high-resolution micro-CT volumes of bone samples at 20 μm after simulating the effect of a loss of spatial resolution and degradation by noise and blur. Concluding remarks are given in the last section.

The method and the results presented in this chapter have been published in the following article:

A. Toma, L. Denis, B. Sixou, J.B. Pialat, F. Peyrin, "Total variation Super-resolution for 3D trabecular bone micro-structure segmentation", EUSIPCO 2014, Lisbon, Portugal, 1-5 September 2014, pp 2220 - 2224

5.1 State of the art

Image segmentation has been widely studied in the literature, see for example [Chan and Shen (2005), Chan *et al.* (2001), Cremers *et al.* (2006), Goldstein *et al.* (2010)]. Image super-resolution is also an active research field [Babacan *et al.* (2008)b, Ren *et al.* (2013)]. Yet, in most studies, image restoration (denoising, deblurring, super-resolution) and image segmentation are considered separately. Recent work on convex relaxation of segmentation problems have proved that some segmentation models could be exactly computed by resorting to techniques similar to total variation denoising methods [Chan *et al.* (2006), Goldstein *et al.* (2010)]. This bridges the gap between the families of segmentation methods and restoration methods and offers attractive theoretical guarantees of global minimization, thus segmentation results that are independent from the initialization. By generalizing these segmentation methods to linear degradations such as blur, it is possible to perform joint restoration and segmentation, as shown in a very recent work [Paul *et al.* (2013)].

Since the images we are interested in display quasi-binary structures, we can strongly rely on a total variation (TV) prior model and consider single-image super-resolution. We compare segmentation of a grayscale volume obtained by a TV regularized super-resolution method with joint segmentation / super-resolution on 3D volumes simulated from a ground-truth segmentation obtained with high-resolution micro-CT.

In a two-phase segmentation task, each voxel of the segmented image s is assigned to one of the two phases. Let c_0 and c_1 be the average graylevels of each phase. A satisfying segmentation of image f is a labelling such that each voxel is assigned to a phase whose average graylevel is close to the corresponding graylevel of image $\boldsymbol{f}$ and where neighbor voxels most often belong to the same class. One can thus consider the following functional first proposed by [Mumford and Shah (1989)]:

$$\int_{\mathscr{R}_0} [f(\boldsymbol{r}) - c_0]^2 \, \mathrm{d}\boldsymbol{r} + \int_{\mathscr{R}_1} [f(\boldsymbol{r}) - c_1]^2 \, \mathrm{d}\boldsymbol{r} + \nu|\Gamma| \tag{5.1}$$

where $\mathscr{R}_0$ and $\mathscr{R}_1$ are the regions of each of the two phases and $|\Gamma|$ denotes the perimeter of the boundary between regions $\mathscr{R}_0$ and $\mathscr{R}_1$.

5.2 Joint Super-Resolution/Segmentation

5.2.1 Convex formulation

In discrete form, minimizing the cost function (5.1) corresponds to the following minimization problem:

$$\arg\min_{\boldsymbol{s}\in\mathbb{B}} \quad \frac{\mu}{2}\|\boldsymbol{f} - \boldsymbol{s}\|_2^2 + \mathcal{R}_{\mathrm{TV}}(\boldsymbol{s}) \tag{5.2}$$

where $\mathbb{B} = \{c_0, c_1\}^{N'}$ is the set of all N'-voxels two-phase volumes and $\mu = 2|c_1 - c_0|/\nu$.

In order to perform joint super-resolution and segmentation, we consider the following

optimization problem:

$$\arg\min_{\boldsymbol{s}\in\mathbb{B}} \ \frac{\mu}{2}\left\|\boldsymbol{A}\boldsymbol{s}-\boldsymbol{g}^{\delta}\right\|_2^2+\mathcal{R}_{\mathrm{TV}}(\boldsymbol{s})\,. \tag{5.3}$$

Minimization problem (5.3) is NP-hard for general linear operators $\boldsymbol{A}$. We therefore only perform approximate minimization by considering instead the following convex relaxation:

$$\hat{\boldsymbol{s}}\in\ \arg\min_{\boldsymbol{s}\in[c_0,c_1]^{N'}} \ \frac{\mu}{2}\left\|\boldsymbol{A}\boldsymbol{s}-\boldsymbol{g}^{\delta}\right\|_2^2+\mathcal{R}_{\mathrm{TV}}(\boldsymbol{s})\,, \tag{5.4}$$

where the set of two-phase volumes has been replaced by the convex set of graylevel volumes with graylevels in the range $[c_0, c_1]$.

5.2.2 The Alternating Direction Method of Multipliers

Restoration of a high-resolution image $\hat{\boldsymbol{s}}$ from a single low-resolution image requires solving an optimization problem of the form of equation (5.4). By introducing auxiliary variables, the minimization problem can be re-expressed as:

$$\begin{aligned}\hat{\boldsymbol{s}}\in \ \arg\min_{\boldsymbol{s},\,\{\boldsymbol{h}_i\},\,\boldsymbol{l}\in[c_0,c_1]^{N'}} \ & \frac{\mu}{2}\left\|\boldsymbol{A}\boldsymbol{s}-\boldsymbol{g}^{\delta}\right\|_2^2+\sum_i\|\boldsymbol{h}_i\|\,, \\ \text{s.t.}\quad & \forall i,\ \boldsymbol{h}_i=\boldsymbol{D}_i\,\boldsymbol{s},\ \text{ and }\ \boldsymbol{l}=\boldsymbol{s}.\end{aligned} \tag{5.5}$$

The optimization problem (5.5) can be solved efficiently by finding the saddle point of the augmented Lagrangian using the alternating direction method of multipliers (ADMM), following the approach presented in chapter 3. The augmented Lagrangian associated to constrained problem (5.5) writes:

$$\begin{aligned}\mathcal{L}_{\mathrm{A}}(\boldsymbol{s},\{\boldsymbol{h}_i\},\boldsymbol{l},\{\boldsymbol{\lambda}_i\},\boldsymbol{\lambda_C}) = \ & \frac{\mu}{2}\left\|\boldsymbol{A}\boldsymbol{s}-\boldsymbol{g}^{\delta}\right\|_2^2+\sum_i\|\boldsymbol{h}_i\| \\ & +\sum_i\left[\frac{\beta}{2}\|\boldsymbol{h}_i-\boldsymbol{D}_i\,\boldsymbol{s}\|^2-\boldsymbol{\lambda}_i^{\mathrm{t}}(\boldsymbol{h}_i-\boldsymbol{D}_i\,\boldsymbol{s})\right] \\ & +\boldsymbol{I_C}(\boldsymbol{l})+\frac{\beta}{2}\|\boldsymbol{l}-\boldsymbol{s}\|_2^2-\boldsymbol{\lambda}_{\boldsymbol{C}}^{t}(\boldsymbol{l}-\boldsymbol{s})\end{aligned} \tag{5.6}$$

with $\boldsymbol{\lambda}_i$ the Lagrange multipliers for the i^{th} equality constraint, $\boldsymbol{\lambda_C}$ the Lagrange multiplier for convex constraint and $\boldsymbol{I_C}(\boldsymbol{l})$ is the indicator function of the convex set $\mathrm{C}=[c_0,c_1]^{N'}$.

In this case we have to minimize the augmented Lagrangian $\mathcal{L}_{\mathrm{A}}(\boldsymbol{s},\{\boldsymbol{h}_i\},\boldsymbol{l},\{\boldsymbol{\lambda}_i\},\boldsymbol{\lambda_C})$ with respect to each of the 5 unknowns. We explain below how each minimization is made and after that a compact scheme of the ADMM TVbox method is presented.

The ADMM method alternates between five updates:

1. Update of the high-resolution reconstruction $\boldsymbol{s}$,

by (approximately) solving the linear system:

$$\boldsymbol{H}\boldsymbol{s}^{k+1} = \mu \boldsymbol{A}^{\mathrm{t}}\boldsymbol{g}^{\delta} + \sum_i \boldsymbol{D}_i^{\mathrm{t}}(\beta \boldsymbol{h}_i^k - \boldsymbol{\lambda}_i^k) + \beta \boldsymbol{l}^k - \boldsymbol{\lambda_C}^k \,,$$

with $\boldsymbol{H} = \mu \boldsymbol{A}^{\mathrm{t}}\boldsymbol{A} + \beta \boldsymbol{I} + \sum_i \beta \boldsymbol{D}_i^{\mathrm{t}}\boldsymbol{D}_i$.

2. Update of the auxiliary variables $\boldsymbol{h}_i$,
   by applying a soft-thresholding operator $\mathcal{S}_\beta$:

$$\boldsymbol{h}_i^{k+1} = \mathcal{S}_\beta \left(\boldsymbol{D}_i \boldsymbol{s}^{k+1} + \boldsymbol{\lambda}_i^k / \beta \right) ,$$

   with $\mathcal{S}_\beta(\boldsymbol{u}) = \max\left(1 - \frac{1}{\beta \|\boldsymbol{u}\|}, 0\right) \cdot \boldsymbol{u}$.

3. Update of the auxiliary variable $\boldsymbol{l}$:

$$\boldsymbol{l}^{k+1} = \pi_C(\boldsymbol{s}^k + \frac{\boldsymbol{\lambda}_C^k}{\beta}) \,,$$

   where π_C is the projection on the convex set C.

4. Update of the Lagrange multipliers $\boldsymbol{\lambda}_i$:

$$\boldsymbol{\lambda}_i^{k+1} = \boldsymbol{\lambda}_i^k - \beta \left(\boldsymbol{h}_i^{k+1} - \boldsymbol{D}_i \boldsymbol{s}^{k+1} \right) .$$

5. Update of the Lagrange multiplier $\boldsymbol{\lambda_C}$:

$$\boldsymbol{\lambda}_{\boldsymbol{C}}^{k+1} = \boldsymbol{\lambda}_{\boldsymbol{C}}^k - \beta \left(\boldsymbol{l}^{k+1} - \boldsymbol{s}^{k+1} \right) .$$

More details about how the updates were obtained can be found in the Appendix D.
For comparison purposes, we will also consider in the next part the 3D TV super-resolution without the box constraints that was detailed in chapter 3 for the 2D case. This appears as a special case of the algorithm just described.

5.3 Numerical experiments

We applied the two total variation based regularizations and the bicubic interpolation method to experimental data. Human bone samples (cylinder core of 10mm) were scanned with parallel-beam synchrotron micro-CT at 10 μm. To this aim, 1500 2D projections were acquired after rotating the sample. The 3D images were reconstructed using the Filtered back projection algorithm [Salomé *et al.* (1999)] and further resampled at 20 μm. Due to the high signal to noise ratio of synchrotron CT images, the binary volume of the bone structure was obtained by simple thresholding with the Otsu's method. This binary image of size $328 \times 328 \times 328$ is considered as the ground truth and is shown in Fig. 5.1. The low resolution volumes were obtained considering a sub-sampling rate of $p = 2$. For the blurring operation, we have used a Gaussian point spread function of standard deviation

$\sigma_{blur} = 2.425$. We tested two additive Gaussian noise levels with standard deviations $\sigma = 0.01$ and $\sigma = 0.1$.

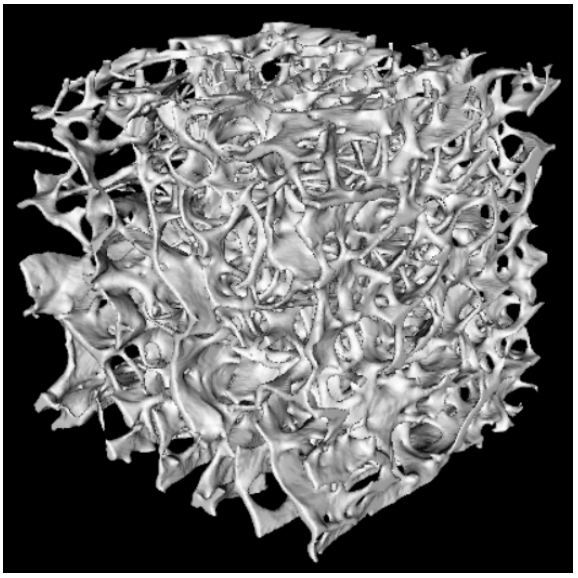

Figure 5.1: The reference binary volume.

To ensure the convergence of the regularization methods, we considered the following stopping criteria of the ADMM iterations: $\frac{\|f^{k-1}-f^k\|_2}{\|f^k\|_2} < \epsilon$ with $\epsilon = 10^{-4}$ for the noise level $\sigma = 0.01$ and $\epsilon = 5 \cdot 10^{-4}$ for $\sigma = 0.1$. A high resolution volume was obtained from the low-resolution, blurred and noisy volume with TV and TV with box constraints regularization. An extensive sweeping of the regularization parameters was performed in order to pick the optimal one based on the known ground-truth. For each method, the regularization parameter μ chosen is the one that maximizes the DICE value between the binary ground truth and the segmented reconstructed volume obtained with the threshold 0.5. For a fixed regularization parameter, the β parameter is chosen beforehand by computing only a limited number of iterations and in order to have the fastest decrease of the regularization functional. For comparison reasons, the low resolution volume and the bicubic interpolation volume were segmented with Otsu's method, for both noise levels. The performance of the methods was measured considering the DICE value and also the quantitative bone micro-architecture parameters such as the bone volume to total volume (BV/TV in %), the trabecular thickness (Tb.Th in μm), the trabecular separation (Tb.Sp in μm), the Euler number (χ), the density of connectivity (Conn.D in mm^{-3}), described in section 1.4.6. Also, the structural model index (SMI) and a local topological analysis were performed determining the distribution of the plate-like elements and rode-like elements given by the parameters: the plates volume to bone volume (PV/BV in %), the rodes volume to bone volume (RV/BV in %) and the nodes volume to bone volume (NV/BV in %).

5.4 Results and discussion

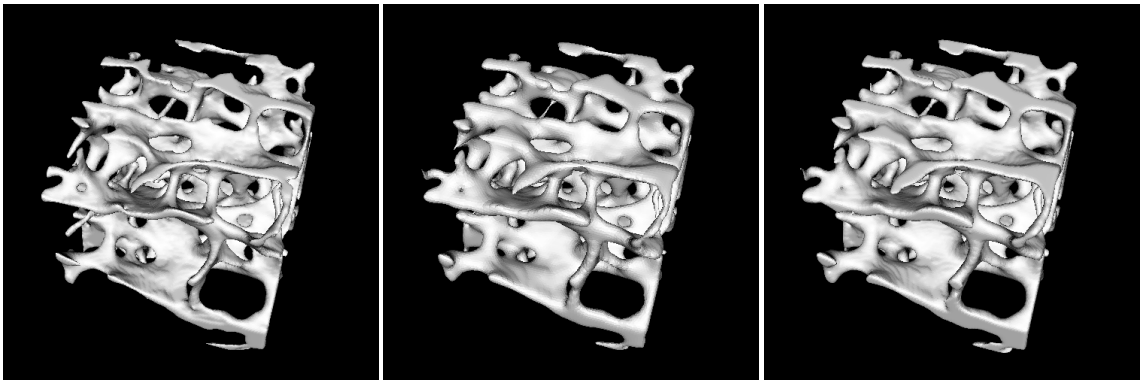

(a) Ground-truth volume (b) Low resolution volume (c) Bicubic interpolation

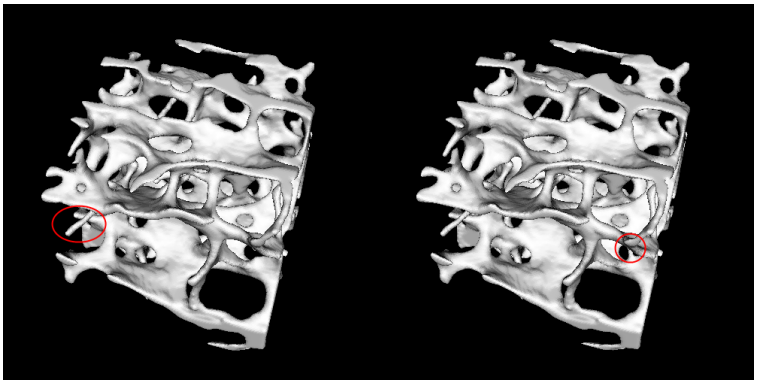

(d) TV regularization (e) TVbox regularization

Figure 5.2: Comparison of 3D restoration methods for the noise level $\sigma = 0.01$.

Parameter	**Reference**	**Low res.**	**Bicubic Interp.**	**TV**	**TVbox**
			$\sigma = 0.01$		
DICE	1	-	0.778	0.962	**0.970**
Euler no.	-1211	-1006	-1006	-1018	**-1106**
Conn.D (mm^{-3})	4.86	3.99	4.01	4.45	**4.52**
BV/TV (%)	11.07	16.86	16.76	11.23	**11.14**
Tb.Th (μm)	134	204	199	**136**	**136**
Tb.Sp (μm)	757	694	697	**762**	**762**
SMI	1.66	2.12	1.98	1.72	**1.69**
PV/BV (%)	75.85	52.81	62.86	**75.61**	75.22
RV/BV (%)	23.59	45.38	36.85	**24.00**	24.40
NV/BV (%)	0.56	1.80	0.29	0.38	0.38

Table 5.1: Quantitative parameters for the noise level $\sigma = 0.01$

Crops of size $150 \times 150 \times 150$ of the resulted binary volumes are shown in Figure 5.2 for

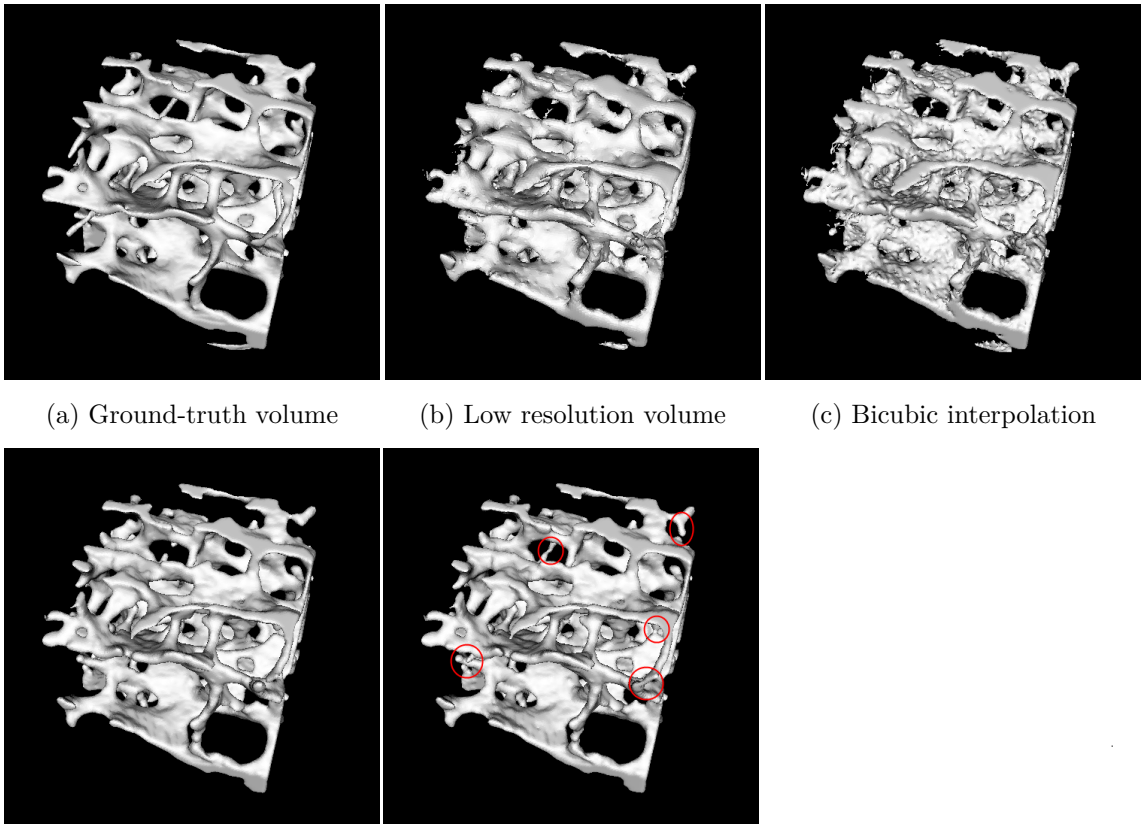

(a) Ground-truth volume (b) Low resolution volume (c) Bicubic interpolation

(d) TV regularization (e) TVbox regularization

Figure 5.3: Comparison of 3D restoration methods for the noise level $\sigma = 0.1$.

the noise level $\sigma = 0.01$ and in Figure 5.3 for $\sigma = 0.1$. From these images we can visually estimate that the TV based methods are better recovering the bone structure and that TVbox method is the preferred method for solving our problem. The same conclusion can be taken from Figure 5.4 that shows a slice of the ground-truth volume, of the low resolution gray level volume and of the resulted binary volumes with the tested method. The quantitative results are summarized in Table 5.1. From this table we can see the efficiency of the TV regularization methods. The TV methods outperforms clearly the interpolation method which gives poor estimates of the structural parameters. The DICE, Euler number, density of connectivity, BV/TV, Tb.Th, SMI, PV/BV and RV/BV are all improved with the TV based regularization approaches. The best reconstruction results and structural parameters are obtained with additional box constraint (TVbox method). The advantages of the TVbox method are more clearly showed in the higher noisy case (see Table 5.2 for $\sigma = 0.1$). The ability of the TVbox method to restore the connectivity, represented by the Conn.D parameter, can also be observed in Figure 5.3. Moreover, the estimation of the plate and rode elements distribution given by the SMI, PV/BV and RV/BV, is the closest to the reference values with the TVbox method.

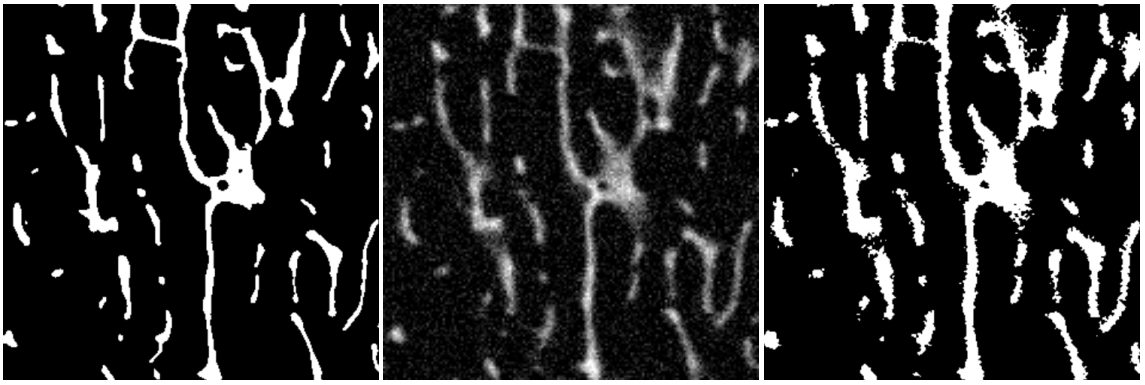

(a) Ground-truth slice (b) Low resolution slice (c) Bicubic interpolation

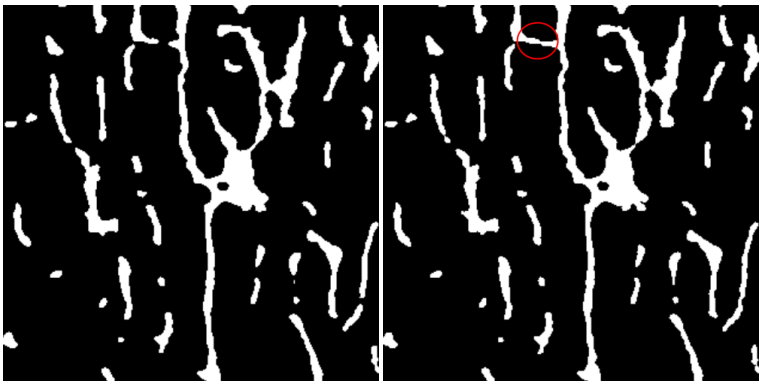

(d) TV regularization (e) TVbox regularization

Figure 5.4: Slice of the restored volumes for the noise level $\sigma = 0.1$.

Parameter	**Reference**	**Low res.**	**Bicubic Interp.**	**TV**	**TVbox**
			$\sigma = 0.1$		
DICE	1	-	0.773	0.898	**0.906**
Euler no.	-1211	4888	11201	-686	**-723**
Conn.D (mm^{-3})	4.86	16.61	11.98	3.92	**4.20**
BV/TV (%)	11.07	16.48	16.38	11.78	**11.52**
Tb.Th (μm)	134	173.6	173	146	**142**
Tb.Sp (μm)	757	742.5	**758**	765	768
SMI	1.66	2.70	2.33	1.90	**1.85**
PV/BV (%)	75.85	25.29	33.03	68.27	**69.12**
RV/BV (%)	23.59	44.35	56.81	31.25	**30.35**
NV/BV (%)	0.56	25.93	9.84	0.48	**0.53**

Table 5.2: Quantitative parameters for the noise level $\sigma = 0.1$

5.5 Conclusions

In this chapter, we proposed a super-resolution segmentation method based on the total variation regularization with convex constraint and ADMM minimization for improving the trabecular bone micro-structure quantification from micro-CT volumes. We compared this new approach with a standard interpolation method and TV super-resolution method on noisy, blurred, low-resolution volumes in terms of DICE and structural parameters. Better results are obtained when a convex constraint is included in the TV regularization functional. We observe that in this case, all quantitative bone parameters are nearly well restored and improved compared to the original.

Chapter 6

Semi-Blind Joint Super-Resolution/Segmentation

6.1 Introduction

In chapter 5 we have shown that an *a priori* based on TV regularization with a convex relaxation of the binary constraint (TVbox) can improve the quantification (and especially the connectivity) of the artificially deteriorated experimental micro-CT bone images when the blur kernel is known.

However, when considering real data, the problem is more complex since the blurring kernel is not known and may be difficult to estimate. Several methods have been proposed for the simultaneous recovery of the image and of the point spread function (PSF), like bayesian methods [Babacan *et al.* (2009), Molina *et al.* (2006)], Tikhonov regularization [You and Kaveh (1996)] or Total Variation (TV) regularization [Babacan *et al.* (2009), Chan and Wong (1998), Liao and Ng (2011)]. Estimating the unknown image and some partially known PSF is referred to as semi-blind deconvolution [Galatsanos *et al.* (2000), Molina (1994)].

Thus, we finally address the problem of semi-blind joint super-resolution/segmentation aiming at estimating both the segmented super-resolved image and the gaussian blurring kernel. Preliminary results on experimental HR-pQCT images are presented.

The method and the results presented in this chapter have been published in the following article:
Peyrin, F., Toma, A., Sixou, B., Denis, L., Burghardt, A., Pialat, J.-B.
"Semi-blind joint super-resolution/segmentation of 3D trabecular bone images by a TV box approach", EUSIPCO 2015, Nice, France, pp. 2811 - 2815

6.2 Semi-Blind Joint Super-Resolution/Segmentation

6.2.1 Problem formulation

In the general case, solving the blind super-resolution problem requires estimating both $\boldsymbol{f}$ and the blurring operator from (3.1). In this first approach, we assume that the blur is isotropic and can be represented by a 3D Gaussian kernel:

$$\alpha(x, y, z) = \alpha_\sigma(x)\alpha_\sigma(y)\alpha_\sigma(z) \tag{6.1}$$

where $\alpha_\sigma(x)$ is the 1D Gaussian kernel of standard deviation σ. The problem in now reformulated as a semi-blind problem:

$$\{\hat{\boldsymbol{f}}, \sigma\} = \arg\min_{\boldsymbol{f},\sigma}\{J(\boldsymbol{f}, \sigma), \boldsymbol{f} \in [c_0, c_1]^{N'}, \sigma > 0\}. \tag{6.2}$$

where $J(\boldsymbol{f}, \sigma)$ includes the dependence of the blurring kernel on σ.

6.2.2 Alternating Minimization algorithm

We note that the cost function is convex with respect to $\boldsymbol{f}$, but not convex with respect to the standard deviation σ. Thus, in order to find the solution $\{\hat{\boldsymbol{f}}, \sigma\}$ that minimizes the cost function (6.2), we apply the alternating minimization scheme:

Step 0: Choose a starting sigma value $\sigma^{(0)}$, t=0

Step 1: t=t+1, Refine the image:

$$\boldsymbol{f}^{(t)} = \arg\min_{\boldsymbol{f}\in[c_0,c_1]^{N'}} \frac{\mu}{2}\left\|\boldsymbol{A}^{(t-1)}\boldsymbol{f} - \boldsymbol{g}^\delta\right\|_2^2 + \|\nabla\boldsymbol{f}\|_1 \tag{6.3}$$

where $\boldsymbol{A}^{(t-1)}$ is the direct operator at the step t-1.

Step 2:

$$\boldsymbol{f}_{01}^{(t)} = \text{threshold}(\boldsymbol{f}^{(t)}) \tag{6.4}$$

Step 3: Refine the blur:

$$\sigma^{(t)} = \arg\min_{\sigma} \left\| \boldsymbol{A}(\sigma)\boldsymbol{f}_{01}^{(t)} - \boldsymbol{g}^{\delta} \right\|_2^2 \tag{6.5}$$

Step 4: Go to step 1 until convergence.

We perform the minimization of (6.3) with the TVbox ADMM scheme presented in chapter 5. At step 3, the Newton method is applied for obtaining the solution $\sigma^{(t)}$. A local optimum is found since the regularization functional is not a convex function of σ.

6.3 Numerical experiments

6.3.1 Experiments on simulated images

We first consider simulations based on experimental micro-CT images of bone samples artificially blurred and under-sampled. For comparison reason we test the semi-blind TVbox approach on the same synchrotron micro-CT volume of the trabecular human bone presented in Figure 5.1 and deteriorated in the same way. Thus, we recall herein, that the ground-truth was blurred with a Gaussian kernel with a standard deviation $\sigma = 2.425$ and down-sampled at 40 μm (p=2). A Gaussian noise level with standard deviation $\sigma_n = 0.1$ was added to the image. The method was tested on a Volume of Interest (VOI) of $(328)^3$ voxels. Considering the bimodal histogram of the ground truth volume, the binary version of it was obtained with Otsu's method. 3D rendering of the ground-truth and low resolution volume crops are shown in Figure 6.1 (a) and (b).

We recall in Figure 6.1 the resulted volumes obtained with bicubic interpolation, classical TV and the non-blind version of TVbox presented in chapter 5. The proposed semi-blind super-resolution/segmentation TVbox method was applied to the low-resolution volume. The parameters μ and β from step 1 were chosen based on the ground-truth and on the cost function as explained in subsection 5.3. Slices of these volumes are displayed in Figure 6.2. Quantitative parameters as the DICE coefficient, the BV/TV, the Euler number and the density of connectivity are presented in Table 6.1.

Parameter	**Ref.**	**Low resolution**	**Bicubic Interpolation**	**TVbox**	**semi-blind TVbox**
DICE	1	-	0.773	0.908	0.915
Euler no.	-1211	4888	11201	-722	-753
dconn (mm^{-3})	4.86	16.61	11.98	4.20	4.22
BV/TV (%)	11.07	16.48	16.38	11.50	11.45

Table 6.1: Quantitative parameters.

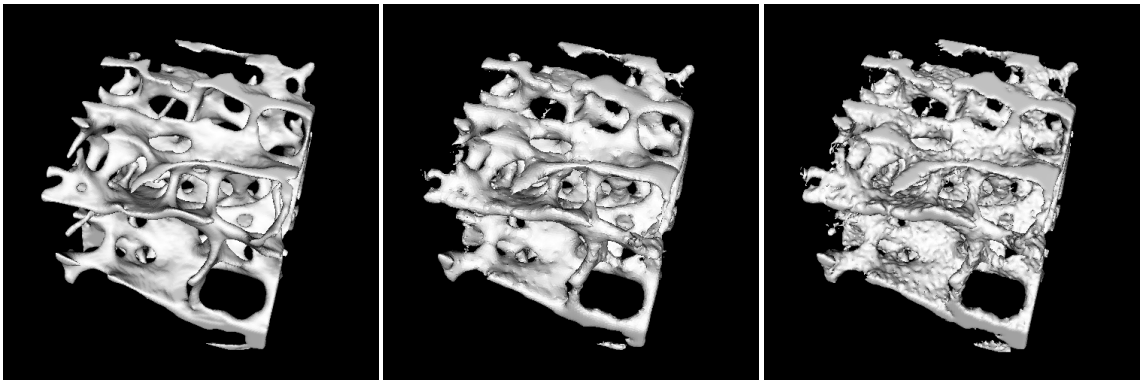

(a) Ground-truth volume (b) Low resolution volume (c) Bicubic interpolation

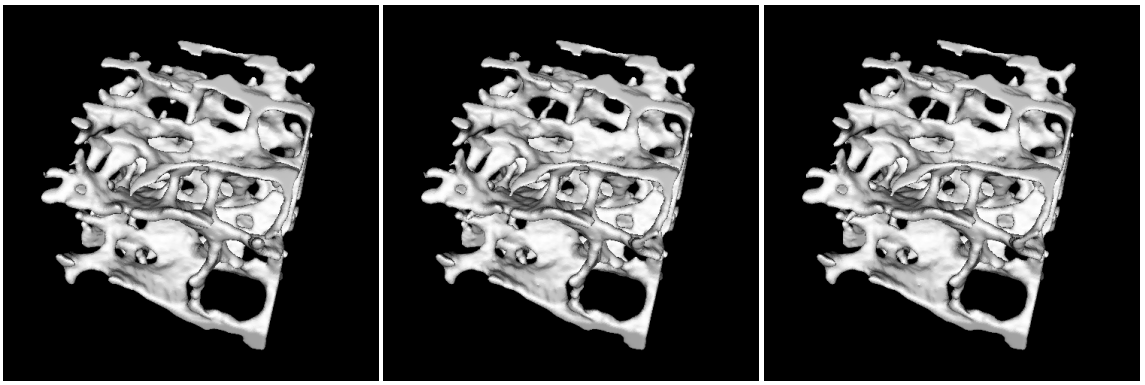

(d) TV regular. (e) TVbox regular. (f) semi-blind TVbox regular.

Figure 6.1: Comparison of 3D restoration methods on experimental synchrotron volume.

6.3.2 Experiments on real images

We present preliminary work on experimental data. 3D images of human radius samples were acquired on a HR-pQCT system from 750 projections and reconstructed at an isotropic voxel size of 82 μm. The same samples were also scanned using a micro-CT system providing 3D images at 24 μm. The HR-pQCT images were first rescaled to a resolution of 41 μm. In Figure 6.3, we show a slice imaged at 82 μm and at 41 μm. The quality of the HR-pQCT image compared to the micro-CT image is lower, due to the blur, spatial resolution and noise. The histograms of these two volumes are shown in Figure 6.4. The bimodal aspect of the micro-CT image histogram assures that an Otsu threshold is sufficient as segmentation step. However, the same method can't be applied to the HR-pQCT image.

We observe that the two initial volumes are not completely overlapped (Figure 6.5) and also, as the images are taken from two different modalities, they must be firstly registered before overlapping them.

In the following subsection we explain the basic concepts of registration.

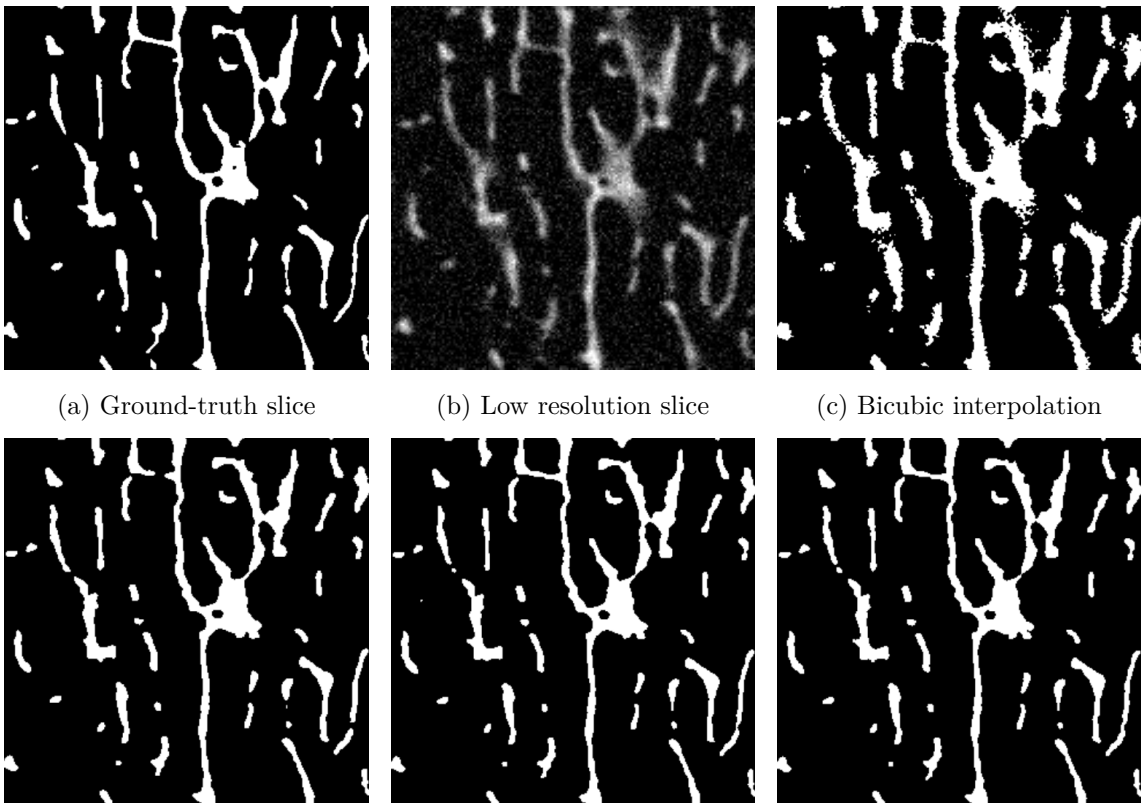

(a) Ground-truth slice (b) Low resolution slice (c) Bicubic interpolation

(d) TV regularization (e) TVbox regular. (f) semi-blind TVbox regular.

Figure 6.2: Slice of the restored experimental synchrotron volume.

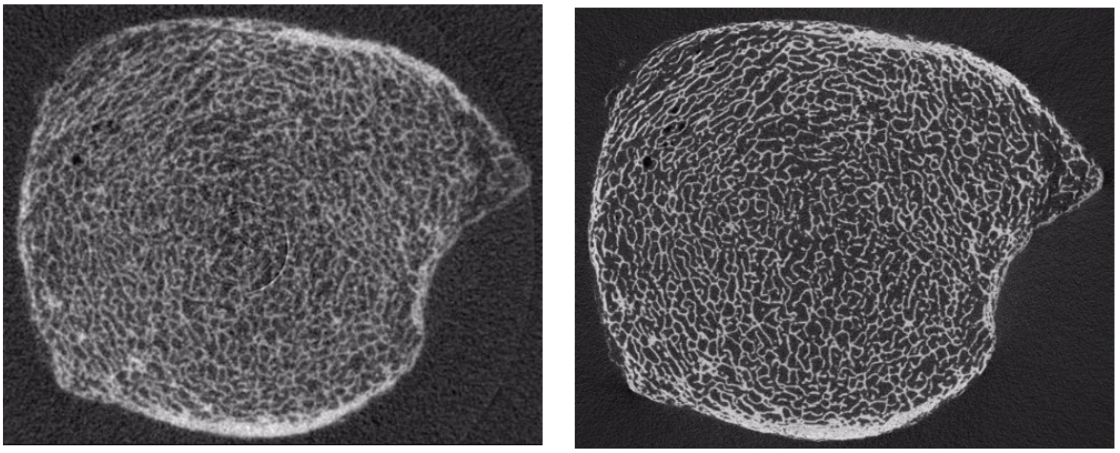

Figure 6.3: Slice of a) HR-pQCT volume at 82 μm and b) micro-CT volume scaled at 41 μm.

Registration

Image registration is a process of spatially aligning a moving image $\mathcal{I}_M$ to a fixed image $\mathcal{I}_F$. In this process, $\mathcal{I}_M$ is deformed by using a transformation function $\mathcal{T}$ in order to

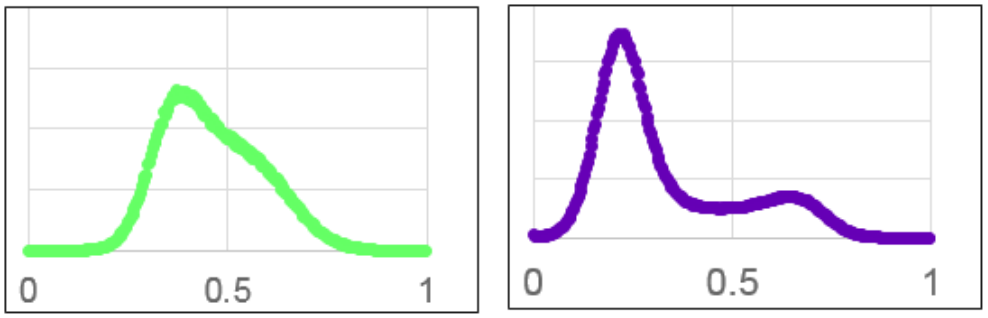

Figure 6.4: Normalized histograms of a) HR-pQCT volume at 82 μm and b) micro-CT volume scaled at 41 μm

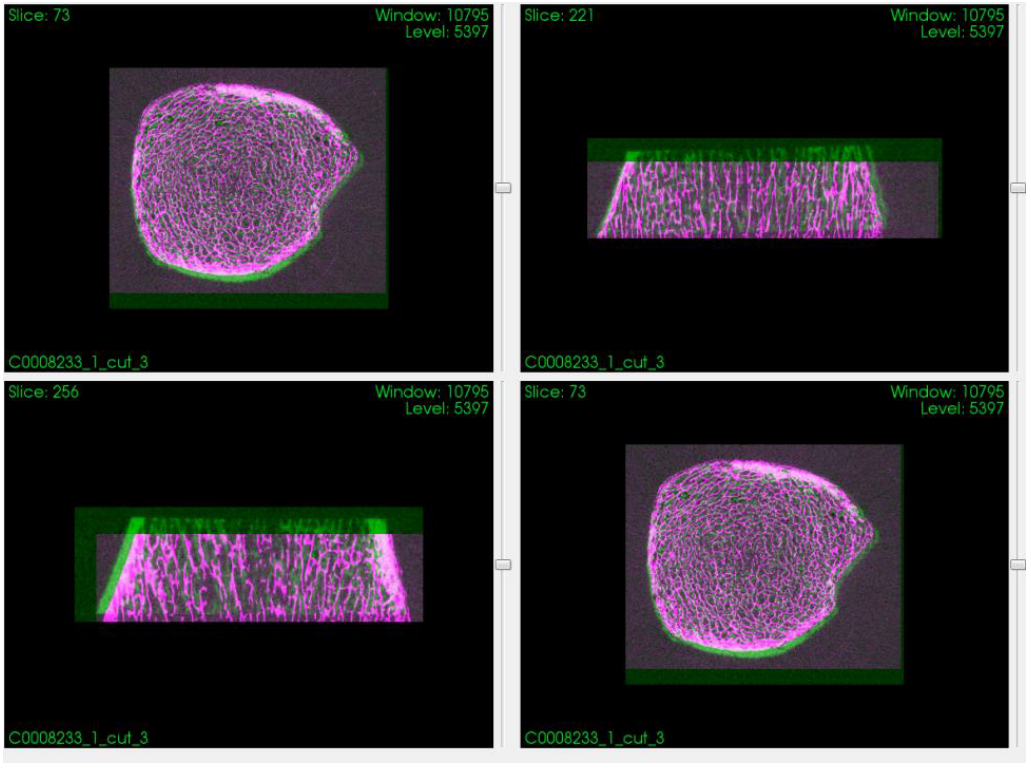

Figure 6.5: The initial spatial overlapped of HR-pQCT and micro-CT volumes using the VV software.

minimize a cost function $\mathcal{C}$ between $\mathcal{T}(\mathcal{I}_M)$ and $\mathcal{I}_F$. The most used type of registration is the parametric registration where the transformation is defined by a vector of parameters $\boldsymbol{u}$. The solution is given by the minimization of the functional:

$$\mathcal{T}_{\boldsymbol{u}}^{*} = \arg\min_{\mathcal{T}_{\boldsymbol{u}}} \mathcal{C}(\mathcal{I}_F, \mathcal{I}_M, \mathcal{T}_{\boldsymbol{u}}), \tag{6.6}$$

where the cost function $\mathcal{C}$ combines a distance function $\mathcal{F}$ between the registered images,

and a regularization term $\mathcal{P}$, which constrains the transformation to smooth deformations. This cost function is defined as:

$$\mathcal{C}(\mathcal{I}_F, \mathcal{I}_M, \mathcal{T}_{\boldsymbol{u}}) = \mathcal{F}(\mathcal{I}_F, \mathcal{I}_M, \mathcal{T}_{\boldsymbol{u}}) + \alpha \mathcal{P}(\mathcal{T}_{\boldsymbol{u}}), \tag{6.7}$$

where α is the weight given to the regularization.

The registration is solved iteratively using an optimizer and an interpolator. The latter is in charge of calculating intensities in non-voxels positions while the moving image is being deformed. Finally, two more components may be used: sampler and pyramids. The former may be used to select a subset of voxels from the images, in order to calculate the distance function between the images. This reduces the computation time required to calculate the distance. The latter is used to help registration avoid local minima in the cost function. The registration process and its components are shown in Figure 6.6.

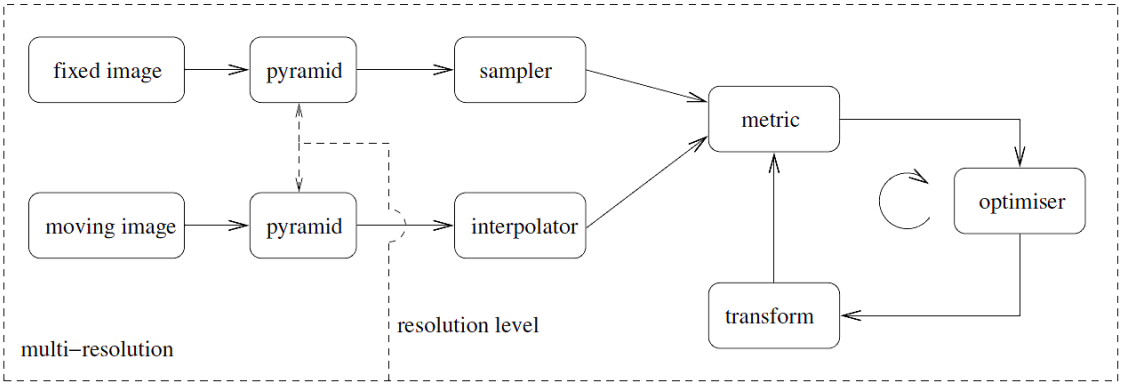

Figure 6.6: The basic registration components [Klein *et al.* (2010), Klein and Staring (2015)]

Given the input images, the micro-CT image at 41 μm is considered to be the fixed image $\mathcal{I}_F$, and the HR-pQCT image at 82 μm, the moving image $\mathcal{I}_M$, with corresponding spatial supports $\Omega_{\mathcal{I}_F} \subset \mathbb{R}^d$ and $\Omega_{\mathcal{I}_M} \subset \mathbb{R}^d$, $d = 3$. Given that the images represent the same object and were imaged ex-vivo, we used a rigid transformation and the sum of squared differences (6.8) as distance function:

$$\mathrm{SSD}(\mathcal{I}_F, \mathcal{I}_M, \mathcal{T}_{\boldsymbol{u}}) = \frac{1}{|\Omega_{\mathcal{I}_F}|} \sum_{\boldsymbol{i} \in \Omega_{\mathcal{I}_F}} \Big(\mathcal{I}_F(\boldsymbol{i}) - \mathcal{I}_M(\, \mathcal{T}_{\boldsymbol{u}}^{-1}(\boldsymbol{i}) \,) \Big)^2 . \tag{6.8}$$

We can see from Figure 6.5 that the images are slightly translated. As suggested in the Elastix implementation manual [Klein and Staring (2015)], we used a stochastic gradient descent optimizer and a B-Spline interpolator. As a final result of the registration we obtained the transformation parameters (six parameters for rigid-registration):

$$\boldsymbol{u} = (\theta_x, \theta_y, \theta_z, t_x, t_y, t_z)^T \tag{6.9}$$

where the first three parameters define the rotation angles around the three axes (in rad) and the last three parameters, the translation vector. We then applied the transformation parameters to deform the low-resolution image in order to overlap it to the high-resolution image, for allowing comparative measures. Figure 6.7 presents the steps required in the case of image registration.

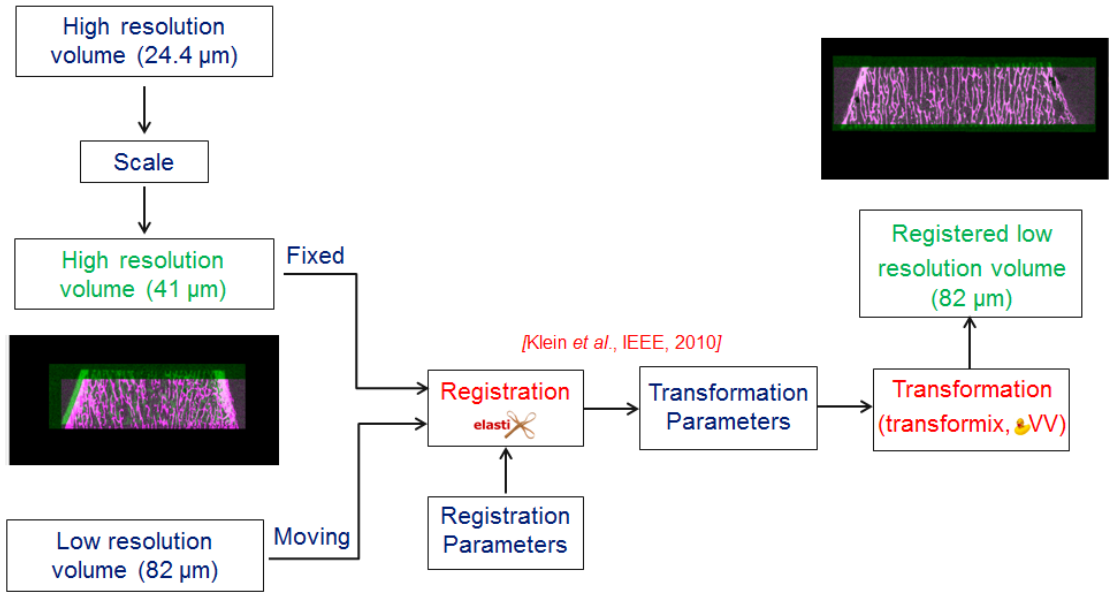

Figure 6.7: Registration schema of HR-pQCT images and micro-CT images.

Results on real data

Figures 6.8(a) and (b) show a region of interest (ROI) within the micro-CT image resampled at 41 μm and the original HR-pQCT image at 82 μm. With real data, only the semi-blind TVbox approach could be applied. Figures 6.8(c) and (d) show the bicubic interpolated slice and a first result of the super-resolved TVbox image with the up-sampled factor p=2. The best results were obtained with the initial value of the $\sigma^{(0)}$=0.5. We may note that the DICE index is increased with the TVbox method (0.7 versus 0.61) compared to bicubic interpolation.

We can observe that for the semi-blind TVbox case the bone structure is over-segmented and in some regions the connectivity is better restored. If for the test images this problem is solved by tunning the regularization parameter μ, for the real images the tunning task is more complex.

A possible improvement of the presented semi-blind TVbox method could be given by a re-estimation of the parameters c_0 and c_1 jointly with the standard deviation of the blur kernel, at each iteration of the algorithm. The assumption that the blur is a Gaussian kernel could also introduce errors in the semi-blind TVbox method.

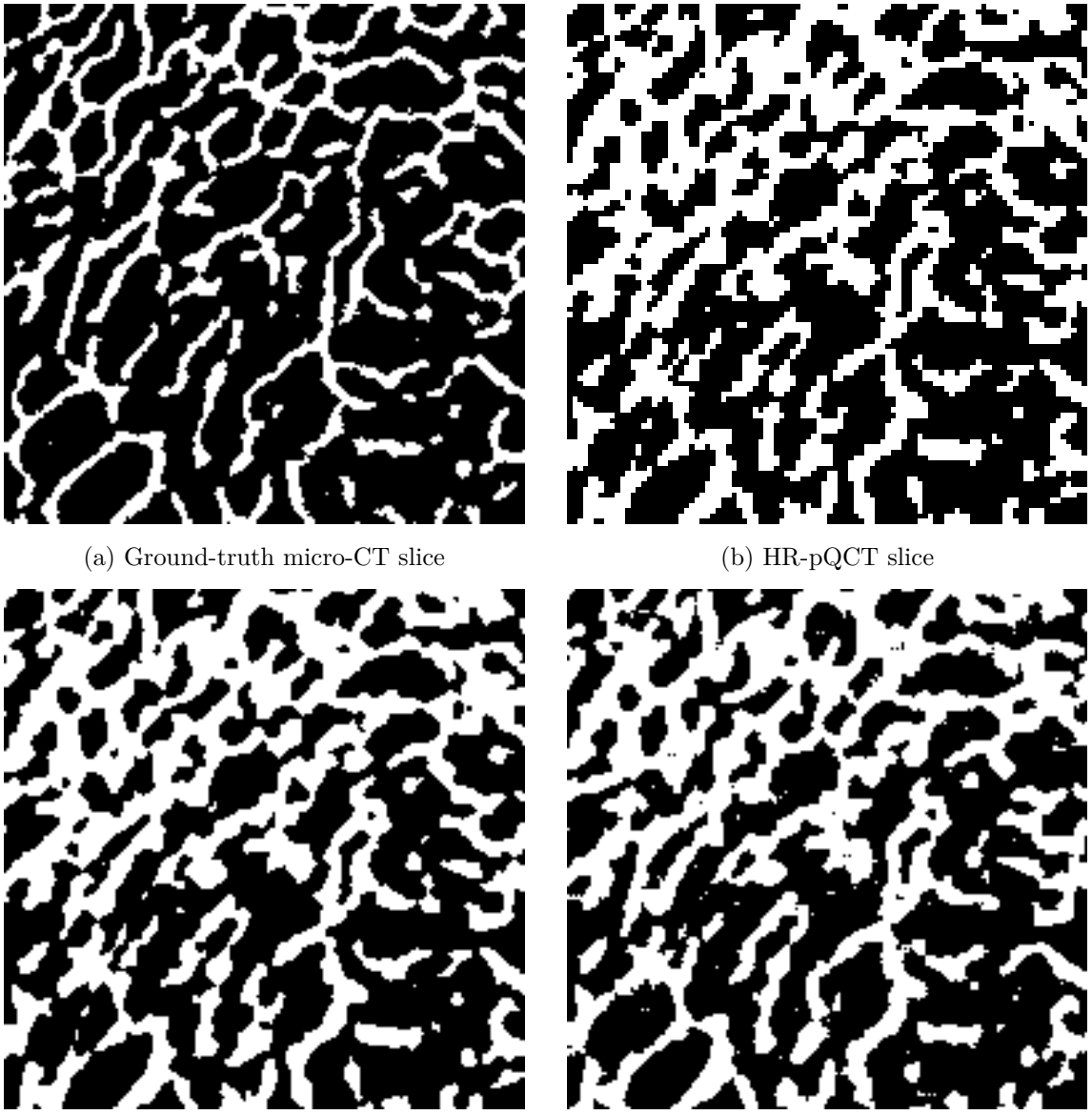

(a) Ground-truth micro-CT slice

(b) HR-pQCT slice

(c) Bicubic interpolation

(d) semi-blind TVbox regular.

Figure 6.8: Slice of the restored HR-pQCT volume.

6.4 Conclusions

In this chapter, we proposed a semi-blind joint super-resolution/ segmentation method based on the Total Variation regularization with convex constraint and ADMM minimization for improving the trabecular bone micro-structure quantification from micro-CT volumes. We compared this semi-blind TVbox approach with the standard interpolation method in terms of DICE and structural parameters. For artificially deteriorated Synchrotron images a comparison with the non-blind TVbox method was performed. We showed that our semi-blind method improves the structural parameters compared to the original ones. It outperforms clearly the interpolation method. Preliminary results show

that the approach can be applied to real HR-pQCT images for which we have a ground truth image. In further work, we shall address the optimization of the algorithm parameters and particularly the choice of c_0 and c_1 used for box constraints. We will also consider anisotropic and spatially varying blurring kernel. Other segmentation methods to obtain the binary version of the low resolution image and bicubic interpolation will be investigated.

Conclusions and perspectives

In this thesis, we have investigated methods to improve the quantification of the trabecular bone micro-structure from CT images. Specifically, our aim was to explore super-resolution techniques by considering that the given CT image was blurred, under-sampled and noisy. In addition, since the final goal to apply quantification is to obtain a binary image of bone micro-architecture, we considered the combined super-resolution/segmentation problem. We used variational approaches with different regularization terms. Moreover, we have also addressed the problem of the regularization parameter choice. The various approaches are tested on 2D images and 3D volumes, obtained from simulations or real data from bone samples.

Firstly, we investigated super-resolution 2D methods based on TV. The basic TV regularization method was extended to higher degree TV regularization because the TV term can create staircasing effects. We expand the ADMM minimization method to isotropic HDTV (Higher Degree TV) regularization. Furthermore, we introduced a general formulation of the regularization term for both methods and derived an efficient minimization scheme. A comparison of the methods was performed on noisy low-resolution images of the bone micro-structure in terms of PSNR, structural and segmentation parameters. The TV based approaches improve standard interpolation methods. Yet, TV and HDTV give similar super-resolved images.

Moreover, we presented a new method to select the TV regularization parameter. This method generalizes the classical Morozov principle. The convergence of the TV with this a posteriori choice of the parameter was investigated. A very fast scheme to obtain this parameter was detailed. Numerical comparisons were presented with other methods like the Unbiased Predictive Risk Estimator. Several images and noise levels were tested. Very good results were obtained with our method which outerperformed the other approaches.

The next part of this manuscript was related to the joint super-resolution /segmentation problem in 3D. The super-resolution and segmentation problems are often considered as separate problems. Herein, we seek to solve both inverse problems at the same time. The method was based on a convex additional box constraints(i.e., the solution must be in a convex set). The minimization method must be modified to include this convex constraint. Our results were presented on 3D volumes. The restored bone volumes and its connectivity were improved with this new constraint.

The last chapter of the thesis presented a semi-blind joint resolution/segmentation

method. An alternate minimization algorithm was used to recover the images and the blur kernel which was assumed to be a Gaussian kernel. The approach was tested on synchrotron and on *ex-vivo* HR-pQCT trabecular bone images. The semi-blind approach improved the structural parameters and leaded to a good estimate of the blur kernel on test images.

This thesis was a preliminary work for the difficult problem under study. Many aspects remain to be investigated: A first possible extension of this work is the use of new regularization terms like the Potts regularization functional. This sets more difficult minimization problems for the regularization functional but may improve the reconstruction results. A good parameter choice scheme has been proposed for TV regularization applied to super-resolution. Yet, it may be interesting to study an adaptive method for more difficult reconstruction problems. In this work, we regularized the blind reconstruction functional with terms related to the input image. More complex functional may be used and the regularization parameter choice problem may be investigated more precisely. The minimization of the regularization functional was done with the ADMM algorithm. The comparison with the proximal methods may represent an interesting research perspective. More realistic validation of the alternate minimization method presented has to be performed on ex-vivo HR-pQCT images for which the corresponding ground-truth micro-CT images are available. The blind super-resolution problem has to be studied on simulated data and real bone images. Different approaches mentioned in the bibliographic chapter for blind inverse problems may be compared. The approaches of [Ramlau and Ring (2007)] and the bilevel methodology are very interesting directions for future research.

Appendix

Appendix A

The L_p norm

Considering a vector $x = (x_1, x_2, ...x_N)$ the l_p norm of x is denoted $\|x\|_{l_p}$ or $\|x\|_p$ and is defined as:

$$\|x\|_{l_p} = \left(\sum_{i=1}^{N} |x_i|^p \right)^{\frac{1}{p}} \tag{A.1}$$

The most used norms are:

$$\|x\|_{l_\infty} = \underset{i=1...N}{max} |x_i| \tag{A.2}$$

$$\|x\|_{l_1} = \sum_{i=1}^{N} |x_i| \tag{A.3}$$

$$\|x\|_{l_2} = \sqrt{\sum_{i=1}^{N} |x_i|^2} \tag{A.4}$$

When x is a matrix of size M x N, the norms defined above treat the matrix as a vector of size MN:

$$\|x\|_p = \left(\sum_{i=1}^{M} \sum_{j=1}^{N} |x_{ij}|^p \right)^{\frac{1}{p}} \tag{A.5}$$

Considering $p = 2$ in equation (A.5) we obtain the Frobenius norm.
Moreover, in the continuous case the $\sum$ is replaced by $\int$ and the notation used is L_p. However, the l_0 norm is not defined in the continuous domain, The equivalent norm is the $\|.\|_\infty$
The finite dimensional case is a special case of the function case, with a well chosen integration measure. The set of L_p-functions (where p>=1) generalize the L_2-space. For a function f to be in L_p it should be p-integrable.

On a measure space X, the L_p norm of a function f is:

$$\|f\|_{L_p} = \left(\int_X |f|^p \right)^{\left(\frac{1}{p}\right)} \tag{A.6}$$

The L_p-functions are the functions for which this integral converges. For $p \neq 2$, the space of L_p-functions is a Banach space.

Appendix B

Convex analysis

The **line segment** between x and y is given by all the points:

$$z = \alpha x + (1 - \alpha)y \tag{B.1}$$

with $0 \leq \alpha \leq 1$.

A set $C \subseteq \mathbb{R}^N$ is **convex** if the line segment between any two points $x, y \in C$ is included in the set:

$$\alpha x + (1 - \alpha)y \in C, \forall \alpha \in [0, 1] \tag{B.2}$$

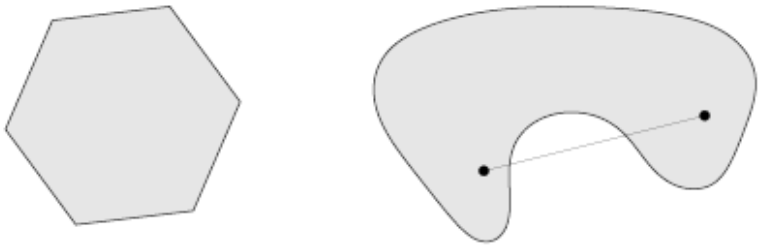

Figure B.1: Example of a convex (left) and a non-convex set (right) [Boyd and Vandenberghe (2004)]

Given a convex set $C \subseteq \mathbb{R}^N$, the function $f(x) : C \to \mathbb{R}$ is said to be **convex** on C if $\forall x, y \in C$ and $\alpha \in (0, 1)$:

$$f(\alpha x + (1 - \alpha)y) \leq \alpha f(x) + (1 - \alpha)f(y) \tag{B.3}$$

In the case when the inequality (B.3) is strict, the function f is said to be **strictly convex**.

The function $f : \mathbb{R}^N \to \mathbb{R}$ is **differentiable** if its derivative exists at each point x in its domain.

Let $f : \mathbb{R}^N \to \mathbb{R} \cup +\infty$ be a closed proper convex function, which means that its **epigraph**

$$\mathbf{epi}f = \Big\{(x,t) \in \mathbb{R}^N \times \mathbb{R} | f(x) \leq t\Big\} \tag{B.4}$$

is a nonemplty closed convex set. The **effective domain** of f is the set of points for which f takes on finite values:

$$\mathbf{dom}f = \Big\{x \in \mathbb{R}^N \mid f(x) < +\infty\Big\} \tag{B.5}$$

We say a vector $g \in \mathbb{R}^N$ is a **subgradient** of a function $f : \mathbb{R}^N \to \mathbb{R}$ at $x \in domf$ if for all $z \in domf$:

$$f(z) \geq f(x) + g^T(z - x). \tag{B.6}$$

If f is convex and differentiable, then its gradient at x is a subgradient and even more is its only subgradient (i.e. $\partial f(x) = \nabla f(x)$). Conversely, if f is convex and $\partial f(x) = g$, then f is differentiable at x and $g = \nabla f(x)$.

As illustrated in Figure B.2, a function f can have more that one subgradient at a point x. Also the subgradients can exist even when f is not differentiable at x.

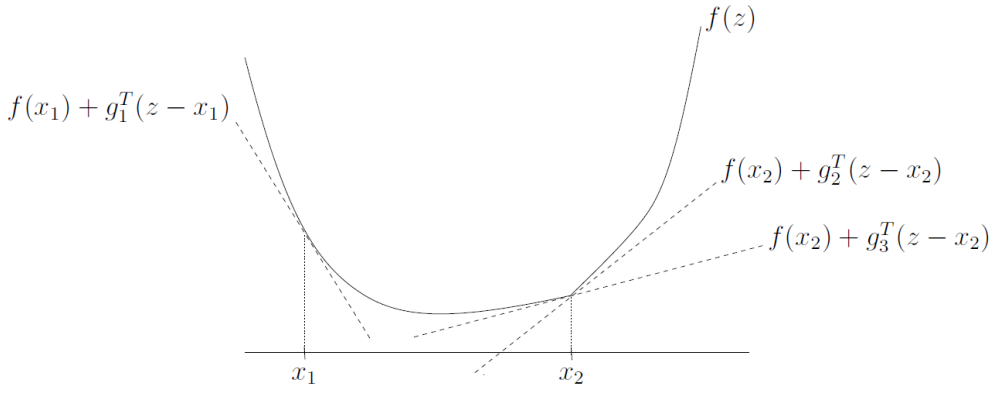

Figure B.2: The given convex function f is differentiable in x_1 but not in x_2. At the point x_1, the g_1 (which is the derivative of f in x_1) is the unique subgradient at x_1. At the point x_2, f has many subgradients from which two are shown, g_2 and g_3 [Boyd and Vandenberghe (2004)]

A function f is called **subdifferentiable** at x if there exists at least one subgradient at x. The set of subgradients of f at the point x is called the **subdifferential** of f at x, and is denoted $\partial f(x)$.
A function f is called **subdifferentiable** if it is subdifferentiable at all $x \in domf$.

The subdifferential $\partial f(x)$ is always a closed convex set, even if f is not convex. In addition, if f is continuous at x, then the subdifferential $\partial f(x)$ is bounded.

A point x^* is a minimizer of a function f (not necessarily convex) if and only if f is subdifferentiable at x^* and $0 \in \partial f(x^*)$, i.e. $g = 0$ is a subgradient of f at x^*.

Indicator function

Let $C \subseteqq \mathbb{R}^N$ be a convex set. The convex function I_C is called the **indicator function** of the set C and is defined by:

$$I_C = \begin{cases} 0 & x \in C \\ \infty & x \notin C \end{cases} \tag{B.7}$$

The subdifferential of the indicator function, I_C, at x is known as the **normal cone**, $N_C(x)$, of C:

$$N_C(x) = \partial I_C(x) = \left\{ g \in \mathbb{R}^N : g^T x \geq g^T y, \ for\ any\ y \in C \right\} \tag{B.8}$$

Optimality condition

For a convex function f,

$$f(x^*) = \min_{x \in \mathbb{R}^n} f(x) \Leftrightarrow 0 \in \partial f(x^*) \tag{B.9}$$

The proof is based on the fact that if $g = 0$ is a subgradient means that for all y:

$$f(y) \geq f(x^*) + 0^T(y - x^*) = f(x^*) \tag{B.10}$$

Soft-thresholding

Given the minimization problem:

$$f(x) = \min_x \frac{1}{2}\|y - x\|^2 + \lambda \|x\|_1 \tag{B.11}$$

its solution is $x^* = S_\lambda(y)$, where $S_\lambda(y)$ is the soft-thresholding operator:

$$S_\lambda(y) = \begin{cases} y_i - \lambda & y_i > \lambda \\ 0 & -\lambda \leq y_i \leq \lambda \\ y_i + \lambda & y_i < -\lambda \end{cases} \tag{B.12}$$

Proximal operator

The **proximal operator** $prox_f : \mathbb{R}^N \to \mathbb{R}^N$ of $f : \mathbb{R}^N \to \mathbb{R} \cup +\infty$ is defined by:

$$prox_f(v) = \arg\min_x (f(x) + \frac{1}{2}\|x - v\|_2^2) \tag{B.13}$$

The proximal operator of the scaled function λf, where $\lambda > 0$ (also called the proximal operator of f with parameter λ)

$$prox_{\lambda f}(v) = \arg\min_x (f(x) + \frac{1}{2\lambda}\|x - v\|_2^2) \tag{B.14}$$

Throughout this appendix, we make the convention that when we refer to the proximal operator of a function, the function is assumed to be closed proper convex.

The proximal operator of the indicator function, I_C is reduces to Euclidean projection onto C:

$$\Pi_C(v) = \arg\min_{x \in C} \|x - v\|_2 \tag{B.15}$$

The proximal operator $prox_{\lambda f}$ and the subdifferential operator ∂f are related as follows:

$$prox_{\lambda f} = (I + \lambda \partial f)^{-1} \tag{B.16}$$

Appendix C

TV ADMM Super-resolution

This appendix comes to complete the ADMM minimization method described in chapter 3 and 4. We detail herein how the updates of the TV ADMM super-resolution approach are obtained.
Having the following augmented Lagrangian:

$$\mathcal{L}_{\mathrm{A}}(\boldsymbol{f},\{\boldsymbol{h}_i\},\{\boldsymbol{\lambda}_i\}) = \frac{\mu}{2}\left\|\boldsymbol{A}\boldsymbol{f}-\boldsymbol{g}^{\delta}\right\|_2^2 + \sum_i \|\boldsymbol{h}_i\| + \sum_i \left[\frac{\beta}{2}\|\boldsymbol{h}_i-\boldsymbol{P}_i\,\boldsymbol{f}\|^2 - \boldsymbol{\lambda}_i^{\mathrm{t}}(\boldsymbol{h}_i-\boldsymbol{P}_i\,\boldsymbol{f})\right] \tag{C.1}$$

the first order optimality conditions of its saddle point are given by:

$$\begin{aligned} \partial_{\boldsymbol{f}}(\mathcal{L}_{\mathrm{A}}) &= 0 \\ \partial_{\boldsymbol{h}_i}(\mathcal{L}_{\mathrm{A}}) &= 0 \\ \boldsymbol{h}_i - \boldsymbol{P}_i\boldsymbol{f} &= 0 \end{aligned} \tag{C.2}$$

We recall that for $\boldsymbol{f}$ and $\boldsymbol{b} \in \mathbb{R}^N$:

$$\nabla_{\boldsymbol{f}}(\|\boldsymbol{A}\boldsymbol{f}-\boldsymbol{g}\|_2^2) = \nabla_{\boldsymbol{f}}(\|\boldsymbol{g}-\boldsymbol{A}\boldsymbol{f}\|_2^2) = 2\boldsymbol{A}^t(\boldsymbol{A}\boldsymbol{f}-\boldsymbol{g}) \tag{C.3}$$

$$\nabla_{\boldsymbol{f}}(\boldsymbol{b}^t\boldsymbol{f}) = \nabla_{\boldsymbol{f}}(\boldsymbol{f}^t\boldsymbol{b}) = \boldsymbol{b} \tag{C.4}$$

First update

From the first KKT optimality condition, the super-resolved image, $\boldsymbol{f}^{k+1}$, is obtained:

$$\nabla_{\boldsymbol{f}}\Big(\frac{\mu}{2}\left\|\boldsymbol{A}\boldsymbol{f}-\boldsymbol{g}^{\delta}\right\|_2^2 + \sum_i \left[\frac{\beta}{2}\|\boldsymbol{h}_i-\boldsymbol{P}_i\,\boldsymbol{f}\|^2 + \boldsymbol{\lambda}_i^{\mathrm{t}}\boldsymbol{P}_i\,\boldsymbol{f}\right]\Big) = 0 \tag{C.5}$$

$$\mu\boldsymbol{A}^t(\boldsymbol{A}\boldsymbol{f}-\boldsymbol{g}^{\delta}) + \sum_i [\beta\boldsymbol{P}_i{}^t(\boldsymbol{P}_i\,\boldsymbol{f}-\boldsymbol{h}_i) + (\boldsymbol{\lambda}_i^{\mathrm{t}}\boldsymbol{P}_i\,)^t] = 0 \tag{C.6}$$

$$(\mu \boldsymbol{A}^{\mathrm{t}}\boldsymbol{A} + \sum_i \beta \boldsymbol{P}_i^{\mathrm{t}}\boldsymbol{P}_i)\boldsymbol{f} = \mu \boldsymbol{A}^{\mathrm{t}}\boldsymbol{g}^{\delta} + \sum_i \boldsymbol{P}_i^{\mathrm{t}}(\beta \boldsymbol{h}_i^k - \boldsymbol{\lambda}_i^k) \tag{C.7}$$

This linear system is solved using the PCG method. As first guess we consider $\boldsymbol{f}^0 = \boldsymbol{A}^t\boldsymbol{g}^{\delta}$. The implementation of ADMM was made in Matlab and to avoid the high dimension of the left-hand side matrix, a function is given as input parameter to the PCG Matlab function and all operations are made in the frequency domain.

Second update

The auxiliary variables, $\boldsymbol{h}_i$, are obtained from:

$$\partial_{\boldsymbol{h}}(\sum_i \|\boldsymbol{h}_i\| + \sum_i \left[\frac{\beta}{2}\|\boldsymbol{h}_i - \boldsymbol{P}_i\,\boldsymbol{f}\|^2 - \boldsymbol{\lambda}_i^{\mathrm{t}}\boldsymbol{h}_i\right]) = 0 \tag{C.8}$$

$$\partial_{\boldsymbol{h}}\|\boldsymbol{h}_i\| + \beta(\boldsymbol{h}_i - \boldsymbol{P}_i\,\boldsymbol{f}) - \boldsymbol{\lambda}_i = 0 \tag{C.9}$$

$$\frac{\partial_{\boldsymbol{h}}\|\boldsymbol{h}_i\|}{\beta} + \boldsymbol{h}_i = \boldsymbol{P}_i\,\boldsymbol{f} + \frac{\boldsymbol{\lambda}_i}{\beta} \tag{C.10}$$

We distinguish two cases in the calculation of the subdifferential:

$$\partial_{\boldsymbol{h}}\|\boldsymbol{h}_i\| = \begin{cases} \in [-1,1] & \boldsymbol{h}_i = 0 \\ \frac{\boldsymbol{h}_i}{\|\boldsymbol{h}_i\|} & \boldsymbol{h}_i \neq 0 \end{cases} \tag{C.11}$$

Using (C.10) and (C.11) the update of the auxiliary variables, $\boldsymbol{h}_i$ is rewritten as:

$$\boldsymbol{h}_i = \mathcal{S}_{\beta}\left(\boldsymbol{P}_i\boldsymbol{f} + \boldsymbol{\lambda}_i/\beta\right), \tag{C.12}$$

where $\mathcal{S}_{\beta}(\boldsymbol{u}) = \max\left(1 - \frac{1}{\beta\|\boldsymbol{u}\|}, 0\right)\cdot \boldsymbol{u}$ is the soft-thresholding operator.

Third update

The Lagrangian multipliers, $\boldsymbol{\lambda}_i$, are given directly by:

$$\boldsymbol{\lambda}_i^{k+1} = \boldsymbol{\lambda}_i^k - \beta\left(\boldsymbol{h}_i^{k+1} - \boldsymbol{P}_i\boldsymbol{f}^{k+1}\right) \tag{C.13}$$

Appendix D

TVbox ADMM Super-resolution/segmentation

This appendix comes to complete the description of the ADMM minimization method presented and applied in chapter 5 and 6. We detail herein how the updates of the TVbox ADMM joint super-resolution/segmentation approach were obtained.
Having the following augmented Lagrangian:

$$\mathcal{L}_{\mathrm{A}}(\boldsymbol{s},\{\boldsymbol{h}_i\},\boldsymbol{l},\{\boldsymbol{\lambda}_i\},\boldsymbol{\lambda_C}) = \frac{\mu}{2}\left\|\boldsymbol{A}\boldsymbol{s}-\boldsymbol{g}^{\delta}\right\|_2^2 + \sum_i \|\boldsymbol{h}_i\| \; + \sum_i \left[\frac{\beta}{2}\|\boldsymbol{h}_i-\boldsymbol{D}_i\,\boldsymbol{s}\|^2 - \boldsymbol{\lambda}_i^{\mathrm{t}}(\boldsymbol{h}_i-\boldsymbol{D}_i\,\boldsymbol{s})\right] \tag{D.1}$$
$$+\boldsymbol{I_C}(\boldsymbol{l}) + \frac{\beta}{2}\|\boldsymbol{l}-\boldsymbol{s}\|_2^2 - \boldsymbol{\lambda}_{\boldsymbol{C}}^t(\boldsymbol{l}-\boldsymbol{s})$$

First update

$$\nabla_{\boldsymbol{s}}(\frac{\mu}{2}\|\boldsymbol{A}\boldsymbol{s}-\boldsymbol{g}^{\delta}\|_2^2+\sum_i[\frac{\beta}{2}\|\boldsymbol{h}_i-\boldsymbol{D}_i\boldsymbol{s}\|_2^2-\boldsymbol{\lambda}_i^t(\boldsymbol{h}_i-\boldsymbol{D}_i\boldsymbol{s})]+\frac{\beta}{2}\|\boldsymbol{l}-\boldsymbol{s}\|_2^2-\boldsymbol{\lambda}_{\boldsymbol{C}}^t(\boldsymbol{l}-\boldsymbol{s}))=0 \tag{D.2}$$

$$\mu\boldsymbol{A}^t(\boldsymbol{A}\boldsymbol{s}-\boldsymbol{g}^{\delta})+\sum_i[\beta\boldsymbol{D}_i^t(\boldsymbol{D}_i\boldsymbol{s}-\boldsymbol{h}_i)+(\boldsymbol{\lambda}_i^t\boldsymbol{D}_i)^t]+\beta(\boldsymbol{s}-\boldsymbol{l})+\boldsymbol{\lambda_C}=0 \tag{D.3}$$

$$(\mu\boldsymbol{A}^t\boldsymbol{A}+\sum_i\beta\boldsymbol{D}_i^t\boldsymbol{D}_i+\beta I)\boldsymbol{s}=\mu\boldsymbol{A}^t\boldsymbol{g}^{\delta}+\sum_i\boldsymbol{D}_i^t(\beta\boldsymbol{h}_i-\boldsymbol{\lambda}_i)+\beta\boldsymbol{l}-\boldsymbol{\lambda_C} \tag{D.4}$$

As in the TV super-resolution case (Appendix C), this step is solved by the PCG method.

Second update

The auxiliary variables, $\boldsymbol{h}_i$, are updated as showed in Appendix C (second update), by

a soft-thresholding operator. Starting from:

$$\partial_{\boldsymbol{h}}(\sum_i \|\boldsymbol{h}_i\| + \sum_i \left[\frac{\beta}{2}\|\boldsymbol{h}_i - \boldsymbol{D}_i\,\boldsymbol{s}\|^2 - \boldsymbol{\lambda}_i^{\mathrm{t}}\boldsymbol{h}_i\right]) = 0 \tag{D.5}$$

we obtain:

$$\boldsymbol{h}_i = \mathcal{S}_\beta\left(\boldsymbol{D}_i\boldsymbol{s}^{k+1} + \boldsymbol{\lambda}_i^k/\beta\right), \tag{D.6}$$

where $\mathcal{S}_\beta(\boldsymbol{u}) = \max\left(1 - \frac{1}{\beta\|\boldsymbol{u}\|}, 0\right)\cdot\boldsymbol{u}$ is the soft-thresholding operator.

Third update

The auxiliary variable, $\boldsymbol{l}$ is related to the box constraints and it is obtained from:

$$\partial_l(\boldsymbol{I}_{\boldsymbol{C}}(\boldsymbol{l}) + \frac{\beta}{2}\|\boldsymbol{l} - \boldsymbol{s}\|_2^2 - \boldsymbol{\lambda}_{\boldsymbol{C}}^t(\boldsymbol{l} - \boldsymbol{s})) = 0 \tag{D.7}$$

$$\partial_{\boldsymbol{l}}\boldsymbol{I}_{\boldsymbol{C}}(\boldsymbol{l}) + 2\beta(\boldsymbol{l} - \boldsymbol{s}) - \boldsymbol{\lambda}_{\boldsymbol{C}} = 0 \tag{D.8}$$

$$\frac{1}{2\beta}\partial_{\boldsymbol{l}}\boldsymbol{I}_{\boldsymbol{C}}(\boldsymbol{l}) + \boldsymbol{l} = \boldsymbol{s} + \frac{\boldsymbol{\lambda}_{\boldsymbol{C}}}{2\beta} \tag{D.9}$$

Applying (B.16), eq. (D.9) it reduces to the projector operator, $\pi_{\boldsymbol{C}}$, on the convex set $\boldsymbol{C}$:

$$\boldsymbol{l}^{k+1} = \pi_{\boldsymbol{C}}(\boldsymbol{s}^k + \frac{\boldsymbol{\lambda}_{\boldsymbol{C}}^k}{\beta}), \tag{D.10}$$

Fourth update

The Lagrange multipliers, $\boldsymbol{\lambda}_i$, are obtained from:

$$\boldsymbol{\lambda}_i^{k+1} = \boldsymbol{\lambda}_i^k - \beta\left(\boldsymbol{h}_i^{k+1} - \boldsymbol{D}_i\boldsymbol{s}^{k+1}\right). \tag{D.11}$$

Fifth update

The Lagrange multiplier, $\boldsymbol{\lambda}_{\boldsymbol{C}}$, is:

$$\boldsymbol{\lambda}_{\boldsymbol{C}}^{k+1} = \boldsymbol{\lambda}_{\boldsymbol{C}}^k - \beta\left(\boldsymbol{l}^{k+1} - \boldsymbol{s}^{k+1}\right). \tag{D.12}$$

List of publications

Journals papers

A. Toma, B. Sixou, F. Peyrin, (2015) "Iterative choice of the optimal regularization parameter in TV image restoration", Journal of Inverse Problems and Imaging, 9(4): 1171-1191

B. Sixou, **A. Toma**, L. Denis, F. Peyrin, "Iterative choice of the optimal regularization parameter in TV image deconvolution", J. Phys.: Conf. Ser. 464 (2013) 012005

Conference papers

Y. Li, **A. Toma**, B. Sixou, F. Peyrin, "Super-resolution/segmentation of 2D trabecular bone images by a Mumford-Shah approach and comparison to Total Variation", submitted to EUSIPCO 2016

F. Peyrin, **A. Toma**, L. Denis, B. Sixou, A. Burghardt, J.B. Pialat, "Semi-Blind Joint Super-resolution/Segmentation of 3D Trabecular Bone Images by a TV BOX approach", EUSIPCO 2015, Nice, France, 1-4 September 2015, pp 2861 - 2865

A. Toma, L. Denis, B. Sixou, J.B. Pialat, F. Peyrin, "Total variation Super-resolution for 3D trabecular bone micro-structure segmentation", EUSIPCO 2014, Lisbon, Portugal, 1-5 September 2014, pp 2220 - 2224

A. Toma, B. Sixou, L. Denis, J.B. Pialat, F. Peyrin, "Higher order Total Variation super-resolution from a single trabecular bone image", ISBI 2014, Beijing, China, April 2014, pp 1152-1155

Bibliography

[Abboud *et al.* (2014)] Abboud, F., Chouzenoux, E., Pesquet, J.-C., Chenot, J.-H., and Laborelli, L. (2014). A hybrid alternating proximal method for blind video restoration. In *Signal Processing Conference (EUSIPCO), 2014 Proceedings of the 22nd European*, pages 1811–1815.

[Afonso *et al.* (2010)] Afonso, M., Bioucas-Dias, J., and Figueiredo, M. (2010). Fast Image Recovery Using Variable Splitting and Constrained Optimization. *IEEE Transactions on Image Processing*, 19(9):2345–2356.

[Aguiar and Moura (2001)] Aguiar, P. and Moura, J. (2001). Three-dimensional modeling from two-dimensional video. *IEEE Transactions on Image Processing*, 10(10):1541–1551.

[Akhter *et al.* (2007)] Akhter, M. P., Lappe, J. M., Davies, K. M., and Recker, R. R. (2007). Transmenopausal changes in the trabecular bone structure. *Bone*, 41(1):111–116.

[Ambrosio *et al.* (2000)] Ambrosio, L., Fusco, N., and Pallara, D. (2000). *Functions of Bounded Variation and Free Discontinuity Problems*. Clarendon Press.

[Ammann and Rizzoli (2003)] Ammann, P. and Rizzoli, R. (2003). Bone strength and its determinants. *Osteoporosis international: a journal established as result of cooperation between the European Foundation for Osteoporosis and the National Osteoporosis Foundation of the USA*, 14 Suppl 3:S13–18.

[Aubert and Kornprobst (2002)] Aubert, G. and Kornprobst, P. (2002). *Mathematical Problems in Image Processing: Partial Differential Equations and the Calculus of Variations*, volume 147. Springer Science & Business Media.

[Aujol and Gilboa (2006)] Aujol, J.-F. and Gilboa, G. (2006). Constrained and SNR-Based Solutions for TV-Hilbert Space Image Denoising. *Journal of Mathematical Imaging and Vision*, 26(1-2):217–237.

[Babacan *et al.* (2008)a] Babacan, S., Molina, R., and Katsaggelos, A. (2008a). Parameter Estimation in TV Image Restoration Using Variational Distribution Approximation. *IEEE Transactions on Image Processing*, 17(3):326–339.

[Babacan *et al.* (2008)b] Babacan, S., Molina, R., and Katsaggelos, A. (2008b). Total variation super resolution using a variational approach. In *15th IEEE International Conference on Image Processing, 2008. ICIP 2008*, pages 641–644.

[Babacan *et al.* (2009)] Babacan, S., Molina, R., and Katsaggelos, A. (2009). Variational Bayesian Blind Deconvolution Using a Total Variation Prior. *IEEE Transactions on Image Processing*, 18(1):12–26.

[Barrett *et al.* (1994)] Barrett, R., Berry, M., Chan, T. F., Demmel, J., Donato, J., Dongarra, J., Eijkhout, V., Pozo, R., Romine, C., and Van der Vorst, H. (1994). *Templates for the Solution of Linear Systems: Building Blocks for Iterative Methods, 2nd Edition*. SIAM, Philadelphia, PA.

[Beck and Teboulle (2009)] Beck, A. and Teboulle, M. (2009). Fast Gradient-Based Algorithms for Constrained Total Variation Image Denoising and Deblurring Problems. *IEEE Transactions on Image Processing*, 18(11):2419–2434.

[Becker *et al.* (2011)] Becker, S., Bobin, J., and Candès, E. (2011). NESTA: A Fast and Accurate First-Order Method for Sparse Recovery. *SIAM Journal on Imaging Sciences*, 4(1):1–39.

[Bioucas-Dias *et al.* (2006)] Bioucas-Dias, J., Figueiredo, M., and Oliveira, J. (2006). Total Variation-Based Image Deconvolution: a Majorization-Minimization Approach. In *2006 IEEE International Conference on Acoustics, Speech and Signal Processing, 2006. ICASSP 2006 Proceedings*, volume 2, pages II–II.

[Blu and Luisier (2007)] Blu, T. and Luisier, F. (2007). The SURE-LET approach to image denoising. *IEEE transactions on image processing: a publication of the IEEE Signal Processing Society*, 16(11):2778–2786.

[Bonnassie *et al.* (2003)] Bonnassie, A., Peyrin, F., and Attali, D. (2003). A new method for analyzing local shape in three-dimensional images based on medial axis transformation. *IEEE Transactions on Systems, Man, and Cybernetics, Part B: Cybernetics*, 33(4):700–705.

[Bonse *et al.* (1994)] Bonse, U., Busch, F., Günnewig, O., Beckmann, F., Pahl, R., Delling, G., Hahn, M., and Graeff, W. (1994). 3d computed X-ray tomography of human cancellous bone at 8 microns spatial and 10(-4) energy resolution. *Bone and Mineral*, 25(1):25–38.

[Bousson *et al.* (2004)] Bousson, V., Peyrin, F., Bergot, C., Hausard, M., Sautet, A., and Laredo, J.-D. (2004). Cortical Bone in the Human Femoral Neck: Three-Dimensional Appearance and Porosity Using Synchrotron Radiation. *Journal of Bone and Mineral Research*, 19(5):794–801.

[Boutroy *et al.* (2005)] Boutroy, S., Bouxsein, M. L., Munoz, F., and Delmas, P. D. (2005). In Vivo Assessment of Trabecular Bone Microarchitecture by High-Resolution Peripheral Quantitative Computed Tomography. *The Journal of Clinical Endocrinology & Metabolism*, 90(12):6508–6515.

[Bouxsein *et al.* (2010)] Bouxsein, M. L., Boyd, S. K., Christiansen, B. A., Guldberg, R. E., Jepsen, K. J., and Müller, R. (2010). Guidelines for assessment of bone microstructure in rodents using micro–computed tomography. *Journal of Bone and Mineral Research*, 25(7):1468–1486.

[Boyd (2008)] Boyd, S. K. (2008). Site-Specific Variation of Bone Micro-Architecture in the Distal Radius and Tibia. *Journal of Clinical Densitometry*, 11(3):424–430.

[Boyd *et al.* (2011)] Boyd, S., Parikh, N., Chu, E., Peleato, B., and Eckstein, J. (2011). Distributed Optimization and Statistical Learning via the Alternating Direction Method of Multipliers. *Found. Trends Mach. Learn.*, 3(1):1–122.

[Boyd and Vandenberghe (2004)] Boyd, S. and Vandenberghe, L. (2004). *Convex Optimization*. Cambridge University Press, New York, NY, USA.

[Bregman (1967)] Bregman, L. M. (1967). The relaxation method of finding the common point of convex sets and its application to the solution of problems in convex programming. *USSR Computational Mathematics and Mathematical Physics*, 7(3):200–217.

[Burger and Osher (2004)] Burger, M. and Osher, S. (2004). Convergence rates of convex variational regularization. *Inverse Problems*, 20(5):1411.

[Burghardt *et al.* (2007)] Burghardt, A. J., Kazakia, G. J., and Majumdar, S. (2007). A Local Adaptive Threshold Strategy for High Resolution Peripheral Quantitative Computed Tomography of Trabecular Bone. *Annals of Biomedical Engineering*, 35(10):1678–1686.

[Burghardt *et al.* (2010)a] Burghardt, A. J., Kazakia, G. J., Ramachandran, S., Link, T. M., and Majumdar, S. (2010a). Age- and gender-related differences in the geometric properties and biomechanical significance of intracortical porosity in the distal radius and tibia. *Journal of Bone and Mineral Research*, 25(5):983–993.

[Burghardt *et al.* (2010)b] Burghardt, A. J., Kazakia, G. J., Sode, M., de Papp, A. E., Link, T. M., and Majumdar, S. (2010b). A longitudinal HR-pQCT study of alendronate treatment in postmenopausal women with low bone density: Relations among density, cortical and trabecular microarchitecture, biomechanics, and bone turnover. *Journal of Bone and Mineral Research*, 25(12):2558–2571.

[Burghardt *et al.* (2011)] Burghardt, A. J., Link, T. M., and Majumdar, S. (2011). High-resolution Computed Tomography for Clinical Imaging of Bone Microarchitecture. *Clinical Orthopaedics and Related Research®*, 469(8):2179–2193.

[Burghardt *et al.* (2013)] Burghardt, A. J., Pialat, J.-B., Kazakia, G. J., Boutroy, S., Engelke, K., Patsch, J. M., Valentinitsch, A., Liu, D., Szabo, E., Bogado, C. E., Zanchetta, M. B., McKay, H. A., Shane, E., Boyd, S. K., Bouxsein, M. L., Chapurlat, R., Khosla, S., and Majumdar, S. (2013). MULTI-CENTER PRECISION OF CORTICAL AND TRABECULAR BONE QUALITY MEASURES ASSESSED BY HR-PQCT. *Journal of bone and mineral research : the official journal of the American Society for Bone and Mineral Research*, 28(3):524–536.

[Chambolle (2004)] Chambolle, A. (2004). An Algorithm for Total Variation Minimization and Applications. *Journal of Mathematical Imaging and Vision*, 20(1-2):89–97.

[Chambolle and Lions (1997)] Chambolle, A. and Lions, P.-L. (1997). Image recovery via total variation minimization and related problems. *Numerische Mathematik*, 76(2):167–188.

[Chan *et al.* (2000)] Chan, T., Marquina, A., and Mulet, P. (2000). High-Order Total Variation-Based Image Restoration. *SIAM J. Sci. Comput.*, 22(2):503–516.

[Chan *et al.* (2001)] Chan, T. F., Vese, L., and others (2001). Active contours without edges. *Image processing, IEEE transactions on*, 10(2):266–277.

[Chan *et al.* (2006)] Chan, T., Esedoglu, S., and Nikolova, M. (2006). Algorithms for Finding Global Minimizers of Image Segmentation and Denoising Models. *SIAM Journal on Applied Mathematics*, 66(5):1632–1648.

[Chan *et al.* (2007)] Chan, T. F., Esedoglu, S., and Park, F. E. (2007). Image Decomposition Combining Staircase Reduction and Texture Extraction. *J. Vis. Comun. Image Represent.*, 18(6):464–486.

[Chan and Shen (2002)] Chan, T. F. and Shen, J. (2002). Mathematical Models for Local Nontexture Inpaintings. *SIAM J. Appl. Math*, 62:1019–1043.

[Chan and Shen (2005)] Chan, T. F. and Shen, J. J. (2005). *Image processing and analysis: variational, PDE, wavelet, and stochastic methods*. Siam.

[Chan and Wong (1998)] Chan, T. and Wong, C.-K. (1998). Total variation blind deconvolution. *IEEE Transactions on Image Processing*, 7(3):370–375.

[Chan and Wong (2000)] Chan, T. F. and Wong, C. K. (2000). Convergence of the alternating minimization algorithm for blind deconvolution. *Linear Algebra and its Applications*, 316(1–3):259–285.

[Chapurlat and Delmas (2009)] Chapurlat, R. D. and Delmas, P. D. (2009). Bone microdamage: a clinical perspective. *Osteoporosis International*, 20(8):1299–1308.

[Chaudhuri (2002)] Chaudhuri, S., editor (2002). *Super-Resolution Imaging*, volume 632 of *The International Series in Engineering and Computer Science*. Kluwer Academic Publishers, Boston.

[Chen and Ning (2004)] Chen, Z. and Ning, R. (2004). Three-dimensional point spread function measurement of cone-beam computed tomography system by iterative edge-blurring algorithm. *Physics in Medicine and Biology*, 49(10):1865.

[Cheung *et al.* (2013)] Cheung, A. M., Adachi, J. D., Hanley, D. A., Kendler, D. L., Davison, K. S., Josse, R., Brown, J. P., Ste-Marie, L.-G., Kremer, R., Erlandson, M. C., Dian, L., Burghardt, A. J., and Boyd, S. K. (2013). High-Resolution Peripheral Quantitative Computed Tomography for the Assessment of Bone Strength and Structure: A Review by the Canadian Bone Strength Working Group. *Current Osteoporosis Reports*, 11(2):136–146.

[Combettes and Pesquet (2004)] Combettes, P. and Pesquet, J. (2004). Image restoration subject to a total variation constraint. *IEEE Transactions on Image Processing*, 13(9):1213–1222.

[Combettes and Pesquet (2007)] Combettes, P. and Pesquet, J. (2007). A Douglas-Rachford Splitting Approach to Nonsmooth Convex Variational Signal Recovery. *IEEE Journal of Selected Topics in Signal Processing*, 1(4):564–574.

[Combettes and Pesquet (2008)] Combettes, P. L. and Pesquet, J.-C. (2008). A Proximal Decomposition Method for Solving Convex Variational Inverse Problems. *Inverse Problems*, 24(6):065014. arXiv: 0807.2617.

[Cremers *et al.* (2006)] Cremers, D., Rousson, M., and Deriche, R. (2006). A Review of Statistical Approaches to Level Set Segmentation: Integrating Color, Texture, Motion and Shape. *International Journal of Computer Vision*, 72(2):195–215.

[Davis *et al.* (2007)] Davis, K. A., Burghardt, A. J., Link, T. M., and Majumdar, S. (2007). The Effects of Geometric and Threshold Definitions on Cortical Bone Metrics Assessed by In Vivo High-Resolution Peripheral Quantitative Computed Tomography. *Calcified Tissue International*, 81(5):364–371.

[Deledalle *et al.* (2014)] Deledalle, C., Vaiter, S., Fadili, J., and Peyré, G. (2014). Stein Unbiased GrAdient estimator of the Risk (SUGAR) for Multiple Parameter Selection. *SIAM Journal on Imaging Sciences*, 7(4):2448–2487.

[Dice (1945)] Dice, L. R. (1945). Measures of the Amount of Ecologic Association Between Species. *Ecology*, 26(3):297–302.

[Ding *et al.* (2002)] Ding, M., Odgaard, A., Linde, F., and Hvid, I. (2002). Age-related variations in the microstructure of human tibial cancellous bone. *Journal of Orthopaedic Research*, 20(3):615–621.

[Eldar (2009)] Eldar, Y. C. (2009). Generalized SURE for Exponential Families: Applications to Regularization. *Trans. Sig. Proc.*, 57(2):471–481.

[Engelke *et al.* (1989)] Engelke, K., Lohmann, M., Dix, W. R., and Graeff, W. (1989). A system for dual energy microtomography of bones. *Nuclear Instruments and Methods in Physics Research Section A: Accelerators, Spectrometers, Detectors and Associated Equipment*, 274(1–2):380–389.

[Engl *et al.* (1996)] Engl, H. W., Hanke, M., and Neubauer, A. (1996). *Regularization of Inverse Problems*. Springer Science & Business Media.

[Esser (2009)] Esser, E. (2009). Applications of Lagrangian-Based alternating direction methods and connections to split Bregman. CAM report.

[Fadili *et al.* (2013)] Fadili, M. J., Peyré, G., Vaiter, S., Deledalle, C., and Salmon, J. (2013). Stable Recovery with Analysis Decomposable Priors. pages 113–116. arXiv: 1304.4407.

[Farsiu *et al.* (2004)] Farsiu, S., Robinson, M., Elad, M., and Milanfar, P. (2004). Fast and robust multiframe super resolution. *IEEE Transactions on Image Processing*, 13(10):1327–1344.

[Feldkamp *et al.* (1984)] Feldkamp, L. A., Davis, L. C., and Kress, J. W. (1984). Practical cone-beam algorithm. *J Opt Soc Am*, pages 612–619.

[Feldkamp *et al.* (1989)] Feldkamp, L. A., Goldstein, S. A., Parfitt, M. A., Jesion, G., and Kleerekoper, M. (1989). The direct examination of three-dimensional bone architecture in vitro by computed tomography. *Journal of Bone and Mineral Research*, 4(1):3–11.

[Florencio-Silva *et al.* (2015)] Florencio-Silva, R., Sasso, G. R. d. S., Sasso-Cerri, E., Simões, M. J., and Cerri, P. S. (2015). Biology of Bone Tissue: Structure, Function, and Factors That Influence Bone Cells. *BioMed Research International*, 2015.

[Frick *et al.* (2011)] Frick, K., Lorenz, D., and Resmerita, E. (2011). Morozov's Principle for the Augmented Lagrangian Method Applied to Linear Inverse Problems. *Multiscale Modeling & Simulation*, 9(4):1528–1548.

[Galatsanos *et al.* (2000)] Galatsanos, N., Mesarovic, V., Molina, R., and Katsaggelos, A. (2000). Hierarchical Bayesian image restoration from partially known blurs. *IEEE Transactions on Image Processing*, 9(10):1784–1797.

[Genant *et al.* (2006)] Genant, H. K., Delmas, P. D., Chen, P., Jiang, Y., Eriksen, E. F., Dalsky, G. P., Marcus, R., and Martin, J. S. (2006). Severity of vertebral fracture reflects deterioration of bone microarchitecture. *Osteoporosis International*, 18(1):69–76.

[Goldstein *et al.* (2010)] Goldstein, T., Bresson, X., and Osher, S. (2010). Geometric Applications of the Split Bregman Method: Segmentation and Surface Reconstruction. *Journal of Scientific Computing*, 45(1-3):272–293.

[Golub *et al.* (1979)] Golub, G. H., Heath, M., and Wahba, G. (1979). Generalized Cross-Validation as a Method for Choosing a Good Ridge Parameter. *Technometrics*, 21(2):215–223.

[Gonzalez and Woods (2002)] Gonzalez, R. C. and Woods, R. E. (2002). Digital image processing. Second Edition. *Upper Saddle River, NJ, US: Prentice Hall*.

[Grasmair (2011)] Grasmair, M. (2011). Linear convergence rates for Tikhonov regularization with positively homogeneous functionals. *Inverse Problems*, 27(7):075014.

[Hadamard (1902)] Hadamard, J. (1902). Sur Les Problèmes Aux Dérivées Partielles et Leur Signification Physique. *Princeton University Bulletin*, 13:49–52.

[Hansen and O'Leary (1993)] Hansen, P. and O'Leary, D. (1993). The Use of the L-Curve in the Regularization of Discrete Ill-Posed Problems. *SIAM Journal on Scientific Computing*, 14(6):1487–1503.

[Hestenes and Stiefel (1952)] Hestenes, M. and Stiefel, E. (1952). Methods of Conjugate Gradients for Solving Linear Systems. *Journal of Research of the National Bureau of Standards*, 49(6):409–436.

[Hildebrand *et al.* (1999)] Hildebrand, T., Laib, A., Müller, R., Dequeker, J., and Rüegsegger, P. (1999). Direct Three-Dimensional Morphometric Analysis of Human Cancellous Bone: Microstructural Data from Spine, Femur, Iliac Crest, and Calcaneus. *Journal of Bone and Mineral Research*, 14(7):1167–1174.

[Hildebrand and Rüegsegger (1997)] Hildebrand, T. and Rüegsegger, P. (1997). Quantification of Bone Microarchitecture with the Structure Model Index. *Computer Methods in Biomechanics and Biomedical Engineering*, 1(1):15–23.

[Hintermüller and Wu (2015)] Hintermüller, M. and Wu, T. (2015). Bilevel optimization for calibrating point spread functions in blind deconvolution. *Inverse Problems and Imaging*, 9(4):1139–1169.

[Hu and Jacob (2012)] Hu, Y. and Jacob, M. (2012). Higher Degree Total Variation (HDTV) Regularization for Image Recovery. *IEEE Transactions on Image Processing*, 21(5):2559–2571.

[Hulme *et al.* (2007)] Hulme, P. A., Boyd, S. K., and Ferguson, S. J. (2007). Regional variation in vertebral bone morphology and its contribution to vertebral fracture strength. *Bone*, 41(6):946–957.

[Hutchinson (1990)] Hutchinson, M. F. (1990). A stochastic estimator of the trace of the influence matrix for Laplacian smoothing splines. Commun Stat Simul Comput 18:1059-1076. *Communication in Statistics- Simulation and Computation*, 19(2):432–450.

[Ito *et al.* (1998)] Ito, M., Nakamura, T., Matsumoto, T., Tsurusaki, K., and Hayashi, K. (1998). Analysis of trabecular microarchitecture of human iliac bone using microcomputed tomography in patients with hip arthrosis with or without vertebral fracture. *Bone*, 23(2):163–169.

[Jiang *et al.* (2005)] Jiang, Y., Zhao, J., Liao, E.-Y., Dai, R.-C., Wu, X.-P., and Genant, H. K. (2005). Application of micro-ct assessment of 3-d bone microstructure in preclinical and clinical studies. *Journal of Bone and Mineral Metabolism*, 23(1):122–131.

[Jiang *et al.* (2014)] Jiang, M., Maass, P., and Page, T. (2014). Regularizing properties of the Mumford–Shah functional for imaging applications. *Inverse Problems*, 30(3):035007.

[Justen and Ramlau (2006)] Justen, L. and Ramlau, R. (2006). A non-iterative regularization approach to blind deconvolution. *Inverse Problems*, 22(3):771.

[Kanis (2002)] Kanis, J. A. (2002). Diagnosis of osteoporosis and assessment of fracture risk. *The Lancet*, 359(9321):1929–1936.

[Khosla *et al.* (2006)] Khosla, S., Riggs, B. L., Atkinson, E. J., Oberg, A. L., McDaniel, L. J., Holets, M., Peterson, J. M., and Melton, L. J. (2006). Effects of Sex and Age on Bone Microstructure at the Ultradistal Radius: A Population-Based Noninvasive In Vivo Assessment. *Journal of bone and mineral research : the official journal of the American Society for Bone and Mineral Research*, 21(1):124–131.

[Kiwiel (1997)] Kiwiel, K. (1997). Proximal Minimization Methods with Generalized Bregman Functions. *SIAM Journal on Control and Optimization*, 35(4):1142–1168.

[Klein *et al.* (2010)] Klein, S., Staring, M., Murphy, K., Viergever, M., and Pluim, J. (2010). elastix: A Toolbox for Intensity-Based Medical Image Registration. *IEEE Transactions on Medical Imaging*, 29(1):196–205.

[Klein and Staring (2015)] Klein, S. and Staring, M. (2015). *Elastix: the manual*. v4.8 edition.

[Krause *et al.* (2014)] Krause, M., Museyko, O., Breer, S., Wulff, B., Duckstein, C., Vettorazzi, E., Glueer, C., Püschel, K., Engelke, K., and Amling, M. (2014). Accuracy of trabecular structure by HR-pQCT compared to gold standard μCT in the radius and tibia of patients with osteoporosis and long-term bisphosphonate therapy. *Osteoporosis International*, 25(5):1595–1606.

[Krug *et al.* (2010)] Krug, R., Burghardt, A. J., Majumdar, S., and Link, T. M. (2010). High-resolution Imaging Techniques for the Assessment of Osteoporosis. *Radiologic clinics of North America*, 48(3):601–621.

[Kulak and Dempster (2010)] Kulak, C. A. M. and Dempster, D. W. (2010). Bone histomorphometry: a concise review for endocrinologists and clinicians. *Arquivos Brasileiros De Endocrinologia E Metabologia*, 54(2):87–98.

[Kunisch (1993)] Kunisch, K. (1993). On a class of damped Morozov principles. *Computing*, 50(3):185–198.

[Kunisch and Zou (1998)] Kunisch, K. and Zou, J. (1998). Iterative choices of regularization parameters in linear. *Inverse Problems*, 14(5):1247.

[Křížek and Korotov (2004)] Křížek, M. and Korotov, S. (2004). Geometric Interpretations of Conjugate Gradient and Related Methods. In Křížek, P. M., Neittaanmäki, P. P., Korotov, D. S., and Glowinski, P. R., editors, *Conjugate Gradient Algorithms and Finite Element Methods*, Scientific Computation, pages 25–43. Springer Berlin Heidelberg. DOI: 10.1007/978-3-642-18560-1_3.

[Laib and Rüegsegger (1999)] Laib, A. and Rüegsegger, P. (1999). Comparison of structure extraction methods for in vivo trabecular bone measurements. *Computerized Medical Imaging and Graphics*, 23(2):69–74.

[Lefkimmiatis *et al.* (2012)a] Lefkimmiatis, S., Bourquard, A., and Unser, M. (2012a). Hessian-Based Norm Regularization for Image Restoration With Biomedical Applications. *IEEE Transactions on Image Processing*, 21(3):983–995.

[Lefkimmiatis *et al.* (2012)b] Lefkimmiatis, S., Bourquard, A., and Unser, M. (2012b). Hessian-based regularization for 3-D microscopy image restoration. In *2012 9th IEEE International Symposium on Biomedical Imaging (ISBI)*, pages 1731–1734.

[Lehmann *et al.* (1999)] Lehmann, T., Gonner, C., and Spitzer, K. (1999). Survey: interpolation methods in medical image processing. *IEEE Transactions on Medical Imaging*, 18(11):1049–1075.

[Liao *et al.* (2009)] Liao, H., Li, F., and Ng, M. K. (2009). Selection of regularization parameter in total variation image restoration. *Journal of the Optical Society of America. A, Optics, Image Science, and Vision*, 26(11):2311–2320.

[Liao and Ng (2011)] Liao, H. and Ng, M. (2011). Blind Deconvolution Using Generalized Cross-Validation Approach to Regularization Parameter Estimation. *IEEE Transactions on Image Processing*, 20(3):670–680.

[Lin *et al.* (2010)] Lin, Y., Wohlberg, B., and Guo, H. (2010). UPRE method for total variation parameter selection. *Signal Processing*, 90(8):2546–2551.

[Liu *et al.* (2008)] Liu, X. S., Sajda, P., Saha, P. K., Wehrli, F. W., Bevill, G., Keaveny, T. M., and Guo, X. E. (2008). Complete Volumetric Decomposition of Individual Trabecular Plates and Rods and Its Morphological Correlations With Anisotropic Elastic Moduli in Human Trabecular Bone. *Journal of Bone and Mineral Research*, 23(2):223–235.

[Lysaker *et al.* (2003)] Lysaker, M., Lundervold, A., and Tai, X.-C. (2003). Noise removal using fourth-order partial differential equation with applications to medical magnetic resonance images in space and time. *IEEE Transactions on Image Processing*, 12(12):1579–1590.

[Lysaker and Tai (2006)] Lysaker, M. and Tai, X.-C. (2006). Iterative Image Restoration Combining Total Variation Minimization and a Second-Order Functional. *International Journal of Computer Vision*, 66(1):5–18.

[Macdonald *et al.* (2010)] Macdonald, H. M., Nishiyama, K. K., Hanley, D. A., and Boyd, S. K. (2010). Changes in trabecular and cortical bone microarchitecture at peripheral sites associated with 18 months of teriparatide therapy in postmenopausal women with osteoporosis. *Osteoporosis International*, 22(1):357–362.

[Macdonald *et al.* (2011)] Macdonald, H. M., Nishiyama, K. K., Kang, J., Hanley, D. A., and Boyd, S. K. (2011). Age-related patterns of trabecular and cortical bone loss differ between sexes and skeletal sites: A population-based HR-pQCT study. *Journal of Bone and Mineral Research*, 26(1):50–62.

[Melton *et al.* (1989)] Melton, L. J., Kan, S. H., Frye, M. A., Wahner, H. W., O'Fallon, W. M., and Riggs, B. L. (1989). Epidemiology of Vertebral Fractures in Women. *American Journal of Epidemiology*, 129(5):1000–1011.

[Meunier and Boivin (1997)] Meunier, P. J. and Boivin, G. (1997). Bone mineral density reflects bone mass but also the degree of mineralization of bone: Therapeutic implications. *Bone*, 21(5):373–377.

[Mohamad-Djafari (2013)] Mohamad-Djafari, A. (2013). *Inverse Problems in Vision and 3D Tomography*. John Wiley & Sons.

[Mohammad-Djafari (2008)] Mohammad-Djafari, A. (2008). Super-Resolution: A Short Review, A New Method Based on Hidden Markov Modeling of HR Image and Future Challenges. *The Computer Journal*, 52(1):126–141.

[Molina (1994)] Molina, R. (1994). On the hierarchical Bayesian approach to image restoration: applications to astronomical images. *IEEE Transactions on Pattern Analysis and Machine Intelligence*, 16(11):1122–1128.

[Molina *et al.* (2006)] Molina, R., Mateos, J., and Katsaggelos, A. K. (2006). Blind deconvolution using a variational approach to parameter, image, and blur estimation. *IEEE Trans. on Image Processing*, 15:3715–3727.

[Morozov (1984)] Morozov, V. A. (1984). *Methods for Solving Incorrectly Posed Problems*. Springer New York, New York, NY.

[Mueller *et al.* (2009)] Mueller, T. L., van Lenthe, G. H., Stauber, M., Gratzke, C., Eckstein, F., and Müller, R. (2009). Regional, age and gender differences in architectural measures of bone quality and their correlation to bone mechanical competence in the human radius of an elderly population. *Bone*, 45(5):882–891.

[Mumford and Shah (1989)] Mumford, D. and Shah, J. (1989). Optimal approximations by piecewise smooth functions and associated variational problems. *Communications on Pure and Applied Mathematics*, 42(5):577–685.

[Ng *et al.* (2010)] Ng, M., Weiss, P., and Yuan, X. (2010). Solving Constrained Total-variation Image Restoration and Reconstruction Problems via Alternating Direction Methods. *SIAM Journal on Scientific Computing*, 32(5):2710–2736.

[Nuzzo *et al.* (2002)a] Nuzzo, S., Lafage-Proust, M. H., Martin-Badosa, E., Boivin, G., Thomas, T., Alexandre, C., and Peyrin, F. (2002a). Synchrotron Radiation Microtomography Allows the Analysis of Three-Dimensional Microarchitecture and Degree of Mineralization of Human Iliac Crest Biopsy Specimens: Effects of Etidronate Treatment. *Journal of Bone and Mineral Research*, 17(8):1372–1382.

[Nuzzo *et al.* (2002)b] Nuzzo, S., Peyrin, F., Cloetens, P., Baruchel, J., and Boivin, G. (2002b). Quantification of the degree of mineralization of bone in three dimensions using synchrotron radiation microtomography. *Medical Physics*, 29(11):2672–2681.

[Odgaard (1997)] Odgaard, A. (1997). Three-dimensional methods for quantification of cancellous bone architecture. *Bone*, 20(4):315–328.

[Odgaard and Gundersen (1993)] Odgaard, A. and Gundersen, H. J. G. (1993). Quantification of connectivity in cancellous bone, with special emphasis on 3-D reconstructions. *Bone*, 14(2):173–182.

[Ohser *et al.* (2011)] Ohser, J., Nagel, W., and Schladitz, K. (2011). MILES FORMULAE FOR BOOLEAN MODELS OBSERVED ON LATTICES. *Image Analysis & Stereology*, 28(2):77–92.

[Otsu (1979)] Otsu, N. (1979). A Threshold Selection Method from Gray-Level Histograms. *IEEE Transactions on Systems, Man and Cybernetics*, 9(1):62–66.

[Parfitt *et al.* (1987)] Parfitt, A. M., Drezner, M. K., Glorieux, F. H., Kanis, J. A., Malluche, H., Meunier, P. J., Ott, S. M., and Recker, R. R. (1987). Bone histomorphometry: Standardization of nomenclature, symbols, and units: Report of the asbmr histomorphometry nomenclature committee. *Journal of Bone and Mineral Research*, 2(6):595–610.

[Park *et al.* (2003)] Park, S. C., Park, M. K., and Kang, M. G. (2003). Super-resolution image reconstruction: a technical overview. *IEEE Signal Processing Magazine*, 20(3):21–36.

[Patsch and Bauer (2013)] Patsch, J. M. and Bauer, J. S. (2013). High-Resolution Imaging. In Guglielmi, G., editor, *Osteoporosis and Bone Densitometry Measurements*, Medical Radiology, pages 149–159. Springer Berlin Heidelberg.

[Patti *et al.* (1994)] Patti, A., Sezan, M., and Tekalp, A. (1994). High-resolution image reconstruction from a low-resolution image sequence in the presence of time-varying motion blur. In *Image Processing, 1994. Proceedings. ICIP-94., IEEE International Conference*, volume 1, pages 343–347 vol.1.

[Paul *et al.* (2013)] Paul, G., Cardinale, J., and Sbalzarini, I. F. (2013). Coupling Image Restoration and Segmentation: A Generalized Linear Model/Bregman Perspective. *International Journal of Computer Vision*, 104(1):69–93.

[Peter and Peyrin (2011)] Peter, Z.-A. and Peyrin, F. (2011). *Synchrotron radiation micro-CT imaging of bone tissue*. N homma intech edition.

[Peyrin *et al.* (2010)] Peyrin, F., Attali, D., Chappard, C., and Benhamou, C. L. (2010). Local plate/rod descriptors of 3d trabecular bone micro-CT images from medial axis topologic analysis. *Medical Physics*, 37(8):4364–4376.

[Peyrin and Engelke (2012)] Peyrin, F. and Engelke, K. (2012). CT Imaging: Basics and New Trends. In *Handbook of Particle Detection and Imaging*, page 883.

[Peyré *et al.* (2011)] Peyré, G., Bougleux, S., and Cohen, L. D. (2011). Non-local Regularization of Inverse Problems. *Inverse Problems and Imaging*, 5(2):511–530.

[Pialat *et al.* (2012)] Pialat, J. B., Vilayphiou, N., Boutroy, S., Gouttenoire, P. J., Sornay-Rendu, E., Chapurlat, R., and Peyrin, F. (2012). Local topological analysis at the distal radius by HR-pQCT: Application to in vivo bone microarchitecture and fracture assessment in the OFELY study. *Bone*, 51(3):362–368.

[R. Y. Tsai (1984)] R. Y. Tsai, T. S. H. (1984). Multiframe image restoration and registration. *Adv. Comput. Vis. Image Process*, 1.

[Ramani *et al.* (2008)] Ramani, S., Blu, T., and Unser, M. (2008). Monte-Carlo sure: a black-box optimization of regularization parameters for general denoising algorithms. *IEEE transactions on image processing: a publication of the IEEE Signal Processing Society*, 17(9):1540–1554.

[Ramani *et al.* (2012)] Ramani, S., Liu, Z., Rosen, J., Nielsen, J., and Fessler, J. (2012). Regularization Parameter Selection for Nonlinear Iterative Image Restoration and MRI Reconstruction Using GCV and SURE-Based Methods. *IEEE Transactions on Image Processing*, 21(8):3659–3672.

[Ramlau and Ring (2007)] Ramlau, R. and Ring, W. (2007). A Mumford-Shah level-set approach for the inversion and segmentation of X-ray tomography data. *J. of Computational Physics*.

[Ramlau and Ring (2010)] Ramlau, R. and Ring, W. (2010). Regularization of ill-posed Mumford–Shah models with perimeter penalization. *Inverse Problems*, 26(11):115001.

[Ren *et al.* (2013)] Ren, Z., He, C., and Zhang, Q. (2013). Fractional order total variation regularization for image super-resolution. *Signal Processing*, 93(9):2408–2421.

[Resmerita (2005)] Resmerita, E. (2005). Regularization of ill-posed problems in Banach spaces: convergence rates. *Inverse Problems*, 21(4):1303.

[Riggs and Melton III (1983)] Riggs, B. L. and Melton III, L. J. (1983). Evidence for two distinct syndromes of involutional osteoporosis. *The American Journal of Medicine*, 75(6):899–901.

[Rizzoli *et al.* (2010)] Rizzoli, R., Laroche, M., Krieg, M.-A., Frieling, I., Thomas, T., Delmas, P., and Felsenberg, D. (2010). Strontium ranelate and alendronate have differing effects on distal tibia bone microstructure in women with osteoporosis. *Rheumatology International*, 30(10):1341–1348.

[Rudin *et al.* (1992)] Rudin, L. I., Osher, S., and Fatemi, E. (1992). Nonlinear total variation based noise removal algorithms. *Physica D: Nonlinear Phenomena*, 60(1–4):259–268.

[Ruiz *et al.* (2015)] Ruiz, P., Zhou, X., Mateos, J., Molina, R., and Katsaggelos, A. K. (2015). Variational Bayesian Blind Image Deconvolution: A review. *Digital Signal Processing*.

[Rüegsegger *et al.* (1996)] Rüegsegger, P., Koller, B., and Müller, R. (1996). A microtomographic system for the nondestructive evaluation of bone architecture. *Calcified Tissue International*, 58(1):24–29.

[Salomé *et al.* (1999)] Salomé, M., Peyrin, F., Cloetens, P., Odet, C., Laval-Jeantet, A.-M., Baruchel, J., and Spanne, P. (1999). A synchrotron radiation microtomography system for the analysis of trabecular bone samples. *Medical Physics*, 26(10):2194–2204.

[Schatzberg and Devaney (1992)] Schatzberg, A. and Devaney, A. J. (1992). Super-resolution in diffraction tomography. *Inverse Problems*, 8(1):149–164.

[Scherzer *et al.* (2008)] Scherzer, O., Grasmair, M., Grossauer, H., Haltmeier, M., and Lenzen, F. (2008). *Variational Methods in Imaging*. Springer New York, 1 edition edition.

[Schultz and Stevenson (1996)] Schultz, R. and Stevenson, R. (1996). Extraction of high-resolution frames from video sequences. *IEEE Transactions on Image Processing*, 5(6):996–1011.

[Seeman *et al.* (2010)] Seeman, E., Delmas, P. D., Hanley, D. A., Sellmeyer, D., Cheung, A. M., Shane, E., Kearns, A., Thomas, T., Boyd, S. K., Boutroy, S., Bogado, C., Majumdar, S., Fan, M., Libanati, C., and Zanchetta, J. (2010). Microarchitectural deterioration of cortical and trabecular bone: Differing effects of denosumab and alendronate. *Journal of Bone and Mineral Research*, 25(8):1886–1894.

[Seeman and Delmas (2006)] Seeman, E. and Delmas, P. D. (2006). Bone quality–the material and structural basis of bone strength and fragility. *The New England Journal of Medicine*, 354(21):2250–2261.

[Shekarforoush *et al.* (1996)] Shekarforoush, H., Berthod, M., and Zerubia, J. (1996). Subpixel image registration by estimating the polyphase decomposition of cross power spectrum. In *Proceedings CVPR '96, 1996 IEEE Computer Society Conference on Computer Vision and Pattern Recognition, 1996*, pages 532–537.

[Shewchuk (1994)] Shewchuk, J. R. (1994). An Introduction to the Conjugate Gradient Method Without the Agonizing Pain. Technical report, Carnegie Mellon University, Pittsburgh, PA, USA.

[Stark and Oskoui (1989)] Stark, H. and Oskoui, P. (1989). High-resolution image recovery from image-plane arrays, using convex projections. *Journal of the Optical Society of America. A, Optics and Image Science*, 6(11):1715–1726.

[Stauber and Müller (2006)] Stauber, M. and Müller, R. (2006). Volumetric spatial decomposition of trabecular bone into rods and plates—A new method for local bone morphometry. *Bone*, 38(4):475–484.

[Steidl (2005)] Steidl, G. (2005). A Note on the Dual Treatment of Higher-Order Regularization Functionals. *Computing*, 76(1-2):135–148.

[Storath *et al.* (2014)] Storath, M., Weinmann, A., and Demaret, L. (2014). Jump-Sparse and Sparse Recovery Using Potts Functionals. *IEEE Transactions on Signal Processing*, 62(14):3654–3666.

[Tekalp *et al.* (1992)] Tekalp, A., Ozkan, M., and Sezan, M. (1992). High-resolution image reconstruction from lower-resolution image sequences and space-varying image restoration. In *, 1992 IEEE International Conference on Acoustics, Speech, and Signal Processing, 1992. ICASSP-92*, volume 3, pages 169–172 vol.3.

[Tikhonov and Arsenin (1977)] Tikhonov, A. N. and Arsenin, V. I. (1977). *Solutions of ill-posed problems*. Winston.

[Tjong *et al.* (2012)] Tjong, W., Kazakia, G. J., Burghardt, A. J., and Majumdar, S. (2012). The effect of voxel size on high-resolution peripheral computed tomography measurements of trabecular and cortical bone microstructure. *Medical physics*, 39(4):1893–1903.

[Tom and Katsaggelos (1994)] Tom, B. C. and Katsaggelos, A. K. (1994). Reconstruction of a High Resolution Image from Multiple Degraded Mis-Registered Low Resolution Images. In *in Proceedings of the IEEE International Conference on Image Processing*, pages 553–557.

[Vaiter *et al.* (2013)] Vaiter, S., Deledalle, C.-A., Peyré, G., Dossal, C., and Fadili, J. (2013). Local behavior of sparse analysis regularization: Applications to risk estimation. *Applied and Computational Harmonic Analysis*, 35(3):433–451.

[Vogel (2002)] Vogel, C. (2002). *Computational Methods for Inverse Problems*. Frontiers in Applied Mathematics. Society for Industrial and Applied Mathematics.

[Vonesch *et al.* (2008)] Vonesch, C., Ramani, S., and Unser, M. (2008). Recursive risk estimation for non-linear image deconvolution with a wavelet-domain sparsity constraint. In *15th IEEE International Conference on Image Processing, 2008. ICIP 2008*, pages 665–668.

[Wang *et al.* (2008)] Wang, Y., Yang, J., Yin, W., and Zhang, Y. (2008). A New Alternating Minimization Algorithm for Total Variation Image Reconstruction. *SIAM Journal on Imaging Sciences*, 1(3):248–272.

[Weinmann *et al.* (2015)] Weinmann, A., Storath, M., and Demaret, L. (2015). The L1-Potts functional for robust jump-sparse reconstruction. *SIAM Journal on Numerical Analysis*, 53(1):644–673. arXiv: 1207.4642.

[Wen and Chan (2012)] Wen, Y.-W. and Chan, R. (2012). Parameter selection for total-variation-based image restoration using discrepancy principle. *IEEE Transactions on Image Processing*, 21(4):1770–1781.

[Wrixon (2008)] Wrixon, A. D. (2008). New ICRP recommendations. *Journal of Radiological Protection*, 28(2):161.

[Yang *et al.* (2009)] Yang, J., Yin, W., Zhang, Y., and Wang, Y. (2009). A Fast Algorithm for Edge-Preserving Variational Multichannel Image Restoration. *SIAM Journal on Imaging Sciences*, 2(2):569–592.

[You and Kaveh (1996)] You, Y.-L. and Kaveh, M. (1996). A regularization approach to joint blur identification and image restoration. *IEEE Transactions on Image Processing*, 5(3):416–428.

[You and Kaveh (2000)] You, Y.-L. and Kaveh, M. (2000). Fourth-order partial differential equations for noise removal. *IEEE Transactions on Image Processing*, 9(10):1723–1730.

[Yuan *et al.* (2009)] Yuan, J., Schnörr, C., and Steidl, G. (2009). Total-Variation Based Piecewise Affine Regularization. In Tai, X.-C., Mørken, K., Lysaker, M., and Lie, K.-A., editors, *Scale Space and Variational Methods in Computer Vision*, number 5567 in Lecture Notes in Computer Science, pages 552–564. Springer Berlin Heidelberg.

[Zou *et al.* (2004)] Zou, K. H., Warfield, S. K., Bharatha, A., Tempany, C. M., Kaus, M. R., Haker, S. J., Wells, W. M., Jolesz, F. A., and Kikinis, R. (2004). Statistical Validation of Image Segmentation Quality Based on a Spatial Overlap Index. *Academic radiology*, 11(2):178–189.

[van den Berg and Friedlander (2008)] van den Berg, E. and Friedlander, M. (2008). Probing the Pareto Frontier for Basis Pursuit Solutions. *SIAM Journal on Scientific Computing*, 31(2):890–912.

[Office of the Surgeon General (US) (2004)] Office of the Surgeon General (US) (2004). *Bone Health and Osteoporosis: A Report of the Surgeon General*. Reports of the Surgeon General. Office of the Surgeon General (US), Rockville (MD).